Louisiana Tech University
Louisiana Tech Digital Commons

Doctoral Dissertations | Graduate School

Spring 2016

Electromagnetic properties of metal-dielectric media and their applications

Shravan Rakesh Animilli
Louisiana Tech University

Follow this and additional works at: https://digitalcommons.latech.edu/dissertations

Part of the Other Physics Commons

Recommended Citation
Animilli, Shravan Rakesh, "" (2016). *Dissertation*. 139.
https://digitalcommons.latech.edu/dissertations/139

This Dissertation is brought to you for free and open access by the Graduate School at Louisiana Tech Digital Commons. It has been accepted for inclusion in Doctoral Dissertations by an authorized administrator of Louisiana Tech Digital Commons. For more information, please contact digitalcommons@latech.edu.

ELECTROMAGNETIC PROPERTIES OF METAL-DIELECTRIC MEDIA AND THEIR APPLICATIONS

by

Shravan Rakesh Animilli, B. Tech, M. S.

A Dissertation Presented in Partial Fulfillment
of the Requirements of the Degree
Doctor of Philosophy

COLLEGE OF ENGINEERING AND SCIENCE
LOUISIANA TECH UNIVERSITY

May 2016

ProQuest Number: 10300682

All rights reserved

INFORMATION TO ALL USERS
The quality of this reproduction is dependent upon the quality of the copy submitted.

In the unlikely event that the author did not send a complete manuscript
and there are missing pages, these will be noted. Also, if material had to be removed,
a note will indicate the deletion.

ProQuest 10300682

Published by ProQuest LLC(2017). Copyright of the Dissertation is held by the Author.

All rights reserved.
This work is protected against unauthorized copying under Title 17, United States Code.
Microform Edition © ProQuest LLC.

ProQuest LLC
789 East Eisenhower Parkway
P.O. Box 1346
Ann Arbor, MI 48106-1346

LOUISIANA TECH UNIVERSITY

THE GRADUATE SCHOOL

APRIL 11, 2016
Date

We hereby recommend that the dissertation prepared under our supervision by

Shravan Rakesh Animilli, B. Tech, M. S.

entitled **Electromagnetic Properties of Metal-Dielectric Media and Their Applications**

be accepted in partial fulfillment of the requirements for the Degree of

Doctor of Philosophy in Engineering

Supervisor of Dissertation Research

Head of Department

Physics

Department

Recommendation concurred in:

Advisory Committee

Approved:

Director of Graduate Studies

Dean of the College

Approved:

Dean of the Graduate School

GS Form 13
(8/10)

ABSTRACT

The main objective of this dissertation is to investigate nano-structured random composite materials, which exhibit anomalous phenomena, such as the extraordinary enhancements of linear and non-linear optical processes due to excitation of collective electronic states, surface plasmons (SP). The main goal is to develop a time and memory efficient novel numerical method to study the properties of these random media in three dimensions (3D) by utilization of multi core processing and packages such as MPI for parallel execution. The developed numerical studies are then utilized to provide a comprehensive characterization and optimization of a surface plasmon enhanced solar cell (SPESC) and to serve as a test bed for enhanced bio and chemical sensing.

In this context, this thesis work develops an efficient and exact numerical algorithm here referred to as Block Elimination Method (BE) which provides the unique capability of modeling extremely large scale composite materials (with up to 1 million strongly interacting metal or dielectric particles). This capability is crucial in order to study the electromagnetic response of large scale inhomogeneous (fractal) films and bulk composites at critical concentrations (percolation). The developed numerical method is used to accurately estimate parameters that describe the composite materials, including the effective conductivity and correlation length scaling exponents, as well as density of states and localization length exponents at the band center. This works reveals, for a first time, a unique de-localization mechanism that plays an important role in the excitation of charge–

density waves, i.e. surface plasmons (SP), in metal-dielectric composites. It also shows that in 3D metal-dielectric percolation systems the local fields distribution function for frequencies close to the single particle plasmon resonance is log-normal which is a signature of a metal-dielectric phase transition manifested in the optical response of the composites.

Based on the obtained numerical data a scaling theory for the higher order electric field moments is developed. A distinct evidence of singularities in the surface plasmon density of states and localization length is obtained, correlating with results previously obtained for two dimensional systems. This leads to the main finding of this work; i.e., the delocalization of surface plasmon states in percolating metal-dielectric composite materials is universally present regardless of the dimensionality of the problem.

This dissertation also proposes a new approach toward developing highly efficient inorganic/organic solar cell, by presenting a method for enhancement in the optical absorption and overall cell efficiency. Specifically, the approach improves the operation characteristics of inorganic semiconductor (e.g. *Si and a-Si*) and organic (P3HT:PCBM) thin film solar cells by integrating a thin, inhomogeneous, metal-dielectric composite (MDC) electrode at the interface between the transparent electrode and active layer. Through numerical simulations, we show that under solar illumination, surface plasmons are excited within the fractal MDC electrode across an extremely broad range of optical frequencies, trapping the incoming light and ensuring an optimal absorption into the active layer of the solar cells. An analytical model is developed to study the I-V characteristics of the cells, providing a pathway toward achieving optimal efficiency and better understanding of the behavior of charge carriers. Using this model, it is shown that

including gold MDC electrodes can lead to an enhancement in solar cell power conversion efficiency up to 33% higher compared to the benchmark device.

APPROVAL FOR SCHOLARLY DISSEMINATION

The author grants to the Prescott Memorial Library of Louisiana Tech University the right to reproduce, by appropriate methods, upon request, any or all portions of this Dissertation. It is understood that "proper request" consists of the agreement, on the part of the requesting party, that said reproduction is for his personal use and that subsequent reproduction will not occur without written approval of the author of this Dissertation. Further, any portions of the Dissertation used in books, papers, and other works must be appropriately referenced to this Dissertation.

Finally, the author of this Dissertation reserves the right to publish freely, in the literature, at any time, any or all portions of this Dissertation.

Author _____

Date 05/03/16

GS Form 14
(8/10)

DEDICATION

To

My parents,

My grandparents,

To Them I Owe My Life

TABLE OF CONTENTS

ABSTRACT iii

DEDICATION vii

LIST OF FIGURES x

ACKNOWLEDGMENTS xiii

CHAPTER 1 INTRODUCTION 1

1.1 Motivation 1

1.2 Previous Work 3

1.3 Significance of this Work 14

1.4 Organization of the Dissertation 15

CHAPTER 2 LOCAL FIELD DISTRIBUTION IN METAL-DIELECTRIC COMPOSITES 16

2.1 Introduction 16

2.2 Semi-Continuous Metal Films 17

2.3 Surface Plamons in Random Metal-Dielectric Composites 20

2.4 Numerical Methods 21

2.4.1 Block Elimination Method in 3D 22

2.5 Local Field Distribution Function 29

CHAPTER 3 EFFECTIVE PROPERTIES OF RANDOM COMPOSITES 33

3.1 Effective Conductivity 33

3.1.1 Maxwell-Garnett Approximation 34

3.1.2 Bruggeman's Effective Medium Theory 36

3.2 Critical Exponents 39

3.3 Higher Order Field Moments-Scaling Exponents 43

CHAPTER 4 SEMI-CONTINUOUS METAL-DIELECTRIC COMPOSITES IN THIN FILM SOLAR CELLS 52

4.1 Introduction 52

4.2 Modeling 55

4.2.1 SPESC Based on Organic Active Layer 62

4.2.2 SPESC Based on Inorganic Active Layer 65

4.3 Generation Rate and Optimal Photovoltaic (PV) Solar Cell Efficiency 67

CHAPTER 5 CONCLUSION 76

5.1 Concluding Remarks 76

APPENDIX A BLOCK ELIMINATION CODES IN FORTRAN 79

A.1 Serial Code 80

A.2 Parallel Code Using Message Passing Interface Commands 91

BIBILIOGRAPHY 103

LIST OF FIGURES

Figure 1-1: Schematic showing of Surface plasmon resonance on a metal particle surface 3

Figure 1-2: Lycurgus cup. When light is shone from outside, the cup appears in the green color (it has no light coming through the glass). When light is shone through the body of the cup, it turns from opaque green to a glowing translucent red [4] 4

Figure 1-3: Excitation of surface plasmon mode using different techniques (a) Kretschmann configuration; (b) double Kretschmann configuration (c) Otto configuration; (d) NSOM probe excitation; (e) a periodic grating structure excitation; (f) excitation at the metal surface irregularities[11]. 7

Figure 1-4: Fishnet type bulk negative index materials in the optical range [28] (a) Diagram of 21 layer fishnet structure and (b) SEM image of the fishnet structure 11

Figure 2-1: Inhomogeneous metal film consisting of nanometer in size metal particles and clusters deposited on dielectric surface [48] 18

Figure 2-2: Metal-dielectric thin films support morphology dependent surface plasmon (SP) resonances that are characterized by highly enhanced local field moments over very wide frequency range [55] 20

Figure 2-3: (a) The metal-dielectric composite is modeled as a random R-L-C network distributed on a cubic lattice. (b) The local electric potential at a particular site *i* is related to the potentials along conducting paths spanning the entire composites (green dots) 25

Figure 2-4: The spatial distribution of the local field intensity calculated for a random metal-dielectric composite with size $L = 100$ and metal volume fractions $p = 0.25$. In the calculations we consider two different illumination wavelengths (a), (b) $\lambda = 414nm$ and (c), (d) $\lambda = 800nm$. The local intensity distributions are sampled at two horizontal planes within the composite (a), (c) vertical layer $H = 40$ and (b), (d) and vertical layer $H = 60$. In the calculations we consider a silver with parameters: $\varepsilon_b = 5.0$, $\omega_p = 9.1eV$ and $\omega_\tau = 0.021eV$; for the glass substrate, we used $\varepsilon_d = 2.2$... 29

Figure 3-1: Geometry of the composite with metal inclusions of permittivity σ_m embedded in dielectric material σ_d whose effective permittivity is given by $\sigma_{eff}(\sigma_e)$... 35

Figure 3-2: Effective conductivity obtained using the Maxwell-Garnett approximation effective medium theory (EMT) with depolarization factor $\eta = 1/3$..... 36

Figure 3-3: Effective conductivity of silver-glass composite for (a) $p = 0.1$, (b) at percolation $p = 1/3$ and (c) for $p = 0.9$. The solid blue and red lines corespond to the real and imaginary parts of the conductivity, respectively. For comparison, we have also included the conductivity (with dashed lines) of bulk silver 37

Figure 3-4: Effective conductivity σ_e of a three-dimensional (3D) composite with size $L = 40$ as function of the volume fraction p for the high conductivity constituent. Inset: a close inspection of the effective conductivity obtained at lower metal volume fractions..... 39

Figure 3-5: (a) Effective conductivity of three-dimensional (3D) random metal-insulator composite at the percolation threshold $p = p_c = 0.2488126$ and as a function of the system size L. (b) The effective conductivity of composites with different sizes is collapsed onto a single universal function f, (see. Eq. (3.7)), when calculated vs. the compound parameter $x = \Delta p_c L^{1/\nu} = (p - p_c)L^{1/\nu}$. In the insert, the power law behavior of the universal function in close proximity to the percolation threshold is examined 42

Figure 3-6:(a) The electric high order field moments M_n as function of the dissipation factor κ.(b) The expected field moments exponents are numerically estimated and fitted to the theoretical result $\chi_n = (n-1)1 - 2\alpha + \gamma + \alpha$, giving an estimate for the SP density of states and localization length exponents α and γ, respectively. In all calculations the lattice size was fixed at $L = 60$ and 20 realizations of the random geometry were used to improved statistics 49

Figure 3-7: The local-field moments $M_{n,0}$ (dots) are calculated with the exact numerical method (BE) and compared to the analytical results with exponents $\alpha = 0.18 \pm 0.02$ and $\gamma = 0.08 \pm 0.02$ (lines).We used $t = 2.02$, $s = 0.76$ and $\nu = 0.88$ from this work and previous estimates [63][77]. In the calculations, we used lattice size of $L = 60$ and have averaged the field moments over 20 realizations..... 51

Figure 4-1: Basic layout of plasmonically enhanced photovoltaic device. Illumination is through a transparent electrode (ITO) with MDC on top of active layer. 58

Figure 4-2: The spatial distribution of the local field intensity calculated for a random metal-dielectric composite with metal volume fractions $p = 0.3$. In the calculations we consider two different illumination wavelengths (a) $\lambda = 414nm$ and (b) $\lambda = 800nm$, metal as Silver and dielectric as Si 59

Figure 4-3: Enhancement of complex part of effective permittivity (metal as silver and dielectric as Silicon) of the active layer when compared to the bare silicon permittivity, which leads to anomalous absorption over a wide frequency range..... 60

Figure 4-4: Optical model of the solar cell with stack of layers of different thickness and dielectric constants. The black and red arrows indicate the transmission and reflection of light within the layers respectively. Illumination is through a transparent electrode (ITO) with MDC on top of active layer 61

Figure 4-5: Basic layout of plasmonically enhanced photovoltaic device with SiO_2/ITO/MDC/P3HT:PCBM/Al. Illumination is through a transparent electrode (ITO) with MDC on top of active layer 62

Figure 4-6: Optical efficiency of SiO_2/ITO/MDC/P3HT:PCBM/Al solar cell as function of the active layer (P3HT:PCBM) thickness and MDC metal concentration. A 20nm MDC is applied for all calculations 63

Figure 4-7: Optical efficiency of SiO_2/ITO/P3HT:PCBM/MDC/Al solar cell as function of the active layer (P3HT:PCBM) thickness and MDC metal concentration. A 20nm MDC is applied for all calculations 64

Figure 4-8: Basic layout of plasmonically enhanced photovoltaic device with SiO_2/ITO/MDC/c-*Si* (a-*Si*:H) /ZnO/Al. Illumination is through a transparent electrode (ITO) with MDC on top of active layer 65

Figure 4-9: Optical efficiency of SiO_2/MCE/*c*-Si/ZnO/Al solar cell as function of the active layer (crystalline Silicon, *c*-Si) thickness and MDC metal concentration. A 20nm MDC is applied for all calculations 66

Figure 4-10: Optical efficiency of SiO_2/MCE/*a*-Si:H/ZnO/Al solar cell as function of the active layer (amorphous Silicon, *a*-Si) thickness and MDC metal concentration. A 20nm MDC is applied for all calculations 67

Figure 4-11: Basic device structure of PN junction silicon solar cell used for modeling 68

Figure 4-12: Optimal efficiency of SiO_2/ITO/ MDCE/ *Si* /ZNO/Al solar cell as function of the active layer (Silicon, *Si*) thickness and MDCE metal concentration 74

ACKNOWLEDGMENTS

I would like to express my sincere gratitude to my advisor, Dr. Dentcho Angelov Genov. His sound advice has been my inspiration throughout my studies at Louisiana Tech University. I am grateful for his valuable feedback and suggestions, for they have greatly added to the value of this dissertation. From him, I learned how to take an idea from its abstract infancy, give it shape, and put it down effectively on paper. I hope to achieve his level of organization and work ethic in my future academic pursuits.

I would also like to thank Dr. Sandra Zivanovic for being patient with my numerous questions and comments (from teaching to research). Dr. Lee Sawyer's encouragement and support throughout my stay at Louisiana Tech was invaluable. Many thanks to Dr. Neven Simicevic, Dr. Long Que, and Dr. John Shaw for agreeing to serve on my dissertation committee and reviewing this work. A fellowship from Louisiana Optical Network Initiative (LONI), obtained through the kind assistance of Dr. Dentcho A. Genov and Dr. Bety E. Rodriguez-Milla, enabled me to utilize the state of art computational facilities at LONI Institute. This work is also funded by the Department of Energy (DOE) and the Consortium for Innovation in Manufacturing and Metals (CIMM).

My deepest gratitude goes to my colleagues at the Computational Electromagnetics Research Lab (Brandon Touchet, Venkatesh K. Pappakrishnan, Pattabhi Raju Mundru, Raj Kumar Vinnakota, Mona Alsaleh, Caylin Vanhook, Neal Blackman) for their constant support and suggestions in writing this dissertation.

Thanks to my parents, Mr. Animilli Gangarju and Mrs. Kilari Janaki, for their wise advice and help in time of need, who made sure that I had the best of opportunities growing up. Their belief in my judgment gave me the confidence to pursue a doctorate degree. I know they will always be there for me.

Most of all, I would like to express my gratitude to my sisters, Sonali, Aravinda and brother-in-law Krishna Prasad Yalagala, for their encouragement and continued support throughout my research. I would also like to thank my friends, Bijoya Chakraborthy, Praneeth Tammineni, Ritesh Nagaram, Vamsee Krishna Gottipati, Venu Madhav, Abhinav Rao Byrneni, Kranthi Kumar Nagapuri, Ravi Teja, Vineel Kanna, Siva, Sashidhar Kothapeta, Le Xu, Saleh Bajaba, Bien Duc, Goof, Eyas Haj, Salah, and Rajivalochan Subramanian, for their inspiration and assistance in helping me to succeed in my doctoral studies.

CHAPTER 1

INTRODUCTION

1.1 Motivation

The random metal-dielectric composites have been the subject of intensive research due to their unique electric and optical properties. The highly inhomogeneous nature of such systems make them notoriously difficult to study, especially in the three dimensional (3D) case. Among the traditional problems facing the theory of random media are the lack of analytical tools and the need for developing highly efficient numerical algorithms that may allow accurate studies of the local electric field distributions, electron and photon localization, and wave and particle transport through percolation systems and nonlinear effects.

To understand the peculiar optical phenomenon related to percolating metal-dielectric composites, a number of effective-medium theories have been proposed, including the Maxwell-Garnett and Bruggeman approaches and their various modifications. However, none of these theories allow exact calculation of the local field fluctuations facilitated by the excitation of highly localized surface plasmons (SP) states in the composites. Attempts to understand the light localization has been made based on the renormalization group method, however, with rather limited success. There are number of fast algorithms (to be discussed below) proposed to determine the effective

conductivity of the composites; however, they are not suitable for studies of the local field fluctuations, which are the main facilitators for the many unique properties of these materials. In 2003, an exact numerical method, called Block Elimination method (BE) was proposed, which is an exact algorithm that allows the numerical investigation of the random composites at any metal concentrations. This method allows the calculation of the local fields in 2D metal-dielectric composites.

Due to insufficient computational and analytical tools, the optical properties and nonlinear phenomena of three dimensional (3D) inhomogeneous materials are still waiting for a complete theoretical description.

This dissertation studies the optical properties of three dimensional random-composite materials, which exhibit anomalous phenomena such as giant enhancements of optical nonlinearities due to collective excitation of surface plasmons (SPs). This is achieved by the introduction of an efficient and exact numerical method, which can be used to calculate not only the effective conductivity of the 3D inhomogeneous metal-dielectric composite materials but also the local-field distributions. Based on the data generated by the numerical studies, a scaling theory is developed for the higher order-field moments, which are responsible for the unique nonlinear optical response of the system. Relying on the knowledge gained on the three dimensional (3D) metal-dielectric composites, this thesis proposes to integrate metal-dielectric composites in the existing thin film solar cells and designs a new type of solar cell, which we refer to as Surface Plasmon Enhanced Solar Cell (SPESC). These studies show that there is a substantial improvement in the photon absorption and also in the optimal photovoltaic (PV) efficiency of the SPESC when compared to the bare counterpart. In summary, the body of

this thesis covers the essentials of surface plasmon physics in three dimensional metal-dielectric composites and leads to new applications in solar cells and bio-chemical sensors.

1.2 Previous Work

As of late, there has been a rapid growth in the crucial innovative work of surface plasmon based structures and devices. Surface plasmons are aggregate charge oscillations that occur at the interface of metals and dielectrics. They can take different forms, extending from freely propagating electron density waves along metal surfaces to localized electron oscillations on metal nanoparticles (Figure 1-1). Their exceptional properties empower an extensive variety of functional applications, including guiding of light and control at the nanoscale, enhanced optical transmission through sub-wavelength gaps, high determination optical imaging beneath as far as possible, and enhanced optical absorption throughout a broadband spectrum.

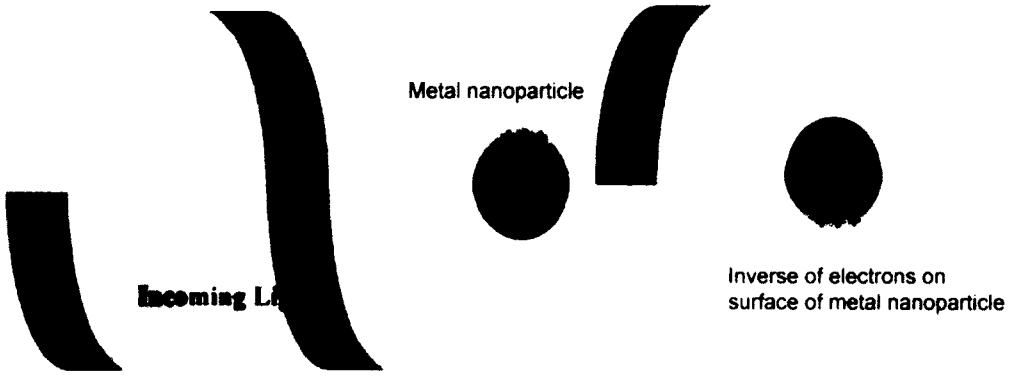

Figure 1-1: Schematic showing of Surface plasmon resonance on a metal particle surface.

Well before researchers set out to examine the novel optical properties of metal nanostructures, artists used to employ metal nano-patrticles in ancient glass accessories to

generate vibrant colors and in stained church window glasses. One of the most popular examples from the antiquity is the Lycurgus cup shown in Figure 1-2. This wonderful piece of art has the property of changing its color depending on the direction of light illumination. Specifically under ambient illumination the cup appears green but changes it color into red if the source of illumination is positioned inside the cup. Now it is understood that this peculiar effect is due to the presence of nano-sized metal particles embedded into the glass that predominantly scatter and absorb light in the green part of the spectra. With the development of the theory of electromagnetism, the first theoretical and experimental studies on surface plasmons were performed at the start of the twentieth century. In the year 1902, Prof. Robert W. Wood observed unique features in the optical reflection of metallic gratings [1]. Around that same time, in 1904, Maxwell Garnett [2] explains the splendid vibrant colors of metal doped glasses by utilizing the then recently developed Drude theory of metals, and the electromagnetic properties of small spheres as inferred by Lord Rayleigh. With an end goal to grow further understanding, in 1908, Gustav Mie created his now famous theory of light scattering from spherical particles [3].

Figure 1-2: Lycurgus cup. When light is shone from outside, the cup appears in the green color (it has no light coming through the glass). When light is shone through the body of the cup, it turns from opaque green to a glowing translucent red [4].

Around fifty years later, in 1956, David Pines theoretically depicted the characteristic energy losses experienced by fast electrons going through metal foils [5], and ascribed these losses to excitations of collective oscillations of free electrons in the metal. In analogy to prior work on plasma oscillations in gas discharges, he named these collective states 'plasmons'. In 1957, Rufus Ritchie published his ground breaking work on electron energy losses in thin films, in which it is demonstrated that plasmon modes can exist close to the surface of metals [6]. This study represents the first complete theoretical depiction of surface plasmons. A year later, John Joseph Hopfield introduced the term "polariton" to describe the coupled oscillations of bound electrons and light inside transparent media [7]. In 1968, about seventy years after Wood's unique perceptions, Ritchie and associates portray the anomalous behavior of metal gratings, regarding surface plasmon resonances energized on the gratings [8]. A noteworthy development in the investigation of surface plasmons was made in 1968 at the point when Andreas Otto, and in addition Erich Kretschmann and Heinz Raether [9], presented techniques for the optical excitation of surface plasmons on metal films, making experiments on surface plasmons open to numerous researchers.

The most common technique for the optical excitation of surface plasmons have been suggested by the Kretschmann method [9], in which a thin metal film is evaporated on top of a glass prism. Photons from a beam impinging from the glass side at an angle greater than the critical angle of total internal reflection tunnel through the metal film and excite surface plasmon polaritons (SPPs) at the metal/air interface as shown in Figure 1-3 (a). Another similar way to excite SPPs using a prism is by adding a second dielectric layer that has a dielectric constant of less than that of the prism, as shown in the

Figure 1-3 (b). Similar to the Kretschmann configuration, is the Otto configuration [10], in which the prism is separated from the metal film by a thin air gap (Figure 1-3 (c)). Total internal reflection takes place at the prism/air interface, exciting SPPs via tunneling to the air/metal interface. This configuration is preferable when direct contact with the metal surface is undesirable. Figure 1-3 (d) depicts the use of near-field evanescent wave excitation of surface plasmon mode in near-field scanning optical microscope (Near-field Scanning Optical Microscopy, NSOM) probe (Fiber Tip). Such technique is used by structurally varying the surface of a metal-dielectric interface, which makes it possible to resonantly couple the incident light with surface plasmon polaritons, which the process can also be used to enhance the optical transmission through the probe's apertures, which are much smaller than the incident wavelength. This mechanism is similar to Otto configuration (Figure 1-3 (c)), but only allowed under the probe localized excitation. A common way to launch SPPs with a set wave vector is through the use of metal grating, as shown in Figure 1-3 (e) or if one seeks broad excitation using localized imperfection on the metal surfaces, for instance metal nanoparticles, as shown in Figure 1-3 (f).

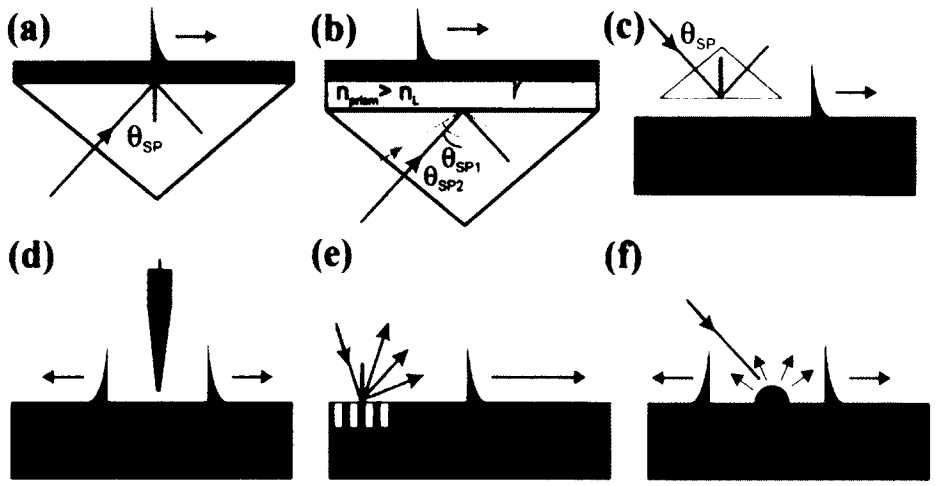

Figure 1-3: Excitation of surface plasmon mode using different techniques (a) Kretschmann configuration; (b) double Kretschmann configuration (c) Otto configuration; (d) NSOM probe excitation; (e) a periodic grating structure excitation; (f) excitation at the metal surface irregularities[11].

In the seventies, the experimental excitation and theoretical treatment of SPPs on metal dielectric interfaces were a well-established discipline, referred to as plasmonics; however at the time there was little work on metal nanoparticles and composites. In 1970, over sixty years after Garnett's work on the bright colors of the metal doped glasses, Uwe Kreibig and Diminish Zacharias performed the first study in which they compared the electronic and optical responses of gold and silver nanoparticles [12]. In their work, for the first time, they were able to portray the optical response of metal nanoparticles in terms of excitation of localized surface plasmons (LSPs). As the field kept on developing and the significance of the coupling between the oscillating electrons and the electromagnetic field turn out to be more evident, Stephen Cunningham and co-workers introduced the presently used terms to identify the propagating surface plasmon states: i.e., surface plasmon-polariton (SPP) in 1974 [13].

Another disclosure in the territory of metal based optics happens in that same year, when Martin Fleischmann and his team observed strong Raman scattering from pyridine molecules in the region of roughened silver surfaces [14]. Their work showed that Raman scattering – an exchange of energy between photons and sub-atomic vibrations – was enhanced by the strong electromagnetic fields in close proximity to the rough silver surfaces, an effect facilitated by excitation of localized surface plasmons (LSPs). This experimental observation prompted the development of the now well established discipline of Surface Enhanced Raman Scattering (SERS). All these disclosures have set the stage for the present surge in surface plasmon nanophotonics.

By now it has been realized that, surface plasmon polaritons (SPPs) are electromagnetic excitations propagating at the interface between a dielectric and a conductor, evanescently confined in direction perpendicular to the interface. The SPPs have been also considered in configuration similar to photonic crystals, i.e. dielectric materials with periodic arrangements of scattering elements, such as holes imprinted inside a dielectric host. In a photonic crystal, both the size and the periodicity of the index modulations are of the order of the wavelength λ in the material. In the SPP analogue, a metal surface is imprinted with a periodic arrangement of surface protrusions or recesses. In contrast to photonic crystals, when the size and the periodicity of the scattering elements are significantly smaller than λ, there is an equally intriguing possibility for designing artificial materials with a controlled photonic response called metamaterials. Therefore, because of the SPPs sub-wavelength characteristics, periodic or semi-periodic arrangements of metal and dielectric elements may serve the purpose of creating new artificial optical materials, in analogy to atoms in conventional materials found in nature.

Since the sub-wavelength scale the electric and magnetic fields are essentially decoupled, $\varepsilon(\omega)$ and $\mu(\omega)$ can often be controlled independently by the use of appropriately shaped inclusions. The corrugated, perfectly-conducting surfaces are an example of a metamaterial with an engineered electric response, $\varepsilon(\omega)$. Such an interface can be described as an effective medium, with a plasma frequency ω_p controlled by the geometry. Metamaterials designs that may allow engineering of both $\varepsilon(\omega)$ and $\mu(\omega)$ has been recently suggested to developed unique material that can manifest a negative refractive index $n = \sqrt{\mu\varepsilon} < 0$ within pre-set frequency range.

In 1967, Vector Veselago provided the theoretical background behind the materials with negative index of refraction (NIR) showing that such materials can be created if ε and μ are simultaneously negative [15][16]. He also showed that having such a material will result in changes of the laws of optics. Specifically, Veselago claimed that materials with NIR would not violate the laws of physics but would provide unusual phenomenon such as reversed Snell's law and Doppler shifts [15][17]. However, Veselago's work was ignored because no material with $\varepsilon < 0$ and $\mu < 0$ exist in nature. Indeed, while there are many naturaly existing materials that can show broad-band negative permittivity (metals), there is no naturally existing material that possesses a negative permeability [16].

The first designed metamaterial with simultaneously negative permittivity and permeability was proposed by Pendry in 1999[7]. The Pendry design consists of periodic metallic thin wires with a lattice constant much smaller than the wavelength of light to provide a negative permittivity ($\varepsilon < 0$) and negative permeability ($\mu < 0$), but this structure had a limited magnetic moment [7]. Later, he introduced a split ring resonator (SRR) in tandem with lattice of paralell metallic wires to enhance the magnetic moment of

the structure. One of the most famous applications of the metamaterials is in the possibility to create a perfect lens with resolution surpassing the conventional diffraction limit. In 2000, Pendry [18] proposed such a superlens based on NIM (with $n = -1$), which can be realized at microwave frequencies. In 2000, Smith and his group combined SRR and metallic wire made of copper to show negative index of refraction. This structure manifested a negative index of refraction at 4.8 GHz, with the effect demonstrated through direct transmission measurements [18]. The first experiment that demonstrated negative refraction at microwave frequency was performed by Shelby *et. al.* in 2001. [19][20]. This design relied on split ring resonators (SRR) to achieve negative permeability and wire stripes centered on the SRRs to provide a negative permittivity. The first three dimensional bulk NIM with centimeter sizes was fabricated in 2003 [21][22]. This structure showed a negative index of refraction by using Snell's law experiment and numerical simulation. The experimental results were found to be in agreement with the numerical simulations. In 2004, Smith and his collogues [23] fabricated the first THz NIMs by shrinking the size of SRR to a few micrometers. Shrinking the size of the resonator allowed obtaining a negative permeability at higher frequency. Using three different sizes of SRRs negative permeability was observed in the frequency range 0.8 to 1 THz.

Linden and his group fabricated a single ring resonator made of copper by reducing the size of the ring to nanometer sizes and futher up-shifting the resonant frequency up to 100 THz[25]. To have a magnetic response at optical frequencies, however, one needs to dramatically shrink the sizes of the SRRs, which is not currently feasible due to the complex geometry and the need to make the gaps in the SRR in the order of a few nanometers. To overcome this problem, Sarychev *et. al.* [26] proposed a different concept

based only on pairs of metal nanowires, which shows negative refraction index at near-Infrared (NIR) frequencies. However, due to the necessity for top down micro-manufacturing and high intrinsic losses the nanowire system is not applicable for development of bulk (multilayer) EMMs.

Following an identical design Shalaev *et.al.* [27] experimentally demonstrated the first optical metamaterial with NIR. The proposed structure consists of parallel metal nanorods separated by a dielectric material as a unit cell. This structure showed an effective permeability at 200 THz. Only recently, in 2008, did the first true bulks NIM based on alternative layers of silver and magnesium fluoride in the form of a fishnet structures as it is shown in Figure 1-4, was successfully developed and tested showing direct evidence of negative refraction at optical frequencies [28].

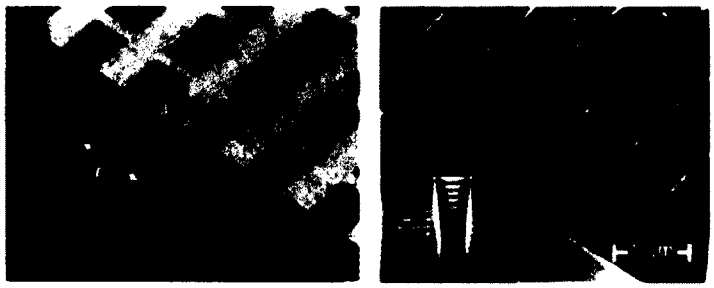

Figure 1-4: Fishnet type bulk negative index materials in the optical range [28] (a) Diagram of 21 layer fishnet structure and (b) SEM image of the fishnet structure.

In 2011, Choi et al [29] designed a metamaterial that extremely bends the light in opposite directions compared to the naturally existing materials. This structure showed a very high negative refractive index over a broad band of THz frequencies.

A separate approach toward negative index of refraction is based on anisotropic dielectric materials. In 2007, Hoffman [30][31] and his group fabricated a three dimensional anisotropic semiconductors metamaterial. The authors use semiconductors to

reduce the losses and simplify the fabrication. One of the most fascinating features of this design is that it provides negative refraction for transversal magnetic (TM) field for all incident angles at mid- infrared frequencies, while the transversal electrical (TE) field has a positive index of refraction.

J. Yao and his coauthors at the University of California, Berkeley observed negative refraction at optical frequencies for a bulk metamaterial consisting of silver nanorods embedded in alumina template [32]. The separation distance between the rods was set to be much smaller than the wavelength of impinging light. Shining a laser beam at different angles demonstrates a negative refraction for TM polarized light, while TE polarized light undergoes a positive refraction.

Finally, it must be emphasized that controlling light on scales much smaller than the light wavelength can be achieved by excitation of SPPs, owing to their unique optical properties described above. SPPs exhibit potential applications in subwavelength optics (e.g. waveguides and sources), near-field optics, SERS, data storage, solar cells, chemical sensors, and biosensors [33, 34].

In summary, it is now well understood that surface plasmons excitations in metal particles embedded in a host dielectric media are associated with resonant collective electron oscillations because of the displacement of free electrons from their equilibrium position in the nano particles, leading to induced by the external field polarization; this polarization in turn, results in restoring force that causes electron oscillations. When the particles are embedded in a host medium, and when they can form objects of complex geometry, such as fractals, self-affine films, and percolation metal-dielectric films, the light-induced oscillating dipoles of different particles interact with each other, forming

collective optical excitations of the whole system. These oscillations span broad spectral range covering optical and infrared (IR) frequencies and are manifested through electromagnetic energy localization in small spatial regions, "hot spots".

The problem under consideration in this thesis is how the collective optical response of a complex random system of metal nanoparticles can be expressed in terms of the optical properties of individual particles that are known. In other words, it is imperative to better understand how the global morphology (i.e. geometry) of a nanostructured random medium affects its collective optical response. Historically, a number of effective-medium theories have been proposed to describe the optical properties of random films, including the Maxwell-Garnett [2] and Bruggeman [35] approaches and their various modifications. These theories assume that the electromagnetic properties of the composites can be homogenized and do not take interactions between the particles into consideration. The renormalization group method [36, 37] is also widely used to calculate the effective dielectric response of two-dimensional percolating films near the percolation threshold. However, none of these theories allows for studies of the local field fluctuations and the relevant optical effects resulting from these fluctuations. High efficiency algorithms have been also proposed to determine exactly the composite's effective conductivity, such as the Frank-Lobb method [38], and the transfer matrix method [39], but they could not provide an insight into the fluctuating nature of the local-fields. Although Zekri-Bouamrane-Zekri (ZBZ) suggested a substitution method [40] to calculate the local-field distributions, the results were somehow contradictory to other theoretical and experimental data. Finally, in 2003, an exact algorithm was proposed that allows the numerical investigation of random two

dimensional (2D) composites at arbitrary metal volume fractions [41]. This method, referred to as block elimination (BE), allows the exact calculation of the local fields and related macroscopic quantities.

1.3 Significance of this Work

The available published work does not address the problem of surface plasmions oscillations in three dimensional metal-dielectric composites. This dissertation work studies the electromagnetic response of random media in three dimensions (3D) by developing new numerical codes and relevant analytical theory. As a practical application the developed theory is utilized to provide a functional characterization and optimization of a novel surface plasmon enhanced solar cell (SPESC). The specific contributions of this dissertation are:

1. Develop a comprehensive, highly efficient numerical model referred to as Block Elimination Method (BEM) to tackle the problem of light interaction with large scale, highly inhomogeneous, bulk (3D) media.
2. Develop a parallel code, which implements the BEM by utilizing multi core processing and packages such as MPI.
3. Study for a first time the local electric response of the random metal-dielectric films in three dimensions (3D), including sampling of the exact local field distribution functions and the effective conductivity of the media.
4. Demonstrate the nature of surface plasmon (SP) localization for a first time in the 3D case.
5. Developing a scaling theory for the higher order-field moments, which are responsible for the nonlinear optical response of the random system.

6. Design a new type of solar cell, here referred to as Surface Plasmon Enhanced Solar Cell (SPESC), and estimate its optical and total electrical efficiency.

The work done for this dissertation has contributed to the following publications: Geometrical phase transition and local field moments in metal-dielectric composite media [42]. Semi continuous metal dielectric composites in thin-film silicon solar cell [43], and Analytical Model of Thin-Film Silicon Solar Cell [44].

1.4 Organization of the Dissertation

The remainder of the dissertation is organized as follows. Chapter 2 presents an overview of the electromagnetic properties of metal-dielectric composites. It also presents the Block Elimination methods and a comprehensive study of the local field fluctuations present in the random composites through sampling of the relevant intensity distribution functions near and away from percolation and for frequencies across the optical frequency range. Chapter 3 obtains accurate estimates of the scaling exponents related to the composite effective conductivity and correlation length. A scaling analytical theory is developed for the higher order local field moments and shown to be in excellent agreement with the numerical simulations. Chapter 4 provides an effective approach to couple the electromagnetic response of metal-dielectric composite to enhance light absorption, photocurrent generation, and therefore, the quantum efficiency of inorganic/organic semiconductor photovoltaic/photodetector devices. Chapter 5 provides the concluding remarks.

CHAPTER 2

LOCAL FIELD DISTRIBUTION IN METAL-DIELECTRIC COMPOSITES

In this chapter we study nano-structured random-composite materials, which exhibit anomalous phenomena such as giant enhancements of optical nonlinearities due to collective excitation of surface plasmons (SPs). We introduce an efficient and exact numerical method for calculation of the effective conductivity and local-field distributions in 3D inhomogeneous metal-dielectric composite materials.

2.1 Introduction

The optical properties of metal-dielectric composites are unique when compared to the constituent bulk metal and dielectric components [45,46]. For example, anomalous absorption and extinction that occur in visible and infrared spectral ranges do not take place in bulk metal or dielectric. Such a broad spectral response is only possible at metal concentrations close to the percolation threshold where, according to the percolation theory [47], fractal clusters with arbitrary sizes and shapes are present in the composite. For metal concentrations below percolation threshold, the interaction of the composites with the incident electromagnetic field is weak, and the composites becomes semi-transparent for frequencies that are away from the single particle plasmon resonance.

The random composites are binary metal-dielectric substrates, usually nano-manufactures based on laser ablation and sputtering of metal targets. These nano-structured composite materials are of significant practical interest because they can lead to dramatic enhancement of linear and nonlinear optical processes across broad spectral range, including the visible and infrared parts of the spectrum. In particular, percolation metal-dielectric films can be employed for surface-enhanced spectroscopy with unsurpassed sensitivity, and for developing optical elements, such as optical switches and efficient optical filters, with transparency windows that can be induced by local photo-modification of the composite films.

2.2 Semi-Continuous Metal Films

Semi-continuous films also referred as random metal-dielectric films, form a large class of random media with high potential for various applications in optics bio and chemical sensing and optoelectronics. These films can be fabricated by thermal evaporation or sputtering of metal onto an insulating substrate (Figure 2-1). As the film grows, the surface filling factor of the metal particles sitting on the dielectric substrate increases, resulting in metal coalescence into irregularly shaped clusters of various sizes. At the percolation threshold the size of the metal clusters diverges, resulting in the formation of a continuous conducting path (spanning cluster) across the entire sample. As a result, the composite undergoes a geometrical metal-dielectric phase transition. The spanning (backbone) cluster is self-similar or fractal in nature. The concept of self-similarity plays an important role in explaining various properties of the percolation systems, including its broadband AC response [49, 50]. At higher surface coverage, the

film is mostly metallic, with voids of irregular shape. With further coverage increase, the film recovers the bulk metal response.

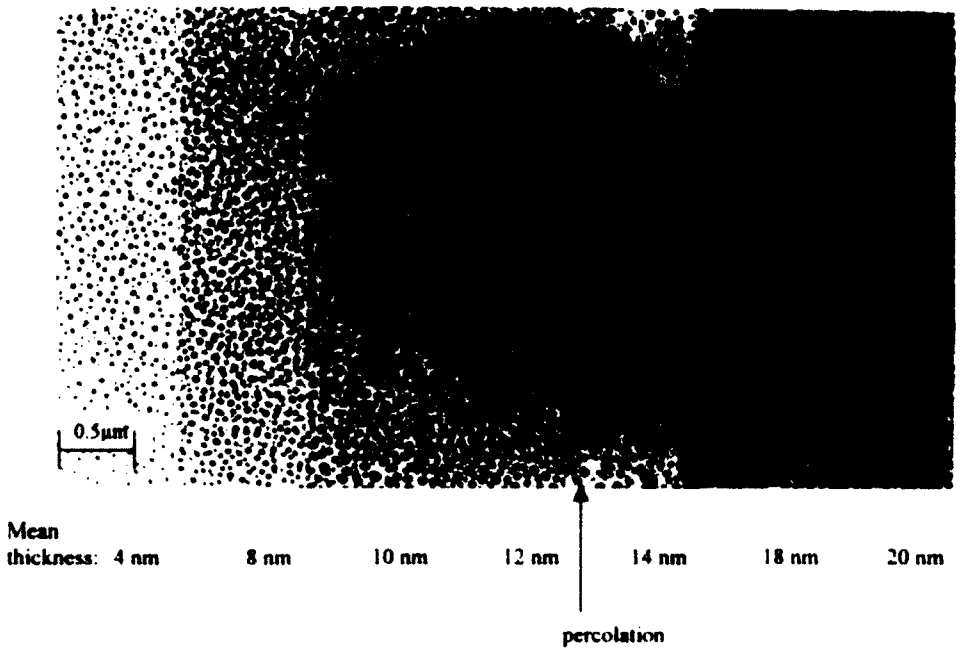

Figure 2-1: Inhomogeneous metal film consisting of nanometer in size metal particles and clusters deposited on dielectric surface [48].

The optical properties of the percolating metal-dielectric films demonstrate anomalous phenomena that are absent in the bulk metal and dielectric components. The anomalous absorption in the near-infrared spectral range for critical metal concentrations (percolation) has been demonstrated in numerous experimental studies [57-59]. This also leads to unusual behavior of the transmittance and reflectance of the film. Typically, the transmittance is much higher than in continuous metal films, whereas the reflectance is much lower [49-51]. As the interaction of incident radiation with the percolation system is very sensitive to the micro- and macroscopic topology of the films, the films transport and optical properties are dependent on an extremely large network of conducting channels. The direct result is a broadband optical response characterized with localization

of the local field in the weak points of the channels, resulting in much larger nonlinear susceptibilities at zero and finite frequencies compared to the bare component materials [52].

Nonlinear electrical and optical properties of percolating metal-dielectric composites have attracted much attention in recent years [52]. The distinguishing feature of random media, namely the enhancement of the optical nonlinearities in its components, was recognized very early on and nonlinear conductivities have been studied intensively in the last few decades [51, 52].

For composite materials containing metal particles with negative real and small imaginary parts of the dielectric constant, the local field fluctuations can be strongly enhanced in the optical and infrared spectral ranges. The local field enhancement (Figure 2-2) is due to excitation of surface plasmon resonances in clusters of metallic granules [51-55]. The strong localization (fluctuations) of the local electric fields leads to enhancement of various nonlinear effects. As such, percolation composites are of high practical importance as prospective media to provide intensity-dependent dielectric functions and, in particular, as nonlinear optical switches, filters, and bi-stable elements.

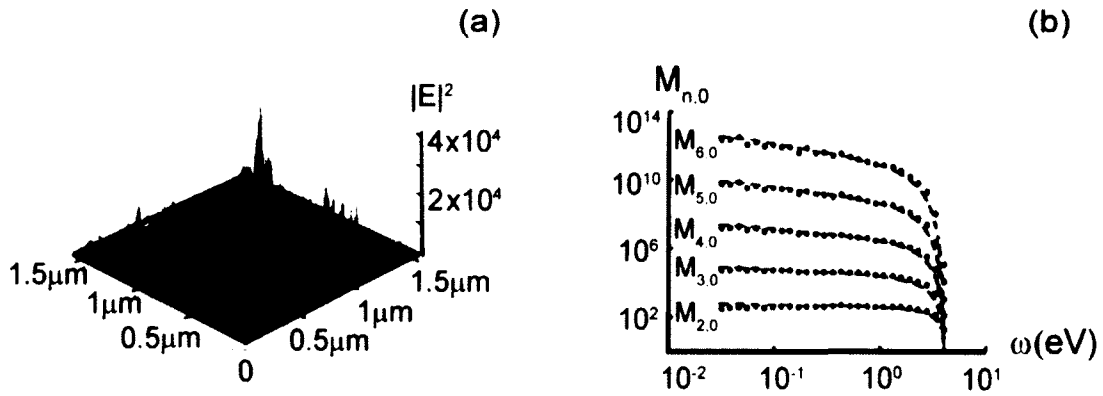

Figure 2-2: Metal-dielectric thin films support morphology dependent surface plasmon (SP) resonances that are characterized by highly enhanced local field moments over very wide frequency range [55].

2.3 Surface Plamons in Random Metal-Dielectric Composites

In the optical spectral range, where the frequency ω is much larger than the relaxation rate $\omega_\tau = \tau^{-1}$, a semi-continuous metal film can be understood as a three-dimensional *RLC* network [51, 56, 57]. The capacitance *C* is due to the gaps between metal grains filled by dielectric material with a dielectric constant ε_d. The inductive *R-L* elements represent the metallic grains. The bulk metal permittivity is well described by the Drude model: Eq. (2.1)

$$\varepsilon_m = \varepsilon_b - \frac{\omega_p^2}{(\omega^2 + i\omega\omega_\tau)}, \qquad \textbf{Eq. 2-1}$$

where, ε_b is a contribution to ε_m due to interband transitions, ω_p is the plasma frequency, and $\omega_\tau = \tau^{-1} \ll \omega_p$ is the relaxation rate. In the high-frequency range considered here, losses in metal grain are small, i.e. $\omega_\tau \ll \omega$. Therefore, the real part of the metal-dielectric function is much larger in magnitude than the imaginary part, and it is negative for frequencies ω less that the "renormalized" plasma frequency defined as $\tilde{\omega}_p = \omega_p/\sqrt{\varepsilon_b}$.

Thus, the metal conductivity is almost purely imaginary and metal grains can be, as mentioned above, thought of as *R-L* elements, with the active component much smaller than the reactive one. Note that this *R-L-C* analogy is only to be used for illustrative purposes; the studies outlined below are general and do not rely on any approximations.

It can be shown that in the quasi-static case the effective conductivity/permittivity of the random two dimensional binary percolating composites ($p = p_c$), is given as $\varepsilon_e = \sqrt{\varepsilon_d \varepsilon_m}$ [57]. If we neglect metal losses and for frequencies smaller than the renormalized plasma frequency $\tilde{\omega}_p$, the metal-dielectric constant ε_m is real and negative. If we also neglect possible small losses in the dielectric substrate, assuming that ε_d is real and positive. As stated above, $\varepsilon_e$is purely imaginary for $\omega < \tilde{\omega}_p$. Therefore, a film consisting of loss-free metal and dielectric grains is reflective for $\omega < \tilde{\omega}_p$ and transparent for $\omega > \tilde{\omega}_p$. In our studies we consider the former case. The strong reflectance of the films is facilitated by rearrangement of the conduction electrons in the metal, which expels the incident radiation. This results in strong local energy localization in the dielectric gaps. For near loss-free films, the electromagnetic energy stored in the system can be very large. Indeed for noble metals in the optical and near-infrared spectral ranges $\omega_\tau \ll \omega$ one can anticipate very strong field fluctuations and giant enhancement of optical nonlinearities [52].

2.4 Numerical Methods

It can be shown that in the quasi-static case the effective conductivity/permittivity of the random two dimensional binary percolating composites ($p = p_c$), is given as $\varepsilon_e = \sqrt{\varepsilon_d \varepsilon_m}$ [57]. If we neglect metal losses and for frequencies smaller than the renormalized

plasma frequency $\tilde{\omega}_p$, the metal-dielectric constant ε_m is real and negative. If we also neglect possible small losses in the dielectric substrate, assuming that ε_d is real and positive. As stated above, $\varepsilon_e$is purely imaginary for $\omega < \tilde{\omega}_p$. Therefore, a film consisting of loss-free metal and dielectric grains is reflective for $\omega < \tilde{\omega}_p$ and transparent for $\omega > \tilde{\omega}_p$. In our studies we consider the former case. The strong reflectance of the films is facilitated by rearrangement of the conduction electrons in the metal, which expels the incident radiation. This results in strong local energy localization in the dielectric gaps. For near loss-free films, the electromagnetic energy stored in the system can be very large. Indeed for noble metals in the optical and near-infrared spectral ranges $\omega_\tau \ll \omega$ one can anticipate very strong field fluctuations and giant enhancement of optical nonlinearities [52].

2.4.1 Block Elimination Method in 3D

In this section we provide a short introduction to the Block Elimination (BE) method, which is used to study the local electric response of random metal-dielectric films in three dimensions (3D). We consider composites of metal particles with characteristic sizes much smaller than the wavelength of illumination. Under such restrictions, one can neglect retardation effects and seek a solution for the local potential in the quasi-static approximation. Assuming time-harmonic fields, currents and charge densities of the form $e^{-i\omega t}$, we can write the Gauss law $\vec{\nabla} \cdot \left[\varepsilon(\vec{r},\omega)\vec{E}(\vec{r},\omega)\right] = \rho(\vec{r},\omega)$ in terms of a complex valued conductivity/permeability of the composite. The procedure relies on substituting the charge density through the charge conservation $\rho(\vec{r},\omega) = -(i/\omega)\vec{\nabla} \cdot \vec{J}(\vec{r},\omega)$, where $\vec{J} = \sigma_c(\vec{r},\omega)\vec{E}(\vec{r},\omega)$ is the conduction current density, σ_c and $\vec{E}$ are the local conductivity and electric field, respectively. The generalized Kirchhoff law,

which now includes both the displacement and conduction currents and is characterized by a complex valued conductivity $\sigma = -i\omega\varepsilon^* = \sigma_c - i\omega\varepsilon$, is thus written as:

$$\vec{\nabla} \cdot \left[\sigma(\vec{r},\omega)\vec{\nabla}\varphi(\vec{r},\omega)\right] = \vec{\nabla} \cdot \left[\sigma(\vec{r},\omega)\vec{E}_0\right], \qquad \textbf{Eq. 2-2}$$

where we have split the local electric field $\vec{E}(\vec{r},\omega) = \vec{E}_0 - \vec{\nabla}\varphi(\vec{r},\omega)$ into a fluctuating and constant (applied) field components. In the optical and infrared spectral range, the metal components can be modeled using a complex valued conductivity given by the Drude model $\sigma = -i\omega\varepsilon_0\left[\varepsilon_b - \omega_p^2/(\omega^2 + i\omega\omega_\tau)\right]$, where, ε_b is a contribution due to the lattice electrons, ε_0 is the permittivity of free space, ω_p is the plasma frequency, and $\omega_\tau \ll \omega_p$ is the relaxation rate. As discussed in the preceding section in the high-frequency range, considered here, losses in metals are small, i.e. $\omega_\tau \ll \omega$. Therefore, the metal permittivity is predominantly real valued and negative for frequencies less that the "renormalized" plasma frequency $\tilde{\omega}_p = \omega_p/\sqrt{\varepsilon_b}$. Thus, the metal-dielectric composites can be considered as a random *RLC* circuit network with the metal components described by *RL* elements while the dielectric host is represented by distributed capacitances [53, 54, 55]. This immediately leads to the conclusion that for optical and infrared frequencies the composites should manifest *RLC* resonances and excitations of charge density states, i.e. surface plasmons (SPs). Since the capacitance of the dielectric gaps and the inductance of the metal clusters are proportional to the characteristic length scale ($C \sim l$ and $L \sim l$), the expected resonance frequencies should scale as $\omega_R = 1/\sqrt{LC} \sim 1/l$. Because of metal volume fractions close to the percolation threshold, the composite materials are fractal in nature and clusters with arbitrary sizes and shapes and because they are present in the composites [67], a broad frequency response is expected. This phenomenon is well documented for planar semi-continuous metal films and is best

manifested at percolation through broad absorption spectra [22, 52, 66, 67]. While the RLC model can provide a qualitative understanding of the system response a quantitative description of the problem is required.

Here, we solve Eq. (2.2) by implementing a finite difference (FD) scheme and discretize the local potential on a cubic lattice with size L. Each lattice site is connected to its nearest neighbors through six bonds, each prescribed a metal σ_m or insulator σ_d complex conductivity with probability p and $1-p$, respectively (Figure 2-3). The resulting generalized Kirchhoff's equations take a discrete form as shown in Eq. (2.3):

$$\sum_{s}\sum_{[i,j,k]} \sigma_{ijk}^{s}\vec{\nabla}\varphi(i\Delta x, j\Delta y, k\Delta z)\big|_{s} = \sum_{s}\sum_{[i,j,k]} \sigma_{ijk}^{s}\vec{E}_0\big|_{s}, \qquad \textbf{Eq. 2-3}$$

where the bracket $[i,j,k]$ indicates summation of the local currents along bonds connecting a lattice site $\{i,j,k\}$ with its nearest neighbors, and the index $s=\{x,y,z\}$ identifies the three polarization directions.

The system of Eqs. (2.3), can be written in short form as $\hat{H}\cdot\vec{\Phi}=\vec{J}_0$, where $\hat{H}$ is the $L^3\times L^3$ Kirchhoff's matrix, while the vectors $\vec{\Phi}$ and $\vec{J}_0$ consist of the local potentials and externally induced local currents, respectively. The Kirchhoff's matrix is a symmetric sparse random matrix with diagonal elements given by the sum $H_{pp}=\sum_s\sum_{[i,j,k]}\sigma_{ijk}^{s}$ of all bond conductivities σ_{ijk}^{s}, connecting the $\{i,j,k\}$ site with its nearest neighbors, with the matrix's diagonal indexes given as $p=i+(j-1)L+(k-1)L^2$.

The off-diagonal elements of the Kirchhoff's matrix are related to the individual bond conductivities and are given as $H_{p,p+1}=-\sigma_{ijk}^{x}$, $H_{p,p+L}=-\sigma_{ijk}^{y}$ and $H_{p,p+L^2}=-\sigma_{ijk}^{z}$. The system of equations (Eq. 2.3) is solved using the BE procedure [19], which here has been extended in the 3D case. The BE method relies on reducing the Kirchhoff

matrix into $3L$ separate block matrices each of size $L^2 \times L^2$. The elimination procedure is then formulated with respect to this set of sub-matrices reducing the operational memory requirement from $O(L^9)$ to $O(L^5)$. The total number of operations required to obtain a solution is also reduced to $O(L^7)$, which compares favorably with the $O(L^9)$ operations needed if using classical Gaussian or LU (for symmetric matrices) elimination methods.

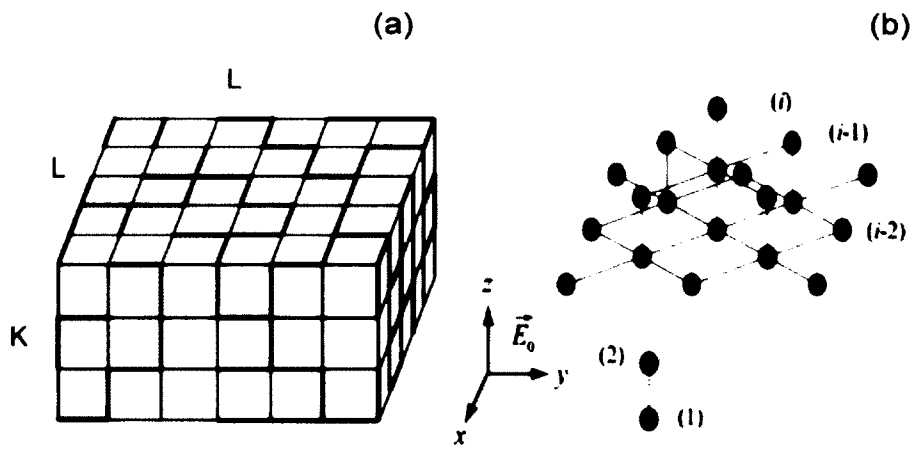

Figure 2-3: (a) The metal-dielectric composite is modeled as a random R-L-C network distributed on a cubic lattice. (b) The local electric potential at a particular site i is related to the potentials along conducting paths spanning the entire composites (green dots).

Under this labeling, the KH matrix $\hat{H}$ acquires a block type structure and for $L = 5$ is written as:

$$\hat{H} = \begin{pmatrix} \hat{h}^{(11)} & \hat{h}^{(12)} & 0 & 0 & \hat{h}^{(15)} \\ \hat{h}^{(21)} & \hat{h}^{(22)} & \hat{h}^{(23)} & 0 & 0 \\ 0 & \hat{h}^{(32)} & \hat{h}^{(33)} & \hat{h}^{(34)} & 0 \\ 0 & 0 & \hat{h}^{(43)} & \hat{h}^{(44)} & \hat{h}^{(45)} \\ \hat{h}^{(51)} & 0 & 0 & \hat{h}^{(54)} & \hat{h}^{(55)} \end{pmatrix}, \qquad \textbf{Eq. 2-4}$$

where $\hat{h}^{(ij)}$are $L^2 \times L^2$diagonal matrices, with the off-diagonal matrices $\hat{h}^{(ki)} = \hat{h}^{(ik)}(k \neq l)$ connecting the *k-th* layer with the *l-th* layer and vice versa. The matrices in the right upper and left bottom corners of the KH are due to the periodical boundary conditions. For large sizes L, the majority of the block matrices $\hat{h}^{(ij)}$ are effectively zero and applying Gaussian elimination will be a very inefficient way to solve the problem. In fact, in a process of elimination of all block elements below $\hat{h}^{(11)}$ the only matrix elements that will change are $\hat{h}^{(11)}, \hat{h}^{(12)}, \hat{h}^{(15)}, \hat{h}^{(21)}, \hat{h}^{(22)}, \hat{h}^{(51)}$ and $\hat{h}^{(55)}$. Thus, to eliminate the first block column of the KH we can instead work with the following $2L^2 \times 2L^2$ block matrix:

$$\hat{S}^{(1)} = \begin{pmatrix} \hat{h}^{(11)} & \hat{h}^{(12)} & \hat{h}^{(15)} \\ \hat{h}^{(21)} & \hat{h}^{(22)} & 0 \\ \hat{h}^{(51)} & 0 & \hat{h}^{(55)} \end{pmatrix}. \qquad \textbf{Eq. 2-5}$$

To eliminate all elements below the diagonal in the first block column of matrix $\hat{S}^{(1)}$, we apply a standard Gaussian elimination procedure, whereby using the diagonal elements of the block matrix $\hat{h}^{(11)}$into a triangle matrix $\hat{h}^{*(11)}$ and simultaneously eliminate $\hat{h}^{(21)}, \hat{h}^{(51)}$. After the first step of the block elimination is completed, the matrix $\hat{H}$ has the following form:

$$\hat{H}^{(1)} = \begin{pmatrix} \hat{h}^{*(11)} & \hat{h}^{*(12)} & 0 & 0 & \hat{h}^{*(15)} \\ 0 & \hat{h}^{*(22)} & \hat{h}^{(23)} & 0 & \hat{h}^{(25)} \\ 0 & \hat{h}^{(32)} & \hat{h}^{(33)} & \hat{h}^{(34)} & 0 \\ 0 & 0 & \hat{h}^{(43)} & \hat{h}^{(44)} & \hat{h}^{(45)} \\ 0 & \hat{h}^{(52)} & 0 & \hat{h}^{(54)} & \hat{h}^{*(55)} \end{pmatrix}, \qquad \textbf{Eq. 2-6}$$

whereby the asterisk superscript we denote all blocks that have changed in the elimination process. The two new block elements $\hat{h}^{(25)}$and $\hat{h}^{(52)}$ appear due to the interactions of the first row with the second and fifth rows, respectively.

In the next step of the matric elimination, we again apply the above described procedure for the minor of the matrix $\hat{H}^{(1)}$; therefore we work again with a $2L^2 \times 2L^2$matrix:

$$\hat{S}^{(2)} = \begin{pmatrix} \hat{h}^{*(22)} & \hat{h}^{(23)} & \hat{h}^{(25)} \\ \hat{h}^{(32)} & \hat{h}^{(33)} & 0 \\ \hat{h}^{(52)} & 0 & \hat{h}^{*(55)} \end{pmatrix}. \qquad \textbf{Eq. 2-7}$$

Repeating with $\hat{S}^{(2)}$, all the operations we performed on $\hat{S}^{(1)}$, we put $\hat{h}^{*(22)}$ in a bock upper triangular configuration by eliminating $\hat{h}^{(32)}$ and, $\hat{h}^{(52)}$. We continue this procedure until the entire KH is converted into triangular form, with all the elements below the diagonal being zero. The backward substitution for a triangular matrix is straightforward; namely, we obtain first the site potentials in the *L-th* row (the fifth row, in our example) and then, by calculating the potentials, in the (*L-1*)*-th* row, and so on, until the potentials in all rows are obtained.

Note that the block elimination procedure, similarly to the Gaussian elimination, is numerically exact and well suited for parallel computing. Due to the random nature of the problem to acquire good statistics, such as in calculating the effective conductivity of the composite, one needs to perform a large number of separate calculations for different realizations of the composite microstructure. In the studies that follow, we use a simple multi-processor version of the code based on the Single Process Multiple Data (SPMD) technique. This parallelization technique involves simultaneous use of multiple processors

sharing input/output data with a single parent processor using Message Passing Interface (MPI) commands.

A typical example of simulation outputs is shown in Figure 2-4, where the local intensity fluctuations at two different lattice planes are calculated for two different wavelengths. Similarly to the two-dimensional case, investigated elsewhere [19, 45-48], we observe strong energy localization and broad frequency response, consistent with the *RLC* model. The fluctuating electric field intensities at the "hot spots" can surpass the incident field intensity by factors higher than 10^3. The spatial separation of the local peaks, as well as their absolute magnitudes, are found to increase with the wavelength, which is again consistent with the size dependent scaling of the resonance frequencies predicted by the *RLC* model.

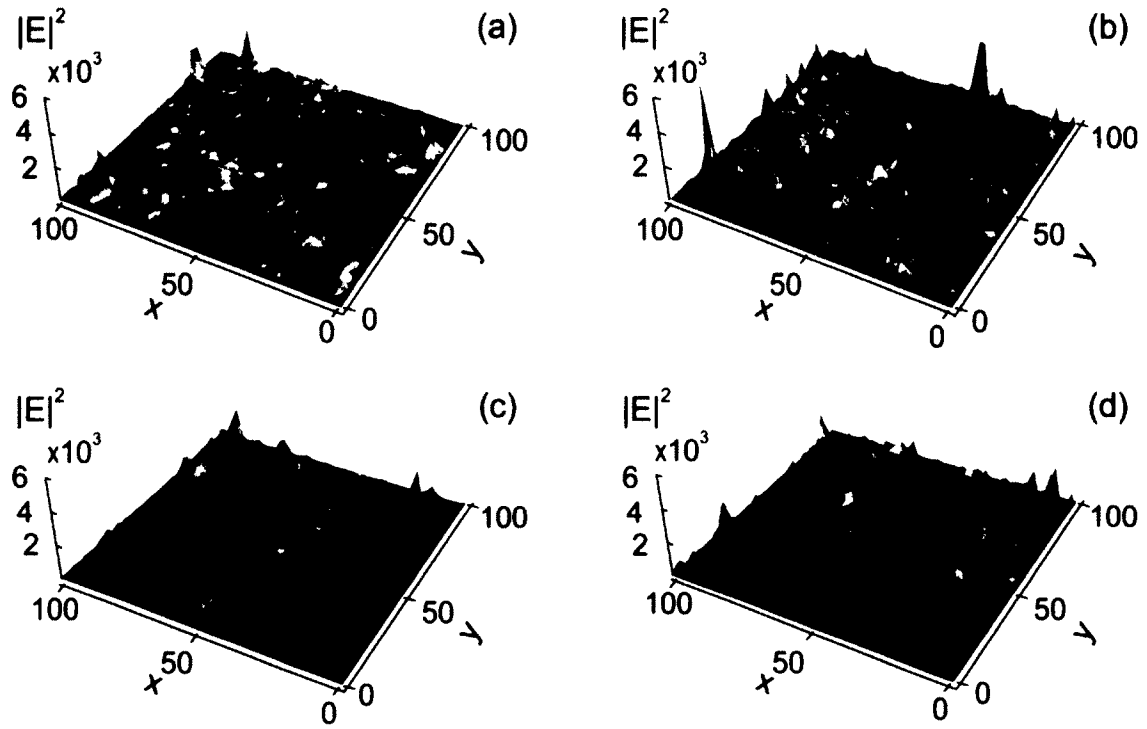

Figure 2-4: The spatial distribution of the local field intensity calculated for a random metal-dielectric composite with size $L = 100$ and metal volume fractions $p = 0.25$. In the calculations we consider two different illumination wavelengths (a), (b) $\lambda = 414nm$ and (c), (d) $\lambda = 800nm$. The local intensity distributions are sampled at two horizontal planes within the composite (a), (c) vertical layer $H = 40$ and (b), (d) and vertical layer $H = 60$. In the calculations we consider a silver with parameters: $\varepsilon_b = 5.0$, $\omega_p = 9.1eV$ and $\omega_\tau = 0.021eV$; for the glass substrate, we used $\varepsilon_d = 2.2$.

2.5 Local Field Distribution Function

An important characteristic of the metal-insulator composites is the fluctuating nature of the local electric fields. This phenomenon can be studied through the local intensity distribution function (LIDF), which is sampled in terms of the local field intensity fluctuations $I = |\vec{E} - \vec{E}_0|^2 / |\vec{E}_0|^2$, where $\vec{E}_0$ is the applied field. The LIDFs for a silver/glass composite were calculated for three different incident wavelengths and are shown in Figure 2-4. We observe exponentially broad intensity distributions whose width

increases with the incident wavelength and intensity enhancements factors that reach exceedingly high values. The LIDFs can be described well with the log-normal function:

$$P(I) = \frac{1}{\sigma I\sqrt{2\pi}} \exp\left[-\frac{(\ln(I) - \langle \ln(I) \rangle)^2}{2\sigma^2}\right], \qquad \textbf{Eq. 2-8}$$

where $\langle \ln(I) \rangle$ is the average logarithmic value of the local field intensity fluctuations, and σ is the standard deviation. The occurrence of exponentially broad intensity distributions is a footprint of the underlying de-localization of surface plasmon modes, as well as the composite's structural morphology. Indeed, if we consider the phenomenological *RLC* model, which predicts the size of the resonating clusters to increase with the wavelength, then it immediately follows that the hot spots will spread out and the local field intensities will span a large range of values. Hence, the LIDF is expected to broaden for higher wavelength which is precisely what is observed in Figure 2-5(a).

The broadening of the distributions and the exceedingly large values of the field enhancement for larger wavelengths can also be understood by considering the following limiting case. The highest local intensity is achieved for a system consisting of a single insulating planar layer sandwiched in an otherwise metallic sample. For such a configuration, the maximum field intensity is located within the insulating layer and considering the continuity of the electric field across the metal-insulator boundary, and the applied incident field $\vec{E}_0$, it is easy to obtain that $\vec{E} = \sigma_m \vec{E}_0/(q\,\sigma_m + (1-q)\,\sigma_d)$, where q is the volume fraction of the insulating planar layer.

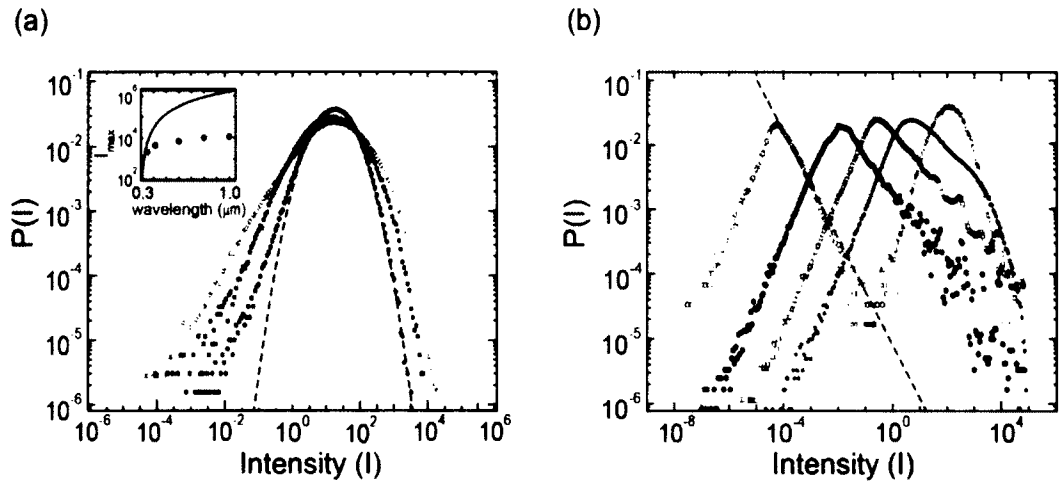

Figure 2-5: Local intensity distribution functions calculated for (a) three different wavelengths at $p = p_c$: • $\lambda = 414nm$, ▪ $\lambda = 800nm$, ○ $\lambda = 1500nm$. Inset: Maximum field intensity calculated at different wavelengths, where the solid represents the maximum limit of local field enhancement calculated from Eq. (10) and dotted line represents the maximum local field intensities obtained from the numerical calculations. (b) at the single particle surface plasmon resonance ($\lambda = 414nm$), for different metal volume fractions: ○ Single Dipole, • $p = 10^{-4}$, □ $p = 10^{-3}$, ✱ $p = 10^{-2}$, [$p = 10^{-1}$. In the calculations the metal is silver with $\varepsilon_b = 5.0$, $\omega_p = 9.1eV$ and $\omega_\tau = 0.021eV$; and the dielectric is glass, $\varepsilon_d = 2.2$. The composite size is set at $L = 60$ and 20 distinct random realizations are used for improved statistics.

For a given incident wavelength the electric field achieved a maximum for a system configuration with layer volume fraction $q = q_c = \sigma_d/(\sigma_d - \sigma_m')$, which gives the limiting maximum value of the fluctuating local field enhancement as:

$$I_{max} = \frac{\left|\vec{E}(q_c) - \vec{E}_0\right|^2}{\left|\vec{E}_0\right|^2} = \left(\frac{\sigma_m'}{\sigma_d}\right)^2 \left(1 + \left(\frac{\sigma_m' - \sigma_d}{\sigma_m''}\right)^2\right). \qquad \textbf{Eq. 2-9}$$

If we consider the Drude model of the metal conductivity, see previous section, it follows that $I_{max} \leq \omega_p^4/(\epsilon_d \omega \omega_\tau)^2$, where $\epsilon_d = i\sigma_d/(\omega\epsilon_0)$, is the relative permittivity of the insulating layer. In the percolating samples, and as the wavelength increases, the maximum value of the local fluctuating field is thus expected to increase. However, the number of hotspots will decreases as evident from the calculated LIDF in Figure 2-5(a).

Our numerical results, see insert in Figure 2-5(a), shows that indeed Eq. (2.9) is an upper bound of the local fluctuating field intensity of the metal-insulating composite.

A change in the local-intensity distribution is also observed for metal volume fractious deviating from the percolation threshold. This effect is shown in Figure 2-5(b) where a set of LIDFs are obtained at the single particle SP resonance wavelength $\lambda = 414nm$. With the decrease in the metal volume fraction, we observe dramatic change from a log-normal into a power-law distribution. This is due to transition from strongly coupled dipole-dipole system at the percolation threshold to a randomly distributed sparse configuration of non-interacting dipoles for small volume fractions. In three-dimensions, a single dipole placed at the center of the co-ordinate system induces an electric field with intensity $I_d(\vec{r}) \propto 1/|\vec{r}|^6$, where $\vec{r}$ is the radial vector from the center of the particle. The expected single-dipole distribution function can be obtained to scale with the filed intensity as $P_D(I) = \int \delta\big(I - I_d(\vec{r})\big)dV \propto I^{-3/2}$, where δ is the Dirac delta function. The analytical result is consistent with the numerically obtained distribution (see Figure2-5(b)) except for very low intensities, where fringe effects due to the cubic geometry of the numerically simulated system violates the central symmetry approximation used in the analytical derivation of $P_D(I)$.

CHAPTER 3

EFFECTIVE PROPERTIES OF RANDOM COMPOSITES

In this chapter, we study the effective (macroscopic) properties of inhomogeneous metal-dielectric composites. Moreover, highly accurate estimates of the effective conductivity and correlation length exponents are obtained and found to be in good agreement with previous estimates using a very different approach based on Monte Carlo simulations. Also, we provide the basis for developing a scaling theory for the higher order-field moments, which are responsible for the nonlinear optical response of the system.

3.1 Effective Conductivity

The local conductivity of inhomogeneous metal-dielectric composites depend on the light frequency and rapidly varies across the system. When the size of the composite is larger than the maximum size of the inhomogeneities, an effective conductivity, σ_e, can be introduced. The effective conductivity can be calculated as a weighted average of the local conductivity with respect to the local energy density [73]:

$$\sigma_e(\omega, p) = \frac{1}{V|\vec{E}_0|^2} \int \sigma(\vec{r}, \omega) |\vec{E}(\vec{r}, \omega, p)|^2 dV, \qquad \textbf{Eq. 3-1}$$

where $\vec{E}$ and $\vec{E}_0$ are the local and applied electric fields, respectively. As the metal volume fraction p increases a geometrical insulator-metal transition takes place in the system. Specifically, the percolation theory predicts that as the metal volume fraction, p approaches the percolation threshold, p_c the effective conductivity for a two-component random mixture will vanish as a power law, i.e. $\sigma_e \sim \sigma_m (p - p_c)^t$ (for $p > p_c$), where t is a critical exponent, which has been calculated previously by many authors and in the 3D case is found to be between $t = 1.6$[71] and $t = 2.36$ [72,73]. This critical behavior is shown in Figure 3-2 where we have estimated the effective conductivity as function of the volume fraction of the high conductivity material. In the calculations, we have set a significant contrast between the "metal" and "insulator" conductivities $\sigma_m/\sigma_d = 10^{13}$ so we may better illustrate the concept. Note, the numerical calculations do not allow simulations of ideal insulators with zero conductivity. As the volume fraction approaches a critical value, i.e. the percolation threshold p_c, the effective conductivity experiences a critical behavior corresponding to a morphology based metal-dielectric phase transition. A possible way of understanding the metal-insulator phase transition is through use of mean field approximations.

3.1.1 Maxwell-Garnett Approximation

The Maxwell-Garnett Approximation (MGA)[2] was the earliest attempt to provide a quantitative description of dielectric mixtures; however, it fails to predict the critical behavior associated with the metal-insulator phase transition, namely the existence of a percolation threshold. According to the theory the effective conductivity is calculated from the relation:

$$\frac{\sigma_d - \sigma_e}{\sigma_d + \eta(\sigma_e - \sigma_d)} + p\frac{\sigma_m - \sigma_d}{\sigma_d + \eta(\sigma_m - \sigma_d)} = 0, \qquad \textbf{Eq. 3-2}$$

where $\sigma_d$is the permittivity of the host-dielectric medium, σ_m permittivity of the metal inclusions and depolarization factor η.

The effective conductivity of the composite can be solved explicitly giving:

$$\sigma_{eff} = \sigma_d + 3p\sigma_d\frac{\sigma_m - \sigma_d}{\sigma_m + (1-\eta)\sigma_d}. \qquad \textbf{Eq. 3-2}$$

The MGT result is not symmetrical with respect to the exchange of σ_d and σ_m. MGT can only be justified for small filling fractions, as shown in Figure 3-1, and it cannot depict or explain the critical behavior of conductivity (Figure 3-2).

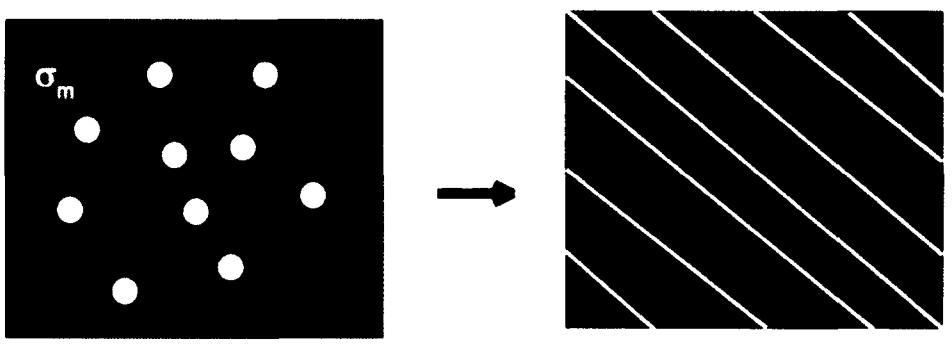

Figure 3-1: Geometry of the composite with metal inclusions of permittivity σ_m embedded in dielectric material σ_d whose effective permittivity is given by $\sigma_{eff}(\sigma_e)$.

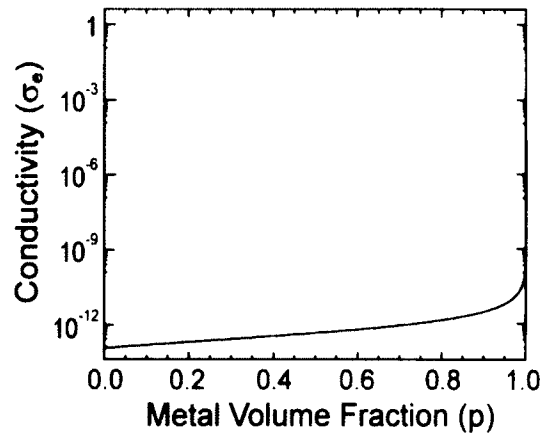

Figure 3-2: Effective conductivity obtained using the Maxwell-Garnett approximation effective medium theory (EMT) with depolarization factor $\eta = 1/3$.

However, the MGT result is rather simple and highly accurate for small factions of inclusions, usually for $p < 0.05$.

3.1.2 Bruggeman's Effective Medium Theory

The Bruggeman's Effective Medium Theory (EMT)[35], treats all constituents on an equal basis and is believed to better describe the binary mixtures at the percolation threshold:

$$p\frac{\sigma_m - \sigma_e}{\sigma_e + \eta(\sigma_m - \sigma_e)} + (1-p)\frac{\sigma_d - \sigma_e}{\sigma_e + \eta(\sigma_d - \sigma_e)} = 0, \qquad \textbf{Eq. 3-4}$$

where $0 \leq \eta \leq 1$ is a depolarization factor, which depends on the shape of the metal inclusions. The effective conductivity can be obtained by simplifying Eq. 3.4 and is given as:

$$\sigma_{eff} = \frac{\eta}{2(1-\eta)}\left\{\frac{1}{\eta}\bar{\sigma} - \sigma_m - \sigma_d \pm \left[\left(\frac{\bar{\sigma}}{\eta} - \sigma_m - \sigma_d\right)^2 + 4\left(\frac{1}{\eta} - 1\right)\sigma_d\sigma_m\right]^{1/2}\right\},$$

where $\bar{\sigma} \equiv p\sigma_m + (1-p)\sigma_d$. Specifically, it is visible that for small concentrations we observe a finite range of frequencies where the real part of the effective conductivity is not negligible. This region corresponds to the frequency band where localized surface plasmons can be excited. At percolation, this frequency band grows and now spans from zero frequency up to the surface plasmon frequency $\omega_{sp} = \omega_p/\sqrt{\epsilon_b + 2\epsilon_d}$. At concentration higher than percolation, we gradually recover the bulk conductivity of silver (Figure 3-3).

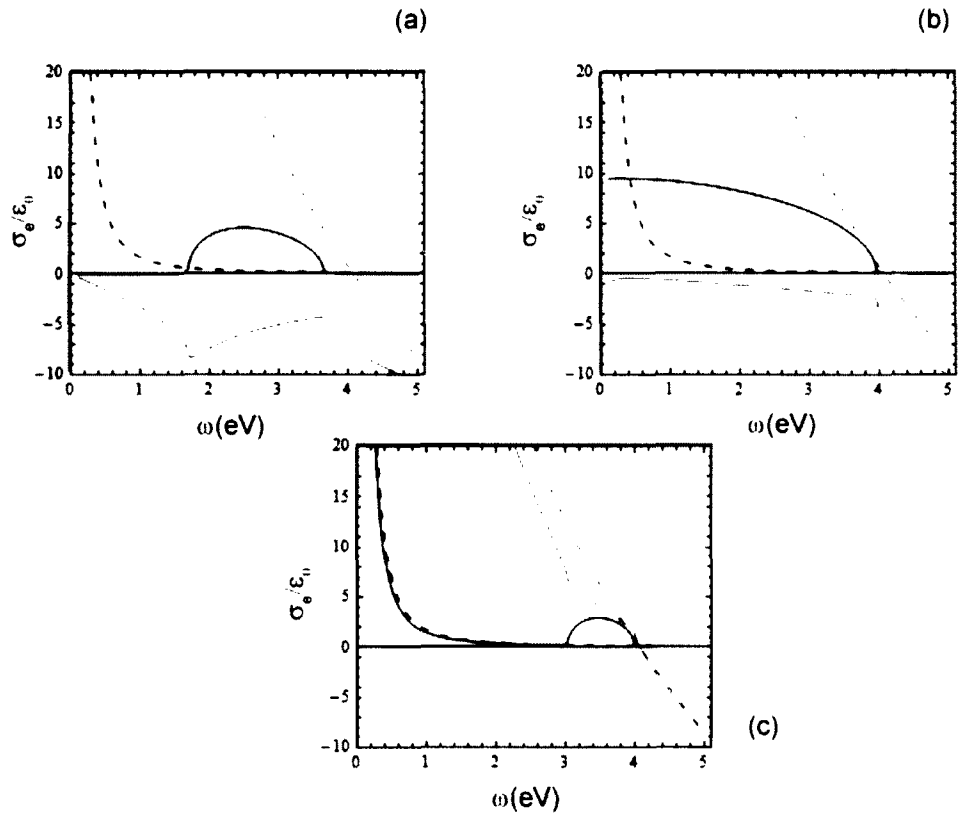

Figure 3-3: Effective conductivity of silver-glass composite for (a) $p = 0.1$, (b) at percolation $p = 1/3$ and (c) for $p = 0.9$. The solid blue and red lines corespond to the real and imaginary parts of the conductivity, respectively. For comparison, we have also included the conductivity (with dashed lines) of bulk silver.

The Bruggeman's EMT predicts a metal-insulator phase transition at a critical volume fraction (percolation threshold) equal to the depolarization factor $p_c^{EMT} = \eta$. This is easy to observe if in Eq. 3.3 we consider the limit $\sigma_d \to 0$ with the effective conductivity converging to:

$$\sigma_e = \sigma_m \left(\frac{p - p_c^{EMT}}{1 - p_c^{EMT}} \right) \theta(p - p_c^{EMT}), \qquad \textbf{Eq. 3-5}$$

where θ is the step function. This limiting case shows that according to the EMT the transition is described with a critical exponent $t = 1$ regardless of the dimensionality of the problem, which contradicts observations [72, 73]. Furthermore, in the 3D case and assuming spherical inclusions, the EMT predicts a percolation threshold $p_c^{EMT} = \eta = 1/3$. This is substantially higher compared to the critical volume fraction for common percolation models, such as bond percolation with $p_c \approx 0.2488$ [74] and site percolation with $p_c \approx 0.3116$ [75]. This discrepancy is not surprising since it is well known that the percolation threshold is not a universal parameter but depends on the composite formation physics and the nature of the constituents. One may attempt to modify the EMT result by adjusting the depolarization factor to match the proper threshold for a given percolation model, i.e. $\eta = p_c$. This may provide for a somehow similar behavior (the adjusted EMT is also included in Figure 3-4 with dashed line); however it will violate the proper behavior for small metal volume fractions and still will not give the correct critical exponent for the effective conductivity in close proximity to the percolation threshold.

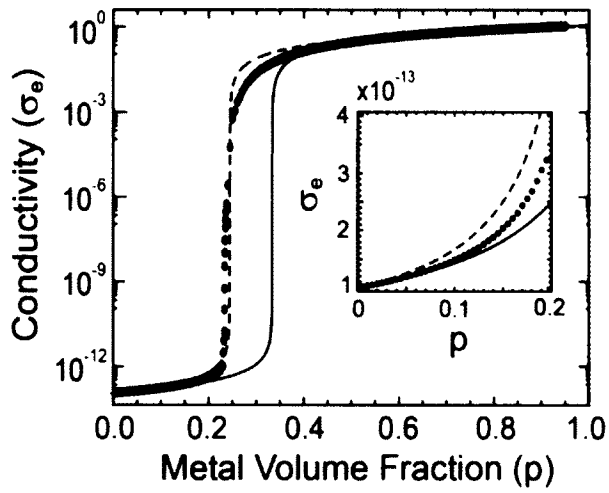

Figure 3-4: Effective conductivity σ_e of a three-dimensional (3D) composite with size $L = 40$ as function of the volume fraction p for the high conductivity constituent. Inset: a close inspection of the effective conductivity obtained at lower metal volume fractions.

In the calculations we set the "metal" and "insulator" conductivities at $\sigma_m = 1$ and $\sigma_d = 10^{-13}$, respectively, and average the system conductivity over 60 distinct random realizations.

3.2 Critical Exponents

To better understand the metal-insulator phase transition, and, specifically, the critical behavior at the percolation threshold, one instead relies on the finite-size scaling theory [71, 76]. According to the theory, as the metal volume fraction approaches the percolation threshold, the correlation length, or the size of the largest metal cluster in the composite, diverges as $\xi \sim (p - p_c)^{-\nu}$ [77], where v is a critical exponent. Correspondingly, continuous metal paths form within the system, facilitating the conduction of electrical current. For small systems with sizes $L \ll \xi$, the effective conductivity depends on L and scales as a power law, $\sigma_e(L) \sim AL^{-t/\nu}$[63]. For $L \gg \xi$, the system is homogeneous and the conductivity is independent on system size. Based on

these two limiting cases, the finite-size scaling theory predicts a general dependence for the effective conductivity given as [79]:

$$\sigma_e(L) \sim L^{-t/\nu} f\left(L^{1/\nu}(p - p_c)\right), \qquad \textbf{Eq. 3-6}$$

where f is a universal function independent on the percolation model and satisfying the condition $f(0) \neq 0$.

A common approach toward determining the scaling exponents, and, in particular, the ratio t/ν, is to calculate the effective conductivity of the composite at the percolation threshold. However, this approach requires a good estimate for p_c. The current best estimate of the bond percolation threshold in 3D has been obtained by Lorenz and Ziff using Monte Carlo simulations, $p_c = 0.2488126 \pm 0.0000005$ [74]. Based on this value, and using the BE method, we have obtained the effective conductivity as function of the system size L. Our results are shown in Figure 3-5(a). In order to improve the statistics for each size L, we have performed a large number of distinct random realizations of the composites. For statistical consistency we have set the number of realizations for each system size such that we maintain a constant total volume used in the averaging process outlined by Eq. (3.1). Applying a standard χ^2 analysis of the numerical data, we have obtained an estimate for the ratio of the critical exponents $t/\nu = 2.28 \pm 0.04$. This result is in a good agreement with previous estimates, $t/\nu = 2.2 \pm 0.1$ of Derrida, *et. al.* [78], $t/\nu = 2.26 \pm 0.04$ of Normand and Herrmann [79], $t/\nu = 2.276 \pm 0.012$ of Gingold and Lobb [80], and $t/\nu = 2.305 \pm 0.15$ of Clerc et al. [81]. Using the correlation length critical exponent $\nu = 0.88 \pm 0.01$ [73, 81], we can also indirectly deduce the conductivity critical exponent as $t = 2.02 \pm 0.05$.

The obtained estimates for the scaling exponent ratio t/ν allows us to directly map the universal scaling function Eq. (3.6). A set of calculations have been performed for various system sizes and metal volume fractions in proximity to p_c. The obtained effective conductivities are then collapsed on a single universal curve by multiplying with the size dependent factor $L^{-t/\nu}$ and plotting with respect to the compound parameter $x = \Delta p_c L^{1/\nu}$. The results are shown in Figure 3-5(b). The universal function follows power law behaviors close to the percolation threshold as:

$$f(x) = f(0) + \begin{cases} Ax^{t}, & p > p_c \\ Bx^{-s}, & p < p_c \end{cases}, \qquad \textbf{Eq. 3-7}$$

with two independent critical exponents t and s. A χ^2analysis have been performed to fit the data (see insert in Figure 3-5(b)) and estimate the critical exponents $t = 2.01 \pm 0.03$, $s = 0.76 \pm 0.02$ along with coefficients $A = 10 \pm 0.05$, $B = 1.1 \pm 0.04$. To the best of our knowledge, this is the first time that both exponents are independently obtained directly based on energy considerations (see Eq. 3.1).

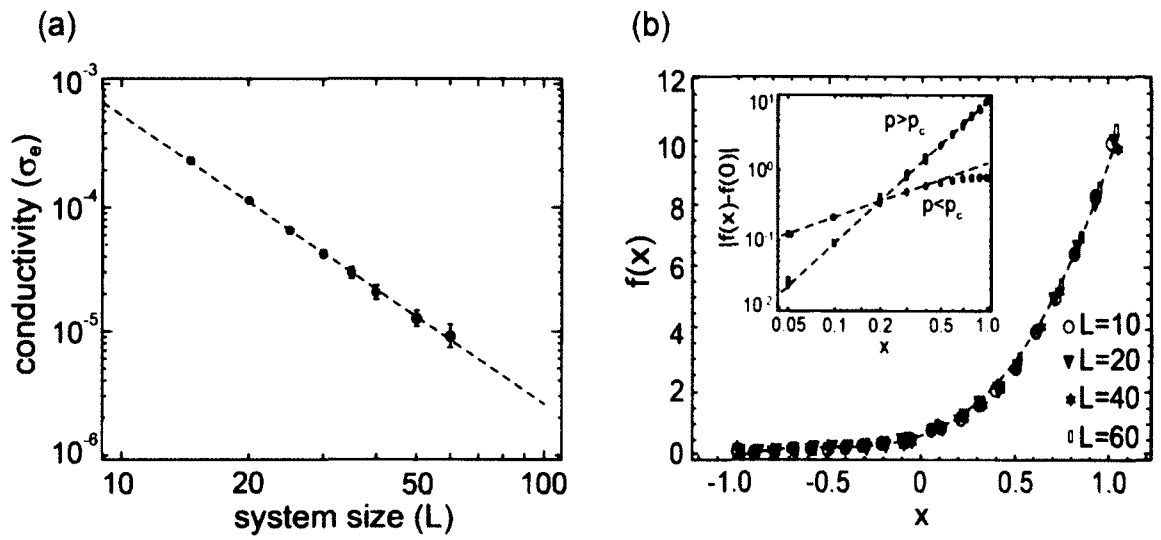

Figure 3-5: (a) Effective conductivity of three-dimensional (3D) random metal-insulator composite at the percolation threshold $p = p_c = 0.2488126$ and as a function of the system size L. (b) The effective conductivity of composites with different sizes is collapsed onto a single universal function f, (see. Eq. (3.7)), when calculated vs. the compound parameter $x = \Delta p_c L^{1/\nu} = (p - p_c)L^{1/\nu}$. In the insert, the power law behavior of the universal function in close proximity to the percolation threshold is examined.

In the above calculations, the number of realizations for each system size $n_r(L)$ is chosen such that the total system volume that in being averaged over is maintained constant $n_r(L)L^3 = 5 \times 10^6$, enforcing the statistical condition that each data point is to be estimated with the same number of distinct fluctuating field terms used in the averaging process outlined by Eq. (3.1). A sufficient contrast between the "metal" and "insulator" conductivities $\sigma_m/\sigma_d = 10^{13}$ is chosen in order to map the entire range of effective conductivities for all system sizes under consideration.

3.3 Higher Order Field Moments-Scaling Exponents

Giant enhancement of optical responses in a random medium including a metal component, such as metal nanocomposites and metal rough thin films consisting of small nanometer-sized particles or roughness features, is associated with optical excitation of surface plasmons that are collective electromagnetic modes and strongly depend on the geometrical structure of the medium. Nanocomposites and rough thin films are, typically, characterized by fractal geometry, where collective optical excitations, such as surface plasmons, tend to be localized in small nm-sized areas, namely hot spots [45]. Thus, in fractals collective plasmon oscillations are strongly affected by the fractal morphology, leading to the existence of hot and cold spots (i.e. areas of high and low local fields). Local enhancements in the hot spots can exceed the average surface enhancement by many orders of magnitude because the local electric peaks are spatially separated by distances much larger than the peak sizes. The spatial distribution of these high-field regions is very sensitive to the frequency and polarization of the applied field [82-92]. The positions of the hot spots change chaotically with change in the frequency and/or polarization. This is similar to speckle patterns created by laser light scattered from a rough surface, with the important difference being that the scale-size for the fractal clusters facilitated surface plasmons hot spots are in the nanometer range rather than in the micrometer range encountered for photons.

Because of the random character of fractal surfaces, the high local fields associated with the hot spots entail strong spatial field fluctuations. Since a nonlinear optical process is proportional to the local fields raised to a power greater than one, the resulting enhancement associated with the fluctuation fields (i.e. with the hot spot) can be

extremely large. In a sense, we can say that enhancement of optical nonlinearities is especially large in fractals because of very strong field fluctuations. Large fluctuations of local electromagnetic fields on a metal surface of inhomogeneous metal media result in a number of enhanced optical effects. A well-known effect is the surface-enhanced Raman scattering (SERS) by molecules adsorbed on a rough metal surface, e.g. in aggregated colloid particles [93-95].

Since local filed fluctuations in random media are crucial in forming the nonlinear response, mean-field approaches to study these effects are not applicable. As we have already shown above, the local field fluctuations are especially pronounced in the optical and infrared spectral ranges for a composite material containing metal particles with negative real and small imaginary parts of the dielectric constant. These phenomenons have been also reported by a number of experimental and theoretical studies [82, 51, 96-98]. Possible applications include bio-sensing, nonlinear optical switches, filters, and bistable elements.

To quantify the nonlinear response of the inhomogeneous composites, one uses the ensemble/volume averaged moments of the local fields [52]:

$$M_{n,m} = \frac{1}{V}\int \frac{\left|\vec{E}(\vec{r})\right|^{n}\left[\vec{E}(\vec{r})\cdot\vec{E}(\vec{r})\right]^{m/2}}{\left|\vec{E}_0\right|^{n}\left[\vec{E}_0\cdot\vec{E}_0\right]^{m/2}}dV. \qquad \textbf{Eq. 3-8}$$

The field moment [52], $M_{2k,m}$ represents a nonlinear process in which k photons are annihilated and $k+m$ photons are added to the continuum [99, 100]. For instance, the enhancement of Kerr optical nonlinearity is proportional to $M_{2,2}$, the surface enhanced Raman scattering (SERS) is represented by $M_{4,0}$, and third harmonic generation enhancement is given by $\left|M_{0,3}\right|^2$.

In the case of non-interactive metal particles immersed in a dielectric medium, the surface plasmon resonance occurs when $\sigma_m = -2\sigma_d$, and it can be investigated using a dimensionless set of complex value conductivities $\sigma_d = -i$ and $\sigma_m = 2i + \kappa$, where κ is a small real conductivity that corresponds to the losses in the metal consituents. In this particular case, Kirchoff's Hamiltonian (see Eq [2.3]) can be written as $\hat{H} = \hat{H}' + i\kappa\hat{H}''$, where the $i\kappa\hat{H}''(\kappa \ll 1)$ represents the losses in the system. It must be noted that $\hat{H}'$ has a form similar to the tight-binding Hamiltonians encountered in the studies of charge transport in disordered atomic systems. This is the well-known Anderson localization problem in quantum mechanics. The distinction is that in the case of surface Plasmons, the Kirchhoff's matric has correlated diagonal and off diagonal disorder. The correlations are due to the local current conservation, which results in dramatic changes in the nature of the SP localization when compared to the discrete non-correlated Anderson analog, i.e. the localization-delocalization transition for the electromagnetic response of the composite material.

In 2000, Sarychev and Shalaev [28], starting from the single particle resonance case and relying on the Anderson analogy in quantum mechanics, developed a scaling theory for the local field moments in percolating metal-insulator composites. In their approach, the local potential $\varphi(\vec{r})$ is expanded over the SP eignestates Ψ_n of $\hat{H}'$; then the problem of finding the local field distribution in the system is reduced to the solution of the surface plasmon eigenproblem through the Kirchoff Hamitonian, $\hat{H}'\Psi_n = a^2\lambda_n\Psi_n = \Lambda_n\Psi_n$, where a is the size of the metal particles and Λ_n are the non-dimensional eigenvalues. The term proportional to the losses $i\kappa\hat{H}''$can be treated as a perturbation. By expanding the fluctuating potential over the eigenstates of the

unperturbed Kirchhoff's Hamiltonian $\varphi = \sum_n A_n \Psi_n$, it is straightforward to obtain a liner system of equations for the expansion coefficients:

$$(\Lambda_n + i\kappa H_{n,n})A_n + i\kappa \sum_{m \neq n} H_{n,m} A_m = \mathcal{E}_n, \qquad \textbf{Eq. 3-9}$$

where $H_{n,m} = (\Psi_n | H'' | \Psi_m)$, and $\mathcal{E}_n = (\Psi_n | \mathcal{E})$ is the projection of the external field on the eigenstate Ψ_n. In the zero order of the approximation we can obtain the expansion coefficients as $A_n^{(0)} = \mathcal{E}_n / (\Lambda_n + i\kappa H_{n,n})$. The fluctuating part of the local field is then given by:

$$\vec{E}_f(\vec{r}) = -\vec{\nabla}\varphi(\vec{r}) = -\sum\nolimits_n \frac{\mathcal{E}_n}{\Lambda_n + i\kappa H_{n,n}} \vec{\nabla}\Psi_n(\vec{r}). \qquad \textbf{Eq. 3-10}$$

The spatially averaged local field intensity over the entire system then follows as:

$$\begin{aligned} \langle |\vec{E}(\vec{r})|^2 \rangle &= \langle |\vec{E}_f + \vec{E}_0|^2 \rangle = \langle |\vec{E}_f|^2 \rangle + 2\vec{E}_0 \cdot \langle \vec{E}_f \rangle + \langle |\vec{E}_f|^2 \rangle \\ &= |\vec{E}_0|^2 + \sum_{n,m} \frac{\mathcal{E}_n \mathcal{E}_m^* \langle \vec{\nabla}\Psi_n(\vec{r}) \cdot \vec{\nabla}\Psi_m^*(\vec{r}) \rangle}{(\Lambda_n + i\kappa H_{n,n})(\Lambda_m - i\kappa H_{m,m})}, \end{aligned} \qquad \textbf{Eq. 3-11}$$

where we have used that fluctuation condition $\langle \vec{E}_f \rangle = 0$ and V is the system volume. Introducing the surface plasmon density of states (DOS) $\rho(\Lambda) = \sum_n \delta(\Lambda - \Lambda_n)$, we can transform the summation into integration:

$$\begin{aligned} &\langle |\vec{E}|^2 \rangle \\ &= |\vec{E}_0|^2 + \iint \frac{\rho(\Lambda)\rho(\Lambda')\mathcal{E}(\Lambda)\mathcal{E}^*(\Lambda')\langle \vec{\nabla}\Psi(\vec{r},\Lambda) \cdot \vec{\nabla}\Psi^*(\vec{r},\Lambda') \rangle d\Lambda d\Lambda'}{(\Lambda + i\kappa H(\Lambda))(\Lambda' - i\kappa H(\Lambda'))}, \end{aligned} \qquad \textbf{Eq. 3-12}$$

where a is the size of the metal particle, d is the dimensionality. The eigenfunctions are transformed according to $\Psi_n(\vec{r}) \to \Psi(\vec{r},\Lambda)$ and $\Psi_m(\vec{r}) \to \Psi(\vec{r},\Lambda')$, while the matric

elements are $H_{n,n} \to H(\Lambda)$ and and $H_{m,m} \to H(\Lambda')$. Similarly, the projection operators on the external electric fields are $\mathcal{E}_n \to \mathcal{E}(\Lambda)$ and $\mathcal{E}_m \to \mathcal{E}(\Lambda')$. If the SPP eigenstates are localized with localization length $\xi(\Lambda)$, we can also estimate $\langle \vec{\nabla}\Psi(\vec{r},\Lambda) \cdot \vec{\nabla}\Psi^*(\vec{r},\Lambda')\rangle \approx a^2\,\delta(\Lambda-\Lambda')/\xi^2(\Lambda)$ and $\mathcal{E}(\Lambda) \approx E_0(\xi(\Lambda)/a)^{d/2-1}$. This allows us to write the expectation value of the system averaged local field intensity enhancement as:

$$\frac{\langle|\vec{E}(\vec{r})|^2\rangle}{|\vec{E}_0|^2} = 1 + \int \frac{\rho(\Lambda)\left(\xi_f(\Lambda)/a\right)^{d-4}}{\kappa^2+\Lambda^2}\,d\Lambda, \qquad \textbf{Eq. 3-13}$$

where we use that $H(\Lambda)$ is of the order of unity. Analogously we can also obtain a general result for the expectation values of the higher order field moments as:

$$M_n = \frac{\langle|\vec{E}(\vec{r})|^n\rangle}{|\vec{E}_0|^n} = 1 + \int \frac{\rho(\Lambda)\left(\xi_f(\Lambda)/a\right)^{d-2n}}{(\kappa^2+\Lambda^2)^{n/2}}\,d\Lambda. \qquad \textbf{Eq. 3-14}$$

If the surface plasmon states are strongly localized (Anderson localization) with $\xi_f(\Lambda)/a \approx 1$, with non-singular density of states $\rho(\Lambda)$, it is easy to perform the integration leading to power law dependence of the field moments with respect to the dissipation parameter $M_n \sim \kappa^{-\chi_n}$, with an exponent $\chi_n = n-1$. This is the original result obtained by Sarychev and Shalaev [52], which, as just argued, was based on the assumption of a strong, Anderson type of localization for the surface plasmon modes. However, in 20001 Stockman *et al.* argued that the SPs are predominantly delocalized and it is the delocalized modes that play the main role in the interactions with the external illumination [80]. Finally, Genov *et al.* have demonstrated that the role of these delocalized modes is more subtle as it dramatically depends on the size of the system [102]. Specifically, the measure of the delocalized states in the spectra (the ratio between

the numbers of delocalized states to the total number of states) has been shown to exponentially decrease with the system size in two-dimensional composites. However, despite the zero measure, the delocalized states still affect the optical properties of the composite by modifying the critical indices.

Here, we expand the modified scaling theory for the local field moments [102] for three-dimensional composites. Specifically, assuming a power-law delocalization for both SPs density of states $\rho(\Lambda)\sim|\Lambda|^{-\gamma}$ and localization length $\xi_f(\Lambda)\sim|\Lambda|^{-\alpha}$ we obtain the higher-order field moments:

$$M_n \sim \kappa^{-\chi_n}, \qquad \textbf{Eq. 3-15}$$

where $\chi_n = (n-1)(1-2\alpha)+\gamma+\alpha(d-2)$ is a positive scaling exponent that dependends on the dimensionality d of the composite and delocalization exponents γ, α, for strong localization and absence of singularities in the SP density of state and localization length ($\gamma = \alpha = 0$). However, the field moments have been validated in the 2D case earlier [81], using the BE methods, and by directly solving the inherent eigenproblem giving the finite delocalization exponents $\alpha \approx \gamma = 0.14$. Here, we study the field moment in the 3D case. In the numerical calculations, we consider percolating ($p = p_c$) metal-insulator composites by varying the dissipation factor in the range $\kappa \in 10^{-1} - 10^{-3}$. Our results are shown in Figure 3-6(a). In accordance to the scaling theory Eq. (3.15), the higher order field moments are found to follow a power law dependence on the dissipation parameter κ. For each field moment, M_n a χ^2 analysis have been performed to fit the data and obtain an estimate of the field exponent χ_n. Finally the obtained exponents, shown in Figure 3-6(b), are used to estimate the SP delocalization exponents, giving $\alpha = 0.18 \pm 0.02$ and $\gamma = 0.08 \pm 0.02$. This is the first time that these

critical exponents have been estimated. It also must be noted that in the 3D case, and within the statistical error, the exponent for the localization length is given as $\alpha = 1/2 - \nu/(t+s)$, where t, s, ν are the critical exponents of the static conductivity, dielectric constant (permittivity), and percolation correlation length.

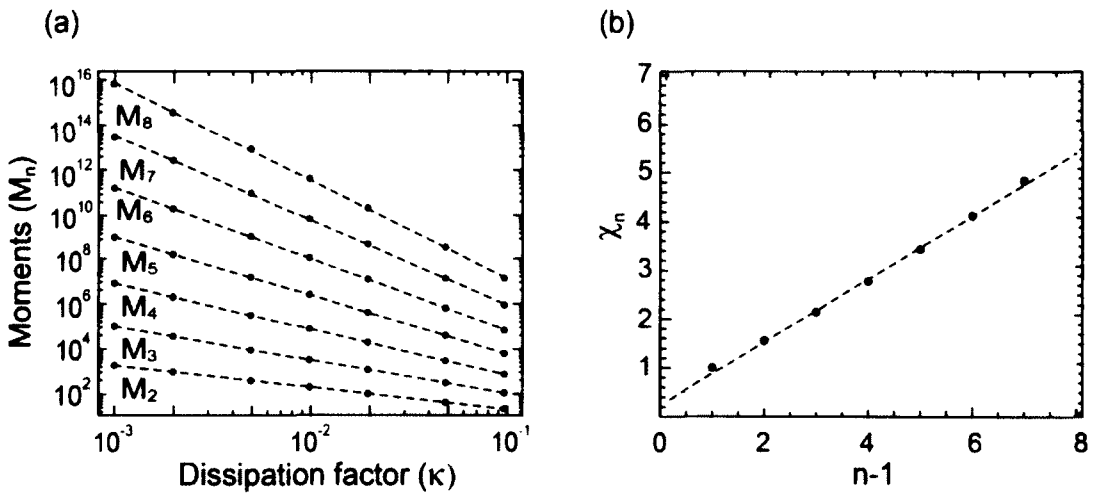

Figure 3-6:(a) The electric high order field moments M_n as function of the dissipation factor κ.(b) The expected field moments exponents are numerically estimated and fitted to the theoretical result $\chi_n = (n-1)(1-2\alpha) + \gamma + \alpha$, giving an estimate for the SP density of states and localization length exponents α and γ, respectively. In all calculations the lattice size was fixed at $L = 60$ and 20 realizations of the random geometry were used to improved statistics.

Using Eq. (3.15) we can also extend the theory to describe the field moments for frequencies spanning the optical and near-infrared spectral range. This is accomplished through renormalization of the system by dividing it in cubes with size $l_r = a(|\varepsilon_m|/\varepsilon_d)^{\nu/(t+s)}$, and renormalizing the electric field $E_m \sim (l_r/a)E_m^*$ and hot spots separation length as $\xi \sim \xi_e^*(l_r/a)$ [52,102]. The field moments then follows as:

$$M_n \approx \left(\frac{|\varepsilon_m'|}{\varepsilon_m''}\right)^{\chi_n} \left(\frac{|\varepsilon_m'|}{\varepsilon_d}\right)^{\mu_n}, \qquad \textbf{Eq. 3-16}$$

where $\mu_n = (s + \nu(n-2))/(t+s)$ and the scaling relationship $n(l_r) \propto (l_r/a)^s$ for the number of peaks in each segment has been used.

The higher order local-field moments at frequencies above the single particle resonance, as predicted by Eq. (3.16), and estimated using the block elimination method, are compared in Figure 3-7. Clearly there is an excellent correlation between numerical simulations and theoretical results. In both cases the field moments initially increase with the incident wavelength, reaching a maximum value and then gradually decreasing as a power law. For intermediate frequencies $\tilde{\omega}_p > \omega \gg \omega_\tau$, the optimal frequency can be obtained from Eq. (3.17)

$$\omega_n = \tilde{\omega}_p \sqrt{\frac{\chi_n - 2\mu_n}{3\chi_n}}, \qquad \textbf{Eq. 3-17}$$

and accordingly, the maximum field moments can be estimated as we obtain that for the

$$M_{n,max} = M_n(\omega_n) \approx \left(\frac{2\varepsilon_b}{\varepsilon_d}\right)^{\mu_n} \left(\frac{\tilde{\omega}_p}{\omega_\tau}\right)^{\chi_n} \frac{\left(1+\frac{\mu_n}{\chi_n}\right)^{\mu_n+\chi_n}}{\left(1-\frac{2\mu_n}{\chi_n}\right)^{\mu_n-\frac{\chi_n}{2}}} \approx \left(\frac{\tilde{\omega}_p}{\omega_\tau}\right)^{\chi_n}. \qquad \textbf{Eq. 3-18}$$

For instance, the cross-section for Raman scattering is expected to scale as $\sim M_{4,max} = 10^5$ in 3D random nanocomposites, which is lower than what is expected in periodic closely packed metal arrays [103].

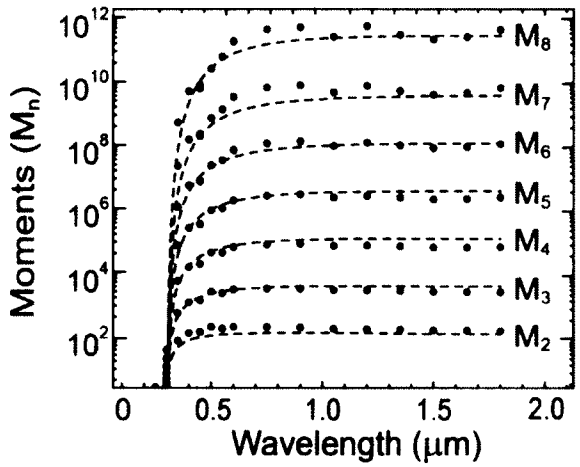

Figure 3-7: The local-field moments $M_{n,0}$ (dots) are calculated with the exact numerical method (BE) and compared to the analytical results with exponents $\alpha = 0.18 \pm 0.02$ and $\gamma = 0.08 \pm 0.02$ (lines).We used $t = 2.02$, $s = 0.76$ and $\nu = 0.88$ from this work and previous estimates [63][77]. In the calculations, we used lattice size of $L = 60$ and have averaged the field moments over 20 realizations.

CHAPTER 4

SEMI-CONTINUOUS METAL-DIELECTRIC COMPOSITES IN THIN FILM SOLAR CELLS

In this chapter we propose and study an efficient solution to a persistent problem preventing the mass adoption of thin film solar cells for commercial use, namely the low power conversion efficiency. A primary factor in the low efficiency is the insufficient light absorption by the very thin active material. Through analytical modeling, we present here a method to enhance the absorption and efficiency of organic/inorganic semiconductor thin film solar cells through the integration of a thin inhomogeneous metal-dielectric composite (MDC) electrode at the interface between a transparent electrode and the active photovoltaic (PV) layer. Through numerical simulations, we show that surface plasmons become excited within the fractal MDC across an extremely broad range of optical frequencies, trapping incoming light and ensuring the optimal absorption of light in the solar cell. An analytical model is also developed to estimate the current-voltage (IV) –characteristics of the device. The model provides the geometrical charcateristics of the cell optimizing power convergence efficiency. These results can be used to guide the design of a prototype.

4.1 Introduction

While the world's energy needs are growing, the current primary sources of energy, such as those based on fossil fuel, are depleting and have detrimental effects on the

environment [104]. These competing trends demand the utilization of novel sources of energy such as solar, wind, etc. Optoelectronic devices, such as solar cells and photodetectors, are the main sources to harness solar energy. The two major methods for conversion of sun light into electrical current are based on photovoltaic and photo-emissive processes. Photovoltaic devices can use a *p-n* junction to directly transfer the photon energy into current and can operate at low quantum efficiencies [105-108]. Many commercially available solar cells contain either toxic elements (arsenic, cadmium) or very rare metals, such as platinum. Manufacturing of inorganic solar cells requires fabrication processes with high temperatures; thus, the energy consumption for the fabrication for these cells is high. Polymer-based solar cells are promising, but their comparatively low efficiency and stability are a drawback.

Up to 80% of the cost for the current generation of inorganic solar cells is due to the active substrate (a semiconductor material) production cost. In an attempt to lower costs, manufacturers have significantly reduced the amount of active layer through the use of thin films (less than 1 microns in thickness) or through the use of inexpensive organic active materials. However, such reduction in active layer thickness typically results in decreased efficiency. Accordingly, there is a continuing need to develop a thin film solar cell technology that provides increased efficiency while reducing the amount of the photovoltaic material utilized.

In general, either organic (polymer) or inorganic (Si) materials are used as active layers in solar cells. However, silicon is dominantly used in solar cell because of its high efficiency, non-toxicity, abundance in nature, long-term stability, and well established

technology [108, 109]. Despite being a relatively well developed technology, the power conversion efficiency of silicon solar cell is still below 25% [110].

Overall there are two main directions toward achieving high solar cells efficiency: (*i*) increase of the photon density of states (DOS) within the active medium and use of broadband, high intrinsic absorption materials, and (*ii*) increase the optimal thickness of the active layer. The active layer of a solar cell must be thick enough to ensure sufficient absorption of incident photons, but it also must be thin in order to ensure efficient charge extraction. To obtain the optimal thickness of the active layer, at which maximum light absorption and maximum charge extraction occurs, it is important to understand the behavior of charge carriers under different wavelengths and spatial conditions.

In this work we present an effective approach to enhance light absorption, photocurrent generation, and therefore the quantum efficiency of organic and inorganic semiconductor photovoltaic/photodetector devices. We have integrated a thin, inhomogeneous metal-dielectric composite (MDC) (<20nm) sputtered below, or at the percolation threshold, between the active layer and the indium-tin-oxide (ITO) electrode, which improves light absorption in the active layer through the surface plasmon phenomenon. In section 4.2, we discuss the coupling of the electromagnetic response of the MDC with the active layer, and investigate the optical characteristics of the solar cell for different geometrical configuration by varying both the thickness of the active layer and metal concentration in MDC. We observed a substantial improvement in absorption when compared with the bare (without the MDC layer) organic/inorganic semiconductor solar cells. In section 4.3, we implement an analytical IV model for the charge carriers and current flow through the device, Ashish *et.al.*[111]. By implementing a constant generation

rate (valid for thin cells) we obtained the optimal quantum efficiency of the organic/inorganic solar cells as a function of the active layer thickness and metal concentration of MDC.

4.2 Modeling

The inhomogeneous metal-dielectric composites are plasmonic nano-materials that have unique geometrical and optical properties, which are not inherent to the constituent metal/dielectric substrates, but result from complex electromagnetic many-body interactions. Under electromagnetic illumination, they exhibit energy localization and huge enhancement of the local field intensities, which corresponds to the excitation of localized surface plasmon (SP) modes, with intrinsic density of states (DOS) far surpassing that of the incident light [56, 66, 102]. At critical metal concentrations (p_c), the random films are inhomogeneous in nature and are composed of fractal nanostructures on all length-scales. Thus for any incident wavelength, resonating clusters exist in the composite, providing a broad frequency response and anomalous optical properties including extraordinary absorption, which is observed both theoretically and experimentally [112-114].

Metal nano-particles have recently been proposed to enhance the optical absorption in thin-film solar cells [115]. In 2007 Pillai *et. al.*, demonstrated enhanced photoluminescence for crystalline silicon solar cells in the near-infrared spectral range [116]. Periodic array of Ag strips on a silica-coated Si film have been proposed to provide strong coupling between the SP modes and active super-layer [117]. Various PV efficiency enhancement techniques based on light trapping and surface plasmon resonance has been also developed for thin film solar cell [118-119]. However, the spectral range of operation of these devices was rather narrow (~100nm) subsequently, not allowing efficient

utilization of the solar spectra. Nanophotonic techniques [120-121] are very effective for the light trapping since they provide flexibility to control the flow of light on the scale of several 100 nm to a few micrometers, which is best suited for thin film solar cells [122]. Despite the progress, the transformative effect of the exceedingly large SP DOS on the solar cell performance has not been fully utilized. This is due to a lack of understanding for the fundamental processes facilitating the SP excitation and localization in the metal-dielectric composites in the 3D case and the evanescent coupling between the SP and the active media. In this work, we implement the Block elimination (BE) method developed in this thesis work, which allows for the calculation of the local electromagnetic response of the 3D metal-dielectric composites, and which serves as an enhancement layer for the solar cell. In the process, we have incorporated the knowledge gained of the electromagnetic field interactions with highly inhomogeneous media, three dimensional (3D) metal-dielectric composites, and designed this new type of solar cell, which we refer to as Surface Plasmon Enhanced Solar Cell (SPESC).

Here, we model SPESCs using both organic (polymer) and inorganic semiconducting active layers. One embodiment provides a solar cell composition, comprising a Glass/ITO/SPb/MDC/Al or Glass/ITO/MDC/SPb/Al multilayer stack encompassing a glass substrate, transparent electrode (ITO), a semiconductor polymer blend (SPb), such as a poly(3-hexylthiophene-2,5-diyl):1-(3-methoxycarbonyl) propyl-1-phenyl [6,6]-methanofullerene (P3HT:PCBM), metal composite electrode (MDC), and transition or post-transition metal contact, such as Aluminum (Al). The MDC electrode is in direct contact with the active layer and having a metal concentration that can vary from 10-60% but is predominantly below percolation.

Another embodiment provides a photovoltaic cell composition, comprising a SiO_2(Al)/MDC/IS/ZnO/Al multilayer stacks encompassing a glass substrate (SiO_2 -- transparent contact electrode), an inorganic semiconductor (IS), such as single crystal silicon *c*-Si or hydrogenated amorphous silicon *a*-Si:H, a metal-dielectric composite electrode (MDC)--zinc oxide (ZnO) will act as a buffer layer and help to effectively collect charge carriers and a second transition or post-transition metal contact, such as Aluminum (Al). The MDC electrode is in direct contact with the active layer and has a metal concentration that can vary from 10-60%, but is predominantly below percolation.

The described thin film solar cell configurations are depicted in Figure 4-1. The devices consist of six functional layers: transparent glass substrate, transparent anode (T-electrode, ITO), MDC electrode, optically active organic/inorganic semiconductor layer, Zinc Oxide (ZnO), and reflecting layer (R-electrode (cathode), Aluminum). The incident light approaches from the transparent substrate i.e. the ITO side. The active media is the organic semiconducting material (P3HT:PCBM) or inorganic semiconducting material (single crystal silicon *c*-Si or hydrogenated amorphous silicon *a*-Si:H). A thin (< 20 nm) MDC electrode layer is considered as a part of either cathode or anode electrode for additional efficiency enhancement.

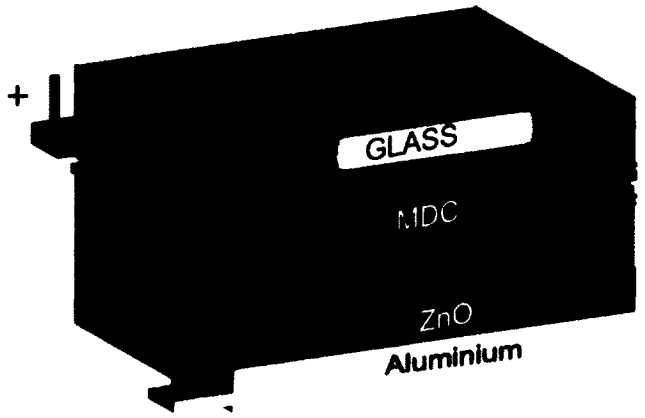

Figure 4-1: Basic layout of plasmonically enhanced photovoltaic device. Illumination is through a transparent electrode (ITO) with MDC on top of active layer.

In the implementation of the MDC layer, we considered silver being the metal constituent and the dielectric is either a P3HT:PCBM for organic solar cell geometry or *c*-Si or *a*-Si:H for the inorganic devices. The light reaching the MDC electrode excites SP resonances that trap the electromagnetic radiation for characteristic times ~200 fs. Thus, the MDC acts as light concentrator, without utilizing actual concentrator based external superstructures, which usually come with increased solar cell surface area. Furthermore, at metal concentrations close to the percolation, the SPs are excited over an extremely broad frequency range with an average photon density in close proximity to the MDC electrode surpassing the incident light intensity by four orders of magnitude (Figure 4-2).

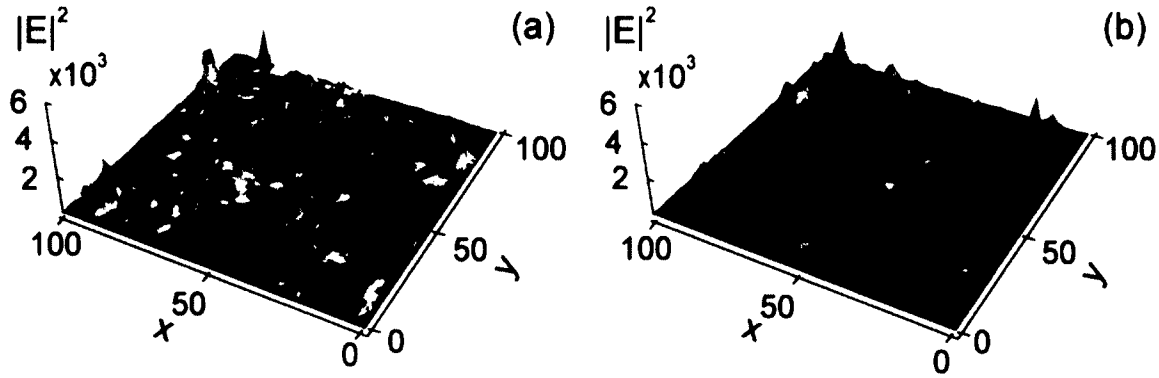

Figure 4-2: The spatial distribution of the local field intensity calculated for a random metal-dielectric composite with metal volume fractions $p = 0.3$. In the calculations we consider two different illumination wavelengths (a) $\lambda = 414nm$ and (b) $\lambda = 800nm$, metal as Silver and dielectric as Si.

The excitation of the surface plasmons (SP) in the metal films traps the light at the nano-scale, which then is absorbed in the adjacent active layer. As a result, the incident radiation is absorbed in the active layer with higher efficiency. The effect of the SP on the active layer absorption is modeled with the effective medium theory with the effective permittivity of the active layer given as:

$$\varepsilon_{AL}^{eff}(\omega, a, d) = \varepsilon'_{AL}(\omega) + i\int_{a}^{d+a} \varepsilon''_{AL}(\omega) M_{2,0}(x,\omega)\frac{dx}{d}, \qquad \textbf{Eq. 4-1}$$

where a is the thickness of the metal composite, d is the thickness of active layer (AL), $\varepsilon'_{AL}(\omega)$ and $\varepsilon''_{AL}(\omega)$ are real and imaginary parts of the permittivity of the bare active layer, and $M_{2,0}(\vec{r},\omega)$ is the local field moment, which are obtained by ensemble, averaging over the composite the local fields intensity enhancement $|E(\vec{r},\omega)|^2/|\vec{E}_0(\vec{r},\omega)|^2$; $\vec{E}_0$ is incident field and $\vec{r}$ is the position vector. In Figure 4-3, we present a parametric plot of the expected enhancement of the complex part of the active layer effective permittivity in close proximity (5nm) to the MDC later. The simulations were

performed using the BE method. The data clearly shows dramatic enhancement of the absorption in the vicinity of the MDC for incident light wavelength higher than the single particle SP resonance (at 515nm). The enhancement is most pronounce at the percolation threshold, which for the sputtered single layer metal films (used in experiments) is at about 60% of metal.

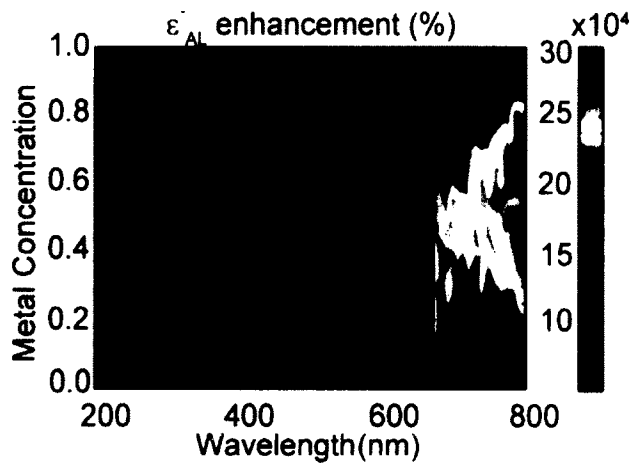

Figure 4-3: Enhancement of complex part of effective permittivity (metal as silver and dielectric as Silicon) of the active layer when compared to the bare silicon permittivity, which leads to anomalous absorption over a wide frequency range.

Once obtained, the effective permittivity of the active layer can be used to calculate light absorption in the active layer. This is done by implementing the net radiation method (NRM) [123] for the segmented cell (Figure 4-4). The fractional absorption within the active layer is calculated by considering all four radiation fluxes:

$$\begin{matrix} S_{i,1} = t_{i-1}S_{i-1,4}, & S_{i,2} = r_i S_{i,1} + t_i S_{i,3} \\ S_{i,3} = t_i S_{i+1,2} & S_{i,4} = r_i S_{i,3} + t_i S_{i,1} \end{matrix}, \qquad \textbf{Eq. 4-2}$$

defined at each functional layer labeled $i = 1 \ldots N$, r_i and t_i, are the reflection and transmission coefficients of each interface, respectively. The above system of $4N$ coupled equations are solved using standard numerical procedure (LU elimination) with

the added conditions $S_{1,1} = 1$ and $S_{N,3} = 1$ (no irradiance reaches the cell from the top). The absorption coefficients within the layers are then given as $A_i(\omega) = S_{i,4} - S_{i+1,1} + S_{i+1,2} - S_{i,3}$, and the absorption factor $A = \int A_a(\omega)u(\omega)d\omega$ within the active layer ($i = a$) will be obtained as a weighted average over the solar spectra $u(\omega)$.

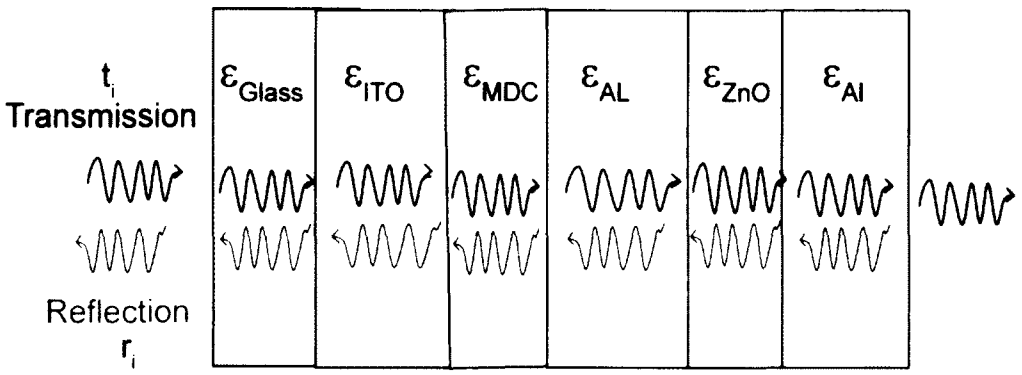

Figure 4-4: Optical model of the solar cell with stack of layers of different thickness and dielectric constants. The black and red arrows indicate the transmission and reflection of light within the layers respectively. Illumination is through a transparent electrode (ITO) with MDC on top of active layer.

The optical efficiency measures the amount of photons absorbed by the active layer with respect to the total electromagnetic energy incident on the film, and it is given by as:

$$\eta_O = \frac{(1-R)\int_o^\infty A\left(\omega, \frac{d}{a}\right)u(\omega)d\omega}{\int_o^\infty u(\omega)d\omega}, \qquad \textbf{Eq. 4-3}$$

where R is the reflection coefficient at the glass (front) interface. Optimization is performed by varying the active layer thickness and inclusion of a MDC electrode layer, which improves the effective absorption coefficient.

4.2.1 SPESC Based on Organic Active Layer

First, we study the optical efficiency of SPESC comprised of SiO_2/ITO/MDC/P3HT:PCBM/Al layers (Figure 4-5).

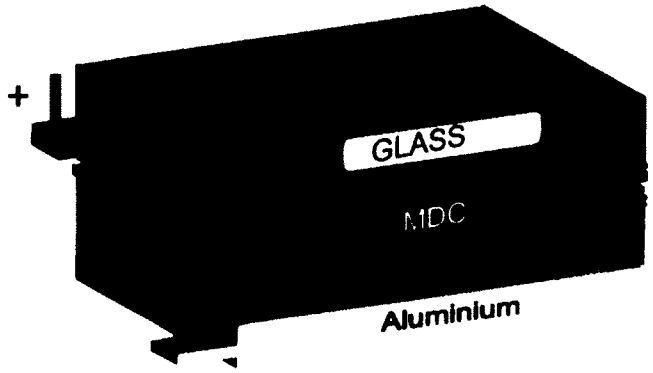

Figure 4-5: Basic layout of plasmonically enhanced photovoltaic device with SiO_2/ITO/MDC/P3HT:PCBM/Al. Illumination is through a transparent electrode (ITO) with MDC on top of active layer.

Using the developed BE code, coupled with the net radiation method (NRM) we seek to obtain the fundamental limit of the power conversion efficiency of the solar cell as function of the active layer (P3HT:PCBM) thickness and MDC metal concentration that is depicted in Figure 4-6 (a) . The incident light illumination is from the Glass side and Silver (Ag) that is sputtered to form the MDC at different metal concentrations. The numerical simulations show well pronounced maxima and minima for the expected optical absorption in the active layer. The maxima correspond to the different order of Fabry-Perot resonances facilitated by the cavity formed by the front transparent electrode and the back Alumina electrode. Figure 4-6 (b) is similar to Figure 4-6 (a) and depicts the fundamental limit of the power conversion efficiency enhancement in percentage due to the incorporation of the MDC and with respect to the original SiO_2/ITO/P3HT:PCBM/Al benchmark device.

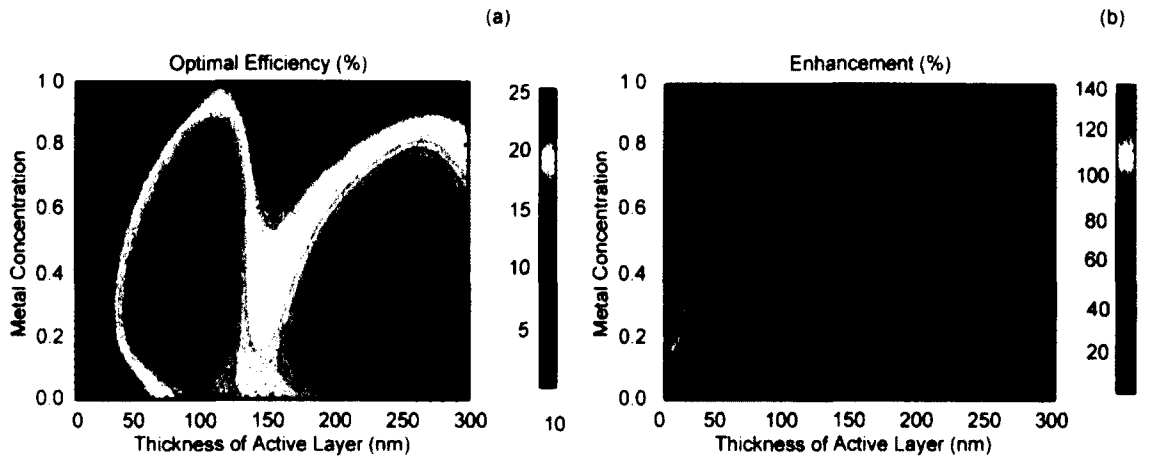

Figure 4-6: Optical efficiency of SiO_2/ITO/MDC/P3HT:PCBM/Al solar cell as function of the active layer (P3HT:PCBM) thickness and MDC metal concentration. A 20nm MDC is applied for all calculations.

The colored areas correspond to parametric conditions where the incorporation of the MCE is beneficial. While the efficiency enhancement due to the MDC layer becomes more pronounce as one shrinks the active layer thickness, the optical efficiency decreases and one needs to achieve a proper trade off. From Figure 4-6 (a) and Figure 4-6 (b), the optimal efficiency is found for metal concentration of between about 20% and about 50% and an active layer thickness of about 50nm and about 100nm and metal concentration of between about 10% and about 40%, and an active layer thickness of about 180nm and about 250nm nm. The maximum optical efficiency of 24% is achieved for active layer thickness of 80nm and metal concentration of 41%. This efficiency is 37% higher compared to the benchmark device and is entirely due to the energy localization and light absorption facilitated by the MDC.

As a second example, we consider an inverted design with respect to the one depicted in Figure 4-5, where the MDC layer is now sandwiched between the Aluminum electrode and the active layer. The fundamental limit of the power conversion efficiency

of this SiO_2/ITO/P3HT:PCBM/MDC/Al solar cell as function of the active layer (P3HT:PCBM) thickness and MDC metal concentration is shown in Figure 4-7 (a). The incident light illumination is again from the Glass (SiO_2) side, and Silver (Ag) is sputtered to form the MDC at different metal concentrations. Figure 4-7 (b) is similar to Figure 4-7 (a) and depicts the fundamental limit of the power conversion efficiency enhancement in percentage due to the incorporation of the MDC and with respect to the benchmark SiO_2/ITO/P3HT:PCBM/Al device.

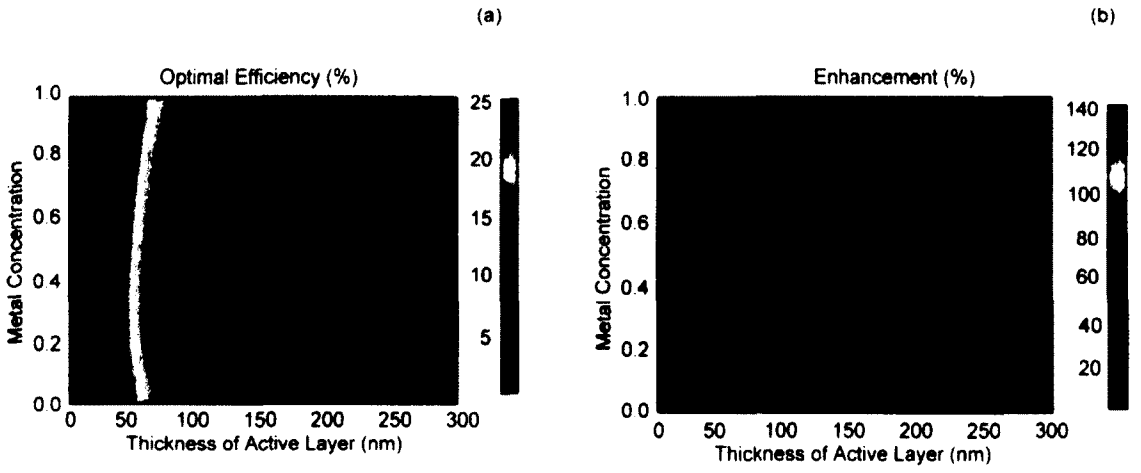

Figure 4-7: Optical efficiency of SiO_2/ITO/P3HT:PCBM/MDC/Al solar cell as function of the active layer (P3HT:PCBM) thickness and MDC metal concentration. A 20nm MDC is applied for all calculations.

The colored areas correspond to parametric conditions where the incorporation of the MDC is beneficial. In Figure 4-7 (a) and Figure 4.7 (b), the optimal efficiency is at a metal concentration of between about 20% and about 60% and an active layer thickness of about 80nm and about 140nm and metal concentration of between about 10% and about 60% and an active layer thickness of about 200nm and about 300nm. Clearly, in this design the optimal performance is achieved for thicker cells (thickness 250nm), and,

accordingly, the enhancement provided by the MDC is smaller (~15%) compared to the preceding design.

4.2.2 SPESC Based on Inorganic Active Layer

Now we consider an inorganic semiconductor (c-Si or a-Si:H) as active layer with MDC on the top of the active layer as shown in Figure 4-8.

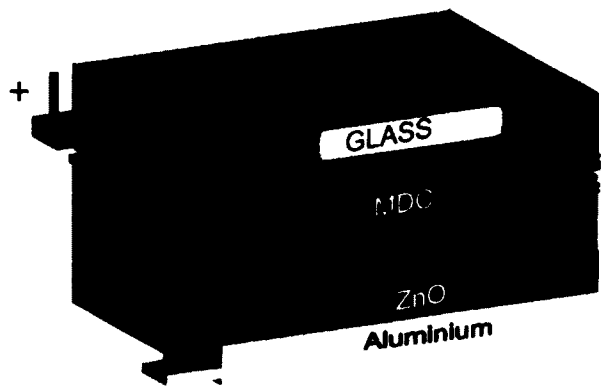

Figure 4-8: Basic layout of plasmonically enhanced photovoltaic device with SiO_2/ITO/MDC/c-*Si* (a-*Si*:H) /ZnO/Al. Illumination is through a transparent electrode (ITO) with MDC on top of active layer.

The fundamental limit of the power conversion efficiency of a SiO_2/MCE/*c*-Si/ZnO/Al solar cell as function of the active layer (single crystal silicon, *c*-Si) thickness and MCE metal concentration is depicted in Figure 4-9 (a). The incident light illumination is from the Glass (SiO_2) side and Gold (Au) is sputtered to form the MCE at different metal concentrations. Figure 4-9 (b) is similar to Figure 4-9 (a) and depicts the fundamental limit of the power conversion efficiency enhancement in percentage due to the incorporation of the MDC and with respect to the original SiO_2/*c*-Si/ZnO/Al device. The colored areas correspond to parametric conditions where the incorporation of the MDC is beneficial.

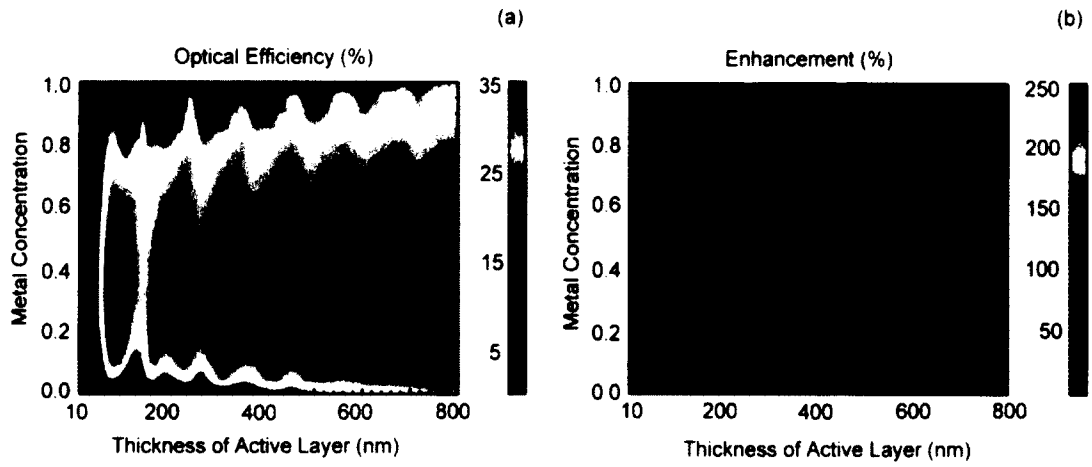

Figure 4-9: Optical efficiency of SiO_2/MCE/*c*-Si/ZnO/Al solar cell as function of the active layer (crystalline Silicon, *c*-Si) thickness and MDC metal concentration. A 20nm MDC is applied for all calculations.

The optical (absorption) efficiency of inorganic SPESC and enhancement in efficiency when compared to the control inorganic solar cell without MDC are shown in Figure 4-9 (b). The improvement in absorption is substantial, and depends on both the thickness of the active layer and metal concentration. Introduction of the semi-continuous metal layer allows development of rather thin devices (with thickness of 380nm) that operate at the same efficiencies as much thicker control devices (thickness >1microns).

Figure 4-10 (a) depicts the fundamental limit of the power conversion efficiency of a SiO_2/MCE/*a*-Si:H/ZnO/Al solar cell as function of the active layer (hydrogenated amorphous silicon, *a*-Si:H) thickness and MCE metal concentration. The incident light illumination is from the Glass (SiO_2) side and Gold (Au) is sputtered to form the MCE at different metal concentrations. Figure 4-10 (b) is similar to Figure 4-10 (a) and depicts the fundamental limit of the power conversion efficiency enhancement in percentage due to the incorporation of the MCE and with respect to the original SiO_2/*a*-Si:H/ZnO/Al device.

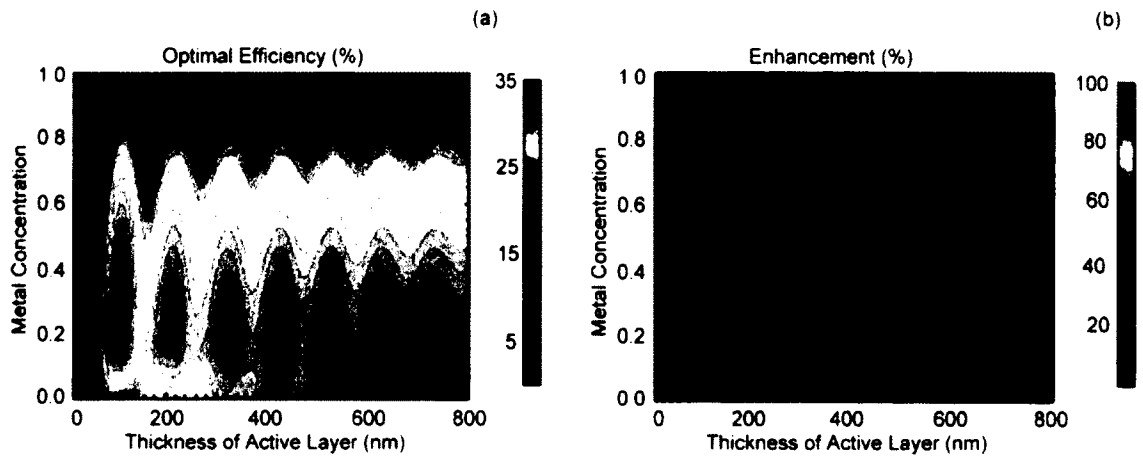

Figure 4-10: Optical efficiency of SiO_2/MCE/*a*-Si:H/ZnO/Al solar cell as function of the active layer (amorphous Silicon, *a*-Si) thickness and MDC metal concentration. A 20nm MDC is applied for all calculations.

The colored areas correspond to parametric conditions where the incorporation of the MCE is beneficial. In Figure 4-10 (a) and Figure 4-10 (b), the highest efficiency is at a metal concentration of between about 10% and about 40% and an active layer thickness of between about 100 and about 700 nm. The best optical solar cell efficiency of 27% is achieved for active layer thickness of as little as 110nm, at which case the enhancement provided by the MDC higher than 50%. We must note that the extremely high efficiency predicted for extremely thin cells (thickness <20nm) will not translate into an equivalent photovoltaic (PV) efficiency due to quenching. Thus, the optical results presented in Figure 4.10(a) and Figure 4-10(b) should only be thrusted for thicknesses >50nm.

4.3 Generation Rate and Optimal Photovoltaic (PV) Solar Cell Efficiency

To study the actual photovoltaic (PV) power conversion efficiency we developed a simple model, where the general transport equations of electrons and holes are solved analytically, providing the carrier concentration profiles and generation dependent electrical current [90].

For thin-film solar cells, where the device thickness is smaller than the photon penetration depth, a homogeneous generation rate can be considered. The generation rate can be obtained from the optical model presented in preceding chapter. Using the spectrum averaged optical absorption efficiency given by Eq. 4.3, we write the homogeneous generation rate for thin-film solar cell as estimated as:

$$G(d,p) = \frac{\eta_O(d,p)P_0}{(hc/\lambda)d}, \qquad \textbf{Eq. 4-4}$$

where the device thickness is d, the MDC metal concentration is p, and P_0 is total incident optical power (1000 W/m^2 for AM1.5 solar radiation). This constant generation rate is then used to solve the drift-diffusion equations for the electrons and holes in a crystalline silicon based pn-junction cell. The geometry of the junction cells is shown in Figure 4-11:

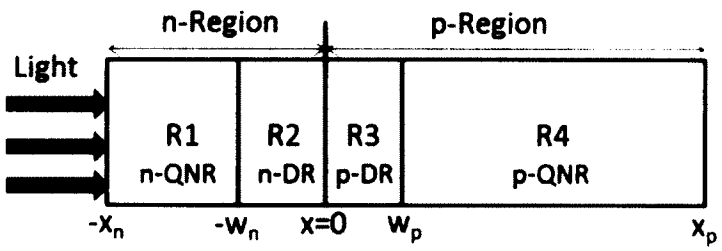

Figure 4-11: Basic device structure of PN junction silicon solar cell used for modeling.

The n-type depletion region (n-DR), R3 is p-type depletion region (p-DR) and R4 is p-type quasi neutral region (p-QNR). The transportation of charge carriers in a silicon solar cell is governed by two mechanism, drift and diffusion. The absorption of photons within a silicon solar cell increases the number of free charge carriers, but the recombination process annihilate free charge carriers. General transport equations based

on drift, diffusion, generation (G) and recombination (R) of electrons and holes in PN junction silicon solar cell are well known [123]:

$$D_n.\frac{d^2n(x)}{dx^2} + \mu_n.E(x).\frac{dn(x)}{dx} + \mu_n.n(x).\frac{dE(x)}{dx} - R_n(x) + G_n(x) = 0, \quad \textbf{Eq. 4-5}$$

$$D_p.\frac{d^2p(x)}{dx^2} + \mu_p.E(x).\frac{dp(x)}{dx} + \mu_p.p(x).\frac{dE(x)}{dx} - R_p(x) + G_p(x) = 0, \quad \textbf{Eq. 4-6}$$

where $D_n(D_p)$ is electron (hole) diffusion coefficient, E is the internal electric field developed in the depletion region, μ_n (μ_p) is the mobility of electron (hole), R_n (R_p) is the recombination rate of electrons (holes) and G_n (G_p) is generation rate of electrons (holes). With the assumption that the electric field exists only in the depletion region (DR) and given by Eq. (4.7) and (4.8):

$$E(x) = \frac{V_t}{(L_{nd})^2}(W_n + x) \qquad -W_n < x < 0, \quad \textbf{Eq. 4-7}$$

$$E(x) = \frac{V_t}{(L_{pd})^2}(W_p - x) \qquad 0 < x < W_p, \quad \textbf{Eq. 4-8}$$

where V_t is the thermal voltage, and $L_{nd}(L_{pd})$ is the Debye length of the electron (hole). In quais-neutral regions (QNR), electric field vanishes as a result the transport Eqns. (4.5) and (4.6) in these regions (R1 and R2) are simplified to Eqns (4.9) and (4.10) given below:

$$D_n.\frac{d^2n(x)}{dx^2} - \frac{n(x) - n_{p0}}{t_n} + G_n(x) = 0, \quad \textbf{Eq. 4-9}$$

$$D_p.\frac{d^2p(x)}{dx^2} - \frac{p(x) - p_{n0}}{t_p} + G_p(x) = 0, \qquad \textbf{Eq. 4-10}$$

where, the recombination rates, $R_n(x) = \frac{n(x)-n_{p0}}{t_n}$ [illegible] $t_n \frac{p(x)-p_{n0}}{t_n}$, n_{p0} is the electron minority concentration in the p-QNR, p_{n0} is the hole minority concentration in the n-QNR and $t_n(t_p)$ is the electron (hole) minority carrier lifetime.

Under constant generation of electrons and holes, $G_n = G_p = G$, the solutions of the electron transport equation in the p-QNR (region R4) and the hole transport equation in the n-QNR (region R1) given by equations (4.11) and (4.12) are:

$$n(x) = G.t_n + n_{p0} - e^{\frac{W_p+x}{L_n}}\left(G.t_n + n_{p0}\left(1 - e^{\frac{V}{V_t}}\right)\right), \qquad \textbf{Eq. 4-11}$$

$$p(x) = G.t_p + p_{n0} - e^{\frac{W_n+x}{L_p}}\left(G.t_p + p_{n0}\left(1 - e^{\frac{V}{V_t}}\right)\right). \qquad \textbf{Eq. 4-12}$$

The solutions of the electron transport equation in the p-DR (region R3) and the hole transport equation in the n-DR (region R2) given by equations (4.13) and (4.14) are:

$$p(x) = e^{\frac{x(2W_p - x)}{2L_{pd}}} c_4 - \frac{G{L_{pd}}^2}{D_p} + \frac{\sqrt{2}L_{pd}(c_3 D_p - GW_p)D_+\left[\frac{-W_p + x}{\sqrt{2}L_{pd}}\right]}{D_p},$$

$$n(x) = e^{\frac{-x(2W_p - x)}{2L_{pd}}} c_3 + \frac{G{L_{nd}}^2}{D_n} \qquad \textbf{Eq. 4-13}$$

$$+ \frac{\sqrt{2\pi}L_{pd} e^{\frac{(W_p - x)^2}{2L_{pd}^2}} (c_4 D_n - GW_p) erf\left[\frac{-W_p + x}{\sqrt{2}L_{pd}}\right]}{2D_n},$$

$$p(x) = e^{\frac{x(2W_n + x)}{2L_{nd}}} c_2 + \frac{G{L_{nd}}^2}{D_p}$$

$$+ \frac{\sqrt{2\pi}L_{nd} e^{\frac{(W_n + x)^2}{2L_{nd}^2}} (c_1 D_p + GW_n) erf\left[\frac{W_n + x}{\sqrt{2}L_{nd}}\right]}{2D_p}, \qquad \textbf{Eq. 4-14}$$

$$n(x) = e^{\frac{-x(2W_n + x)}{2L_{nd}}} c_2 - G{L_{nd}}^2 + \frac{\sqrt{2\pi}L_{nd}(c_1 D_n + GW_n D_+\left[\frac{W_n + x}{\sqrt{2}L_{nd}}\right]}{2D_p},$$

where, D_+ is Dawson's function, $L_n(L_p)$ is the electron (hole) diffusion length. The intrinsic boundary conditions for bulk device are used to solve transport equations in the QNRs. Where the minority carriers concentrations are assumed to have finite value as device thickness tends to reach infinity. These boundary conditions are that n and p are finite as $x = \pm\infty$, $p(-w_n) = p_{n0}(e^{V/V_t} - 1)$ and $n(w_p) = n_{p0}(e^{V/V_t} - 1)$. The continuity of carrier concentration profiles and currents are enforced at the boundaries of n-QNR, n-DR, p-DR and p-QNR as the boundary conditions to calculate integration

constants c1 , c2 , c3 and c4. Once the analytical expressions of charge carriers are obtained, the simple analytical expression for the current, depending on generation, is calculated. The total current is constant at each point within the device. The electron and hole currents are calculated at the edge of the depletion regions. The electron current i_n at W_p, the hole current i_p at$-W_n$and total current i_{total} are given by equations (4.15), (4.16), and (4.17) respectively.

$$i_n = \frac{q\, D_n\, n_{p0}(1 - e^{\frac{V}{V_t}})}{L_p} + q\, L_n G, \qquad \textbf{Eq. 4-15}$$

$$i_p = \frac{q\, D_p\, p_{n0}(1 - e^{\frac{V}{V_t}})}{L_p} + q\, L_p G, \qquad \textbf{Eq. 4-16}$$

$$i_{total} = q.G.(L_p + L_n) + \left(\frac{q\, D_p\, p_{n0}}{L_p} + \frac{q\, D_n\, n_{p0}}{L_n}\right)\left(1 - e^{\frac{V}{V_t}}\right). \qquad \textbf{Eq. 4-17}$$

However, for a thin film solar cell, as the thickness reduces to smaller value, the saturation current tends to achieve very high value when these boundary conditions are used. This shows that one must be careful while considering thin devices. For such thin devices, it is probably more meaningful to consider finite surface recombination velocity as boundary condition.

The electron and hole transport equations [123] are solved for homogeneous generation rate in quasi neutral regions using surface recombination boundary conditions,

given in equation (4.18), to obtain generation current j_G and saturation current j_s shown in equation (4.19).

$$D_n\partial_x[n(x)]|_{x=x_p} = -n(x_p)S_n, \quad n(w_p) = n_{p0}(e^{V/V_t} - 1)$$
$$p(-w_n) = p_{n0}(e^{V/V_t} - 1), \quad D_p\partial_x[p(x)]|_{x=-x_n} = p(-x_n)S_p \quad \textbf{Eq. 4-18}$$

Here, $S_n(S_p)$ is electron (hole) minority carrier surface recombination velocity, $D_n(D_p)$ is electron (hole) diffusion coefficient, $w_n(w_p)$ is depletion width of n-region (p-region), V_t is thermal voltage, $x_n(x_p)$ is thickness of n-region (p-region), and $n_{p0}(p_{n0})$ is electron (hole) minority concentration in p-region (n-region).

$$j_G = qG(d,m)\left(L_n\frac{q_n + \tanh\left[\frac{l_p}{L_n}\right] - q_n\mathrm{sech}\left[\frac{l_p}{L_n}\right]}{1 + q_n\tanh\left[\frac{l_p}{L_n}\right]} + L_p\frac{q_p + \tanh\left[\frac{l_n}{L_p}\right] - q_p\mathrm{sech}\left[\frac{l_n}{L_p}\right]}{1 + q_p\tanh\left[\frac{l_n}{L_p}\right]}\right), \quad \textbf{Eq. 4-19}$$

$$j_s = qS_n n_{p0}\frac{1 + q_n^{-1}\tanh\left[\frac{l_p}{L_n}\right]}{1 + q_n\tanh\left[\frac{l_p}{L_n}\right]} + qS_p p_{n0}\frac{1 + q_p^{-1}\tanh\left[\frac{l_n}{L_p}\right]}{1 + q_p\tanh\left[\frac{l_n}{L_p}\right]}.$$

Here, $q_n = L_nS_n/D_n = \tau_nS_n/L_n$, $q_p = L_pS_p/D_p = \tau_pS_p/L_p$, $l_n = x_n - w_n$, $l_p = x_p - w_p$, and $L_n = \sqrt{\tau_nD_n}(L_p = \sqrt{\tau_pD_p})$ is the electron (hole) diffusion length.

The total electrical current from the solar cell can be expressed as:

$$j_t = j_G + j_{G,DR} - j_s(e^{V/V_t} - 1), \quad \textbf{Eq. 4-20}$$

where j_G is generation current, $j_{G,DR} = qwG$, is the current contributed by generation in depletion region, w being depletion width and q is elementary charge, and j_s is saturation

current. The electrical power is the product of total current and bias voltage given by $P = Vj_t$. Now, the optimal power can be expressed as:

$$P_{opt} = j_t V_t (2 - \mathrm{W}[ej_t/j_s] - \mathrm{W}^{-1}[ej_t/j_s]), \qquad \textbf{Eq. 4-21}$$

where W is Lambert W-function and e is the base of the natural logarithm[90]. The optimal power from the solar cell is then calculated as a function of device active layer thickness and metal concentration in MDC Figure 4-12 (a).

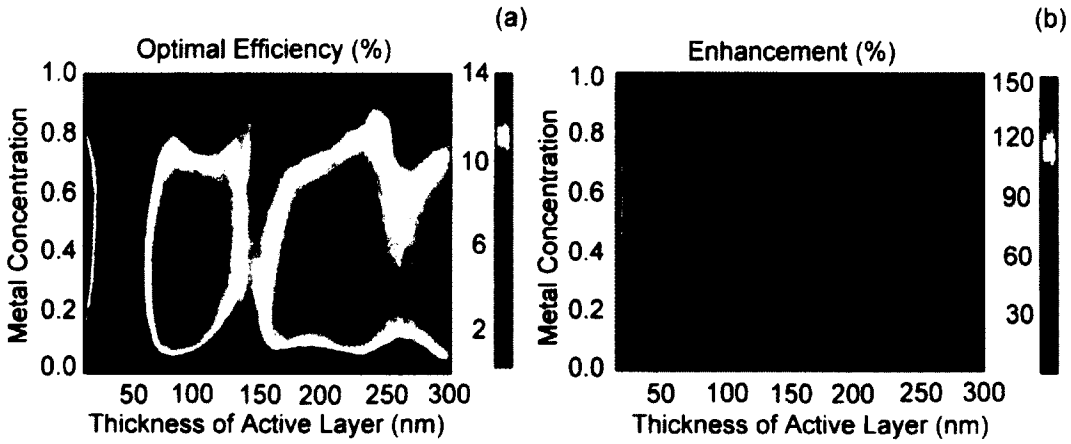

Figure 4-12: Optimal efficiency of SiO_2/ITO/ MDCE/ *Si* /ZNO/Al solar cell as function of the active layer (Silicon, *Si*) thickness and MDCE metal concentration.

The optimal efficiency is at a metal concentration of between about 20% and about 60% and an active layer thickness of about 80nm and about 140nm and metal concentration of between about 10% and about 60% and an active layer thickness of about 200nm and about 300nm. Similar to Figure 4-12 (a), Figure 4-12 (b) depicts the optimal power enhancement in percentage due to the incorporation of the MCE and with respect to the original SiO_2/*c*-Si:H/ZnO/Al device. The improvement in total power is substantial, and depends on both the thickness of the active layer and metal concentration. Introduction of the semi-continuous metal layer allows development of

rather thin devices (with thickness of 100 nm) that operate at the same efficiencies as much thicker control devices (thickness >1microns).

CHAPTER 5

CONCLUSION

5.1 Concluding Remarks

In this work, we studied the electromagnetic properties of nano-structured random-composite materials, which exhibit anomalous phenomena such as giant enhancements of optical nonlinearities due to collective excitation of surface plasmons (SPs).

We introduced an efficient and exact numerical method for calculation of the conductivity and local-field distributions in 3D inhomogeneous metal-dielectric composite materials. Due to the highly demanding run times and operational memory requirements in the 3D case, we implemented the Message Passing Interface (MPI) protocol to parallelize the Block elimination (BE) method and achieved the desired code functionality.

The field distribution, i.e. the solution of the SP eigenproblem, allowed us to study the intrinsic SP modes excited in the composites, which is similar to the 2D case in that it follows a non-Gaussian a log-normal function, which explains the metal-dielectric phase transition of the system. Also, we have provided the basis for developing a scaling theory for the higher order-field moments, which are responsible for the nonlinear optical

response of the system. The developed scaling theory is in excellent agreement with the numerical calculations.

As already shown, surface plasmons localization-delocalization transition can occur in the 1D and 2D cases; here, we studied the nature of the localization for a first time in the 3D case. Highly accurate estimates of the conductivity and correlation length exponents have been obtained and found to be in good agreement with previous estimates.

Our data shows distinct evidence of singularities in the surface plasmon density of states and localization length, correlating with results previously obtained for two dimensional systems. This leads to the main finding of this work, i. e. a delocalization of surface plasmon states in percolating metal-dielectric composite materials is universally present regardless of the dimensionality of the problem.

Relying on the knowledge gained on the three dimensional (3D) metal-dielectric composites, we integrated the MDC electrode in the existing thin film silicon solar cells and designed a new type of solar cell, which we refer to as Surface Plasmon Enhanced Solar Cell (SPESC). With this inclusion of the MDC electrode in the solar cell, we estimated a substantial improvement in absorption in active layer, which in return aids in a huge enhancement in optical efficiency.

We modeled SPESCs using both organic (polymer) and inorganic semiconducting active layers. We used P3HT:PCBM as active layer in organic solar cells; a maximum optical efficiency of 24% is achieved for active layer thickness of 80nm and metal concentration of 41%. This efficiency is 37% higher compared to the benchmark device and is entirely due to the energy localization and light absorption facilitated by the MDC.

We used as crystalline silicon as active layer in inorganic solar cell there is a substantial improvement in the optical (absorption) efficiency when compared to the benchmark device.

We proposed a purely analytical model for thin film silicon solar cell. The general transport equations of electron and hole were solved analytically to compute carrier concentration profiles and generation dependent electrical current. We developed a simple model with a constant generation approximation and calculated electrical output currents at different generation rates showing electrical current increases with increasing generation rate. We employed this analytical model for calculation of generation current and obtained the optimal electrical efficiency as a function of thicknesses of the *Si* silicon layer and also metal concentration of MDC electrode. We observed that there is a substantial enhancement in the electrical efficiency of SPESC when compared to bare solar cells without MDC electrode.

APPENDIX A

BLOCK ELIMINATION CODES IN FORTRAN

A.1 Serial Code

```
parameter (lrows=50) c size of the system LX L
parameter (krows=50) c number of layers
parameter (nreal=1) c number of realizations

      complex(KIND=8) h(lrows,lrows*krows,lrows*krows)
      complex(KIND=8) sigm1(lrows,lrows,krows), sigm2(lrows,lrows,krows)
      complex(KIND=8) sigm3(lrows,lrows,krows),cn(lrows*lrows*krows)
      complex(KIND=8) s(lrows,lrows*krows)
      complex(KIND=8) pot(lrows,lrows,krows),sigma(50),sigme(50),sigm(1,nreal)
      complex(KIND=8) Sm,Sd,Sd2
      complex(KIND=8) big_c(2*lrows*krows),current(lrows,lrows,krows)
      complex(KIND=8) big_m(2*lrows*krows,2*lrows*krows) !,Ham(KL2,KL2)
      complex(KIND=8) Ex(lrows-1,lrows-1,krows-1),Ey(lrows-1,lrows-1,krows-1)
      complex(KIND=8)Ez(lrows-1,lrows-1,krows-1),Epl(lrows-1,lrows-1,krows-
      1),Eplm(lrows-1,lrows-1,krows-1)!,Epls(lrows-1,lrows-1,krows-1)
      complex(KIND=8) cons,Epls((lrows-1)*(lrows-1)*(krows-1)),Eplsn((lrows-
      1)*(lrows-1)*(krows-1)*100)
      real(KIND=8) lam1,pr,m,tita,lamp,lamt,epsb,random!,sigm(2*1,nreal)
      integer n,r,k,l,m,corr,g,n1,n2,KL2,KL,V,myid,ierr,numprocs,t
      integer i,j,kk,nnn,rrr,pp,nc,ik,jk,km,rc,cen,seed,li
      real(KIND=8) Et(krows,nreal)
      real(KIND=8) pm(nreal),p,nm(nreal),pmk,fpm(nreal)
      Open(unit=7,file='I_50_test_pc_1_300_3.dat',status='unknown')


!c    SUBROUTINE VECTORS
      Sd=(2.2,0.0) c permittivity of dielectric
      Sd2=(2.2,0.0) c permittivity of dielectric
      nc=krows
      pp=1
      n1=lrows
```

```
n2=krows
KL2=n1*n1*n2
KL=n1*n2
Sm=(1.570708,0.01478) c permittivity of metal

do 110 lp=1,l
p=0.2488126+lp*0.0000000

do 100 kk=1,nreal

do k=1,n1
do i=1,n1
do j=1,n2

sigm1(k,i,j)=Sd2
sigm2(k,i,j)=Sd2
sigm3(k,i,j)=Sd2
enddo
enddo
enddo

do i=1,n1
do j=1,KL
do k=1,KL
h(i,j,k)=(0.0,0.0)
enddo
s(i,j)=(0.0,0.0)
enddo
enddo

do i=1,KL2-n1*n2
cn(i)=(0.0,0.0)
enddo
```

```
      do i=KL2-KL+1,KL
      cn(i)=1.
      enddo

      do i=1,n1
      do j=1,n1
      do k=1,nc
      if(RAND(0).le.p) then
      sigm1(i,j,k)=Sm
      else
      sigm1(i,j,k)=Sd
      endif
      if(RAND(0).le.p) then
      sigm2(i,j,k)=Sm
      else
      sigm2(i,j,k)=Sd
      endif

      if(RAND(0).le.p) then
      sigm3(i,j,k)=Sm
       else

       sigm3(i,j,k)=Sd
      endif

      enddo
      enddo
    enddo

!c    BUILDING VECTORS
      do i=2,n1-1
      do j=2,n1-1
      do k=2,n2-1
```

```
h(i,(j-1)*n2+k,(j-1)*n2+k)=sigm1(i,j,k)+sigm2(i,j,k)+sigm3(i,j,k)+sigm1(i-
1,j,k)+sigm2(i,j-1,k)+sigm3(i,j,k-1)
h(i,(j-1)*n2+k,(j-1)*n2+k+1)=-sigm3(i,j,k)
h(i,(j-1)*n2+k,(j-1)*n2+k-1)=-sigm3(i,j,k-1)

h(i,(j-1)*n2+k,(j-2)*n2+k)=-sigm2(i,j-1,k)
h(i,(j-1)*n2+k,j*n2+k)=-sigm2(i,j,k)

s(i,(j-1)*n2+k)=-sigm1(i,j,k)
enddo

h(i,(j-1)*n2+1,(j-1)*n2+1)=sigm1(i,j,1)+sigm2(i,j,1)+sigm3(i,j,1)+sigm1(i-
1,j,1)+sigm2(i,j-1,1)+sigm3(i,j,n2)

h(i,(j-1)*n2+1,(j-1)*n2+2)=-sigm3(i,j,1)
h(i,(j-1)*n2+1,(j-1)*n2+n2)=-sigm3(i,j,n2)
h(i,(j-1)*n2+n2,(j-1)*n2+n2)=sigm1(i,j,n2)+sigm2(i,j,n2)+sigm3(i,j,n2)+sigm1(i-
1,j,n2)+sigm2(i,j-1,n2)+sigm3(i,j,n2-1)
h(i,(j-1)*n2+n2,(j-1)*n2+n2-1)=-sigm3(i,j,n2-1)
h(i,(j-1)*n2+n2,(j-1)*n2+1)=-sigm3(i,j,n2)

h(i,(j-1)*n2+1,(j-2)*n2+1)=-sigm2(i,j-1,1)
h(i,(j-1)*n2+n2,(j-2)*n2+n2)=-sigm2(i,j-1,n2)
h(i,(j-1)*n2+1,j*n2+1)=-sigm2(i,j,1)
h(i,(j-1)*n2+n2,j*n2+n2)=-sigm2(i,j,n2)

s(i,(j-1)*n2+1)=-sigm1(i,j,1)
s(i,(j-1)*n2+n2)=-sigm1(i,j,n2)
enddo

h(i,1,1)=sigm1(i,1,1)+sigm2(i,1,1)+sigm3(i,1,1)+sigm1(i-
1,1,1)+sigm2(i,n1,1)+sigm3(i,1,n2)
h(i,1,2)=-sigm3(i,1,1)
h(i,1,n2)=-sigm3(i,1,n2)
```

```
h(i,n2,n2-1)=-sigm3(i,1,n2-1)
h(i,n2,1)=-sigm3(i,1,n2)
h(i,n2,n2)=sigm1(i,1,n2)+sigm2(i,1,n2)+sigm3(i,1,n2)+sigm1(i-
1,1,n2)+sigm2(i,n1,n2)+sigm3(i,1,n2-1)
h(i,(n1-1)*n2+1,(n1-
1)*n2+1)=sigm1(i,n1,1)+sigm2(i,n1,1)+sigm3(i,n1,1)+sigm1(i-1,n1,1)+sigm2(i,n1-
1,1)+sigm3(i,n1,n2)
h(i,(n1-1)*n2+1,(n1-1)*n2+2)=-sigm3(i,n1,1)
h(i,(n1-1)*n2+1,(n1-1)*n2+n2)=-sigm3(i,n1,n2)
h(i,(n1-1)*n2+n2,(n1-1)*n2+n2-1)=-sigm3(i,n1,n2-1)
h(i,(n1-1)*n2+n2,(n1-1)*n2+1)=-sigm3(i,n1,n2)
h(i,(n1-1)*n2+n2,(n1-
1)*n2+n2)=sigm1(i,n1,n2)+sigm2(i,n1,n2)+sigm3(i,n1,n2)+sigm1(i-
1,n1,n2)+sigm2(i,n1-1,n2)+sigm3(i,n1,n2-1)

h(i,1,n2+1)=-sigm2(i,1,1)
h(i,n2,2*n2)=-sigm2(i,1,n2)
h(i,(n1-1)*n2+1,(n1-2)*n2+1)=-sigm2(i,n1,1)
h(i,(n1-1)*n2+n2,(n1-2)*n2+n2)=-sigm2(i,n1,n2)

s(i,1)=-sigm1(i,1,1)
s(i,n2)=-sigm1(i,1,n2)
s(i,(n1-1)*n2+1)=-sigm1(i,n1,1)
s(i,(n1-1)*n2+n2)=-sigm1(i,n1,n2)
enddo

do i=2,n1-1
do k=2,n2-1
h(i,(n1-1)*n2+k,(n1-
1)*n2+k)=sigm1(i,n1,k)+sigm2(i,n1,k)+sigm3(i,n1,k)+sigm1(i-1,n1,k)+sigm2(i,n1-
1,k)+sigm3(i,n1,k-1)
h(i,k,k)=sigm1(i,1,k)+sigm2(i,1,k)+sigm3(i,1,k)+sigm1(i-
1,1,k)+sigm2(i,n1,k)+sigm3(i,1,k-1)
h(i,k,k+1)=-sigm3(i,1,k)
h(i,k,k-1)=-sigm3(i,1,k-1)
```

```
h(i,(n1-1)*n2+k,(n1-1)*n2+k+1)=-sigm3(i,n1,k)
h(i,(n1-1)*n2+k,(n1-1)*n2+k-1)=-sigm3(i,n1,k-1)

s(i,k)=-sigm1(i,1,k)
s(i,(n1-1)*n2+k)=-sigm1(i,n1,k)
enddo
enddo

do j=1,n1
do k=1,n2
h(1,(j-1)*n2+k,(j-1)*n2+k)=(1.0,0.0)
h(n1,(j-1)*n2+k,(j-1)*n2+k)=(1.0,0.0)
if (j.ge.2.and.j.le.n1-1) then
h(j,k,n2+k)=-sigm2(j,1,k)
h(j,(n1-1)*n2+k,(n1-2)*n2+k)=-sigm2(j,n1-1,k)
h(j,k,(n1-1)*n2+k)=-sigm2(j,n1,k)
h(j,(n1-1)*n2+k,k)=-sigm2(j,n1,k)
endif
enddo
enddo

do 20 k=2,n1-2
do i=1,2*KL
do j=1,2*KL
big_m(i,j)=(0.0,0.0)
enddo
enddo

do i=1,KL
do j=1,KL
big_m(i,j)=h(k,i,j)
big_m(i+KL,j+KL)=h(k+1,i,j)
enddo
```

```
      big_m(i,i+KL)=s(k,i)
      big_m(i+KL,i)=s(k,i)
      enddo

      do 5 l=1,KL
   do 6 i=l+1,2*KL
      if(big_m(i,l).ne.(0.0,0.0)) then
   cons=big_m(i,l)
   do 7 j=l,2*KL
   big_m(i,j)=big_m(i,j)-cons*big_m(l,j)/big_m(l,l)
7  continue
      endif
6  continue
5  continue

      do i=1,KL
      do j=1,KL
      h(k,i,j)=big_m(i,j)
      if (i.gt.j) then
      h(k,i,j)=big_m(i,j+KL)
      endif
      h(k+1,i,j)=big_m(i+KL,j+KL)
      enddo
      s(k,i)=big_m(i,i+KL)
      enddo
20    continue

      do i=1,2*KL
      do j=1,2*KL
      big_m(i,j)=(0.0,0.0)
      enddo
      enddo
```

```
      do i=1,KL
      do j=1,KL
      big_m(i,j)=h(n1-1,i,j)
      enddo
      big_m(i,i+KL)=s(n1-1,i)
      enddo

   do 15 l=1,KL
   do 16 i=l+1,2*KL
      if(big_m(i,l).ne.(0.0,0.0)) then
   cons=big_m(i,l)
   do 17 j=l,2*KL
   big_m(i,j)=big_m(i,j)-cons*big_m(l,j)/big_m(l,l)
17 continue
      endif
16 continue
15 continue

      do i=1,KL
      do j=1,KL
      h(n1-1,i,j)=big_m(i,j)
      if (i.gt.j) then
      h(n1-1,i,j)=big_m(i,j+KL)
      endif
      enddo
      s(n1-1,i)=big_m(i,i+KL)
      enddo

!c_____________________________________________________________
!c
!c     BLOCKS ELIMINATION 2
!c    ____________________________________________________________
      do 28 k=n1,2,-1
```

```
        do i=1,2*KL
        do j=1,KL
        big_m(i,j)=(0.0,0.0)
        enddo
        enddo

        do i=1,2*KL
        big_c(i)=cn((k-2)*KL+i)
        enddo

        do i=1,KL
        do j=1,KL
                if (i.le.j) then
                        big_m(i+KL,j)=h(k,i,j)
                endif
                if(i.gt.j) then
                        big_m(i,j)=h(k-1,i,j)
                endif
        enddo
        big_m(i,i)=s(k-1,i)
        enddo

    do 8 j=0,KL-1
    do 9 i=j+1,2*KL-1
    big_c(2*KL-i)=big_c(2*KL-i)-big_c(2*KL-j)*big_m(2*KL-i,KL-j)/big_m(2*KL-
j,KL-j)
    big_m(2*KL-i,KL-j)=0.0
 9  continue
 8  continue

    do i=1,KL
    big_c(KL+i)=big_c(KL+i)/big_m(KL+i,i)
    enddo
```

```
      do i=1,2*KL
      cn((k-2)*KL+i)=big_c(i)
      enddo

28    continue

      do i=1,n1
      do j=1,n1
      do k=1,n2
      pot(i,j,k)=cn((i-1)*KL+(j-1)*n2+k)
      enddo
      enddo
      enddo
!c    open(3,file='pots.dat',status='unknown')
      do i=1,n1-1
    do j=1,n1-1
      do k=1,n2-1

    Ex(i,j,k)=-(n1-1)*(pot(i+1,j,k)-pot(i,j,k))
    Ey(i,j,k)=-(n1-1)*(pot(i,j+1,k)-pot(i,j,k))
      Ez(i,j,k)=-(n1-1)*(pot(i,j,k+1)-pot(i,j,k))


Epl(i,j,k)=Ex(i,j,k)*CONJG(Ex(i,j,k))+Ey(i,j,k)*CONJG(Ey(i,j,k))+Ez(i,j,k)*CONJG(Ez
(i,j,k))*0.01

    enddo
    enddo
    enddo

    sigm(pp,kk)=0.0
```

```
      do k=1,n2-1
      Et(k,kk)=0
      do i=1,n1-1
    do j=1,n1-1

sigm(pp,kk)=sigm(pp,kk)+sigm1(i,j,k)*(Ex(i,j,k))*CONJG(Ex(i,j,k))+sigm2(i,j,k)*(Ey(i,
j,k))*CONJG(Ey(i,j,k))
    sigm(pp,kk)=sigm(pp,kk)+sigm3(i,j,k)*(Ez(i,j,k))*CONJG(Ez(i,j,k))
      enddo
      enddo
      enddo
    li=0
    do i=1,n1-1
    do j=1,n1-1
    do k=1,n2-1
!     write(7,*) Epl(i,j,k),i,j,k,kk,myid
     li=li+1
     Epls(li)=Epl(i,j,k)
     enddo
    enddo
    enddo
    pmk=0.0
    sigma(lp)=(0.0,0.0)
    do i=1,nreal
    sigma(lp)=sigma(lp)+sigm(pp,i)/((n2-1)*(n1-1)**2)
    enddo
110   continue
   stop
   end
```

A.2 Parallel Code Using Message Passing Interface Commands

```
      include 'mpif.h'
      parameter (lrows=50)
      parameter (krows=50)
      parameter (nreal=1)

      complex(KIND=8) h(lrows,lrows*krows,lrows*krows)
      complex(KIND=8) sigm1(lrows,lrows,krows), sigm2(lrows,lrows,krows)
      complex(KIND=8) sigm3(lrows,lrows,krows),cn(lrows*lrows*krows)
      complex(KIND=8) s(lrows,lrows*krows)
      complex(KIND=8) pot(lrows,lrows,krows),sigma(50),sigme(50),sigm(1,nreal)
      complex(KIND=8) Sm,Sd,Sd2
      complex(KIND=8) big_c(2*lrows*krows),current(lrows,lrows,krows)
      complex(KIND=8) big_m(2*lrows*krows,2*lrows*krows) !,Ham(KL2,KL2)
      complex(KIND=8) Ex(lrows-1,lrows-1,krows-1),Ey(lrows-1,lrows-1,krows-1)
      complex(KIND=8) Ez(lrows-1,lrows-1,krows-1),Epl(lrows-1,lrows-1,krows-
     1),Eplm(lrows-1,lrows-1,krows-1)!,Epls(lrows-1,lrows-1,krows-1)
      complex(KIND=8) cons,Epls((lrows-1)*(lrows-1)*(krows-1)),Eplsn((lrows-
     1)*(lrows-1)*(krows-1)*100)
      real(KIND=8) lam1,pr,rn,tita,lamp,lamt,epsb,random!,sigm(2*1,nreal)
      integer n,r,k,l,m,corr,g,n1,n2,KL2,KL,V,myid,ierr,numprocs,t
      integer i,j,kk,nnn,rrr,pp,nc,ik,jk,km,rc,cen,seed,li
      real(KIND=8) Et(krows,nreal),fake
      real(KIND=8) pm(nreal),p,nm(nreal),pmk,fpm(nreal)
      Open(unit=7,file='I_50_test_pc_1_300_3.dat',status='unknown')
!c MPI enviroment
 call MPI_INIT(ierr)
 call MPI_COMM_RANK(MPI_COMM_WORLD, myid, ierr)
 call MPI_COMM_SIZE(MPI_COMM_WORLD, numprocs, ierr)

!c    SUBROUTINE VECTORS
      Sd=(2.2,0.0)
```

```
   Sd2=(2.2,0.0)
   nc=krows
   pp=1
ci=(0.0,1.0)
   n1=lrows
   n2=krows
   KL2=n1*n1*n2
   KL=n1*n2
Sm=(1.570708,0.01478)
   do 110 lp=1,1
p=0.2488126+lp*0.0000000
   do 100 kk=1,nreal
   do k=1,n1
do i=1,n1
do j=1,n2

sigm1(k,i,j)=Sd2
   sigm2(k,i,j)=Sd2
   sigm3(k,i,j)=Sd2
   enddo
enddo
   enddo

   do i=1,n1
   do j=1,KL
   do k=1,KL
   h(i,j,k)=(0.0,0.0)
   enddo
   s(i,j)=(0.0,0.0)
   enddo
   enddo

   do i=1,KL2-n1*n2
```

```
   cn(i)=(0.0,0.0)
   enddo
   do i=KL2-KL+1,KL2
   cn(i)=1.
   enddo

   do i=1,n1
   do j=1,n1
   do k=1,nc

seed=RAND(0)
call SRAND(seed)

if(RAND(0).le.p) then
sigm1(i,j,k)=Sm
else
sigm1(i,j,k)=Sd
endif
if(RAND(0).le.p) then
sigm2(i,j,k)=Sm
else
sigm2(i,j,k)=Sd
endif

if(RAND(0).le.p) then
sigm3(i,j,k)=Sm
else
sigm3(i,j,k)=Sd
   endif

   enddo
   enddo
enddo
```

```
!c      BUILDING VECTORS
        do i=2,n1-1
        do j=2,n1-1
        do k=2,n2-1
        h(i,(j-1)*n2+k,(j-1)*n2+k)=sigm1(i,j,k)+sigm2(i,j,k)+sigm3(i,j,k)+sigm1(i-
1,j,k)+sigm2(i,j-1,k)+sigm3(i,j,k-1)
        h(i,(j-1)*n2+k,(j-1)*n2+k+1)=-sigm3(i,j,k)
        h(i,(j-1)*n2+k,(j-1)*n2+k-1)=-sigm3(i,j,k-1)

        h(i,(j-1)*n2+k,(j-2)*n2+k)=-sigm2(i,j-1,k)
        h(i,(j-1)*n2+k,j*n2+k)=-sigm2(i,j,k)

        s(i,(j-1)*n2+k)=-sigm1(i,j,k)
        enddo

        h(i,(j-1)*n2+1,(j-1)*n2+1)=sigm1(i,j,1)+sigm2(i,j,1)+sigm3(i,j,1)+sigm1(i-
1,j,1)+sigm2(i,j-1,1)+sigm3(i,j,n2)

        h(i,(j-1)*n2+1,(j-1)*n2+2)=-sigm3(i,j,1)
        h(i,(j-1)*n2+1,(j-1)*n2+n2)=-sigm3(i,j,n2)
        h(i,(j-1)*n2+n2,(j-1)*n2+n2)=sigm1(i,j,n2)+sigm2(i,j,n2)+sigm3(i,j,n2)+sigm1(i-
1,j,n2)+sigm2(i,j-1,n2)+sigm3(i,j,n2-1)
        h(i,(j-1)*n2+n2,(j-1)*n2+n2-1)=-sigm3(i,j,n2-1)
        h(i,(j-1)*n2+n2,(j-1)*n2+1)=-sigm3(i,j,n2)

        h(i,(j-1)*n2+1,(j-2)*n2+1)=-sigm2(i,j-1,1)
        h(i,(j-1)*n2+n2,(j-2)*n2+n2)=-sigm2(i,j-1,n2)
        h(i,(j-1)*n2+1,j*n2+1)=-sigm2(i,j,1)
        h(i,(j-1)*n2+n2,j*n2+n2)=-sigm2(i,j,n2)

        s(i,(j-1)*n2+1)=-sigm1(i,j,1)
        s(i,(j-1)*n2+n2)=-sigm1(i,j,n2)
```

```
enddo

h(i,1,1)=sigm1(i,1,1)+sigm2(i,1,1)+sigm3(i,1,1)+sigm1(i-
1,1,1)+sigm2(i,n1,1)+sigm3(i,1,n2)
h(i,1,2)=-sigm3(i,1,1)
h(i,1,n2)=-sigm3(i,1,n2)
h(i,n2,n2-1)=-sigm3(i,1,n2-1)
h(i,n2,1)=-sigm3(i,1,n2)
h(i,n2,n2)=sigm1(i,1,n2)+sigm2(i,1,n2)+sigm3(i,1,n2)+sigm1(i-
1,1,n2)+sigm2(i,n1,n2)+sigm3(i,1,n2-1)
h(i,(n1-1)*n2+1,(n1-
1)*n2+1)=sigm1(i,n1,1)+sigm2(i,n1,1)+sigm3(i,n1,1)+sigm1(i-1,n1,1)+sigm2(i,n1-
1,1)+sigm3(i,n1,n2)
h(i,(n1-1)*n2+1,(n1-1)*n2+2)=-sigm3(i,n1,1)
h(i,(n1-1)*n2+1,(n1-1)*n2+n2)=-sigm3(i,n1,n2)
h(i,(n1-1)*n2+n2,(n1-1)*n2+n2-1)=-sigm3(i,n1,n2-1)
h(i,(n1-1)*n2+n2,(n1-1)*n2+1)=-sigm3(i,n1,n2)
h(i,(n1-1)*n2+n2,(n1-
1)*n2+n2)=sigm1(i,n1,n2)+sigm2(i,n1,n2)+sigm3(i,n1,n2)+sigm1(i-
1,n1,n2)+sigm2(i,n1-1,n2)+sigm3(i,n1,n2-1)

h(i,1,n2+1)=-sigm2(i,1,1)
h(i,n2,2*n2)=-sigm2(i,1,n2)
h(i,(n1-1)*n2+1,(n1-2)*n2+1)=-sigm2(i,n1,1)
h(i,(n1-1)*n2+n2,(n1-2)*n2+n2)=-sigm2(i,n1,n2)

s(i,1)=-sigm1(i,1,1)
s(i,n2)=-sigm1(i,1,n2)
s(i,(n1-1)*n2+1)=-sigm1(i,n1,1)
s(i,(n1-1)*n2+n2)=-sigm1(i,n1,n2)
enddo

do i=2,n1-1
do k=2,n2-1
```

```
h(i,(n1-1)*n2+k,(n1-
1)*n2+k)=sigm1(i,n1,k)+sigm2(i,n1,k)+sigm3(i,n1,k)+sigm1(i-1,n1,k)+sigm2(i,n1-
1,k)+sigm3(i,n1,k-1)
h(i,k,k)=sigm1(i,1,k)+sigm2(i,1,k)+sigm3(i,1,k)+sigm1(i-
1,1,k)+sigm2(i,n1,k)+sigm3(i,1,k-1)
h(i,k,k+1)=-sigm3(i,1,k)
h(i,k,k-1)=-sigm3(i,1,k-1)
h(i,(n1-1)*n2+k,(n1-1)*n2+k+1)=-sigm3(i,n1,k)
h(i,(n1-1)*n2+k,(n1-1)*n2+k-1)=-sigm3(i,n1,k-1)

s(i,k)=-sigm1(i,1,k)
s(i,(n1-1)*n2+k)=-sigm1(i,n1,k)
enddo
enddo

do j=1,n1
do k=1,n2
h(1,(j-1)*n2+k,(j-1)*n2+k)=(1.0,0.0)
h(n1,(j-1)*n2+k,(j-1)*n2+k)=(1.0,0.0)
if (j.ge.2.and.j.le.n1-1) then
h(j,k,n2+k)=-sigm2(j,1,k)
h(j,(n1-1)*n2+k,(n1-2)*n2+k)=-sigm2(j,n1-1,k)
h(j,k,(n1-1)*n2+k)=-sigm2(j,n1,k)
h(j,(n1-1)*n2+k,k)=-sigm2(j,n1,k)
endif
enddo
enddo

do 20 k=2,n1-2
do i=1,2*KL
do j=1,2*KL
big_m(i,j)=(0.0,0.0)
enddo
```

```
      enddo

      do i=1,KL
      do j=1,KL
      big_m(i,j)=h(k,i,j)
      big_m(i+KL,j+KL)=h(k+1,i,j)
      enddo
      big_m(i,i+KL)=s(k,i)
      big_m(i+KL,i)=s(k,i)
      enddo

      do 5 l=1,KL
      do 6 i=l+1,2*KL
      if(big_m(i,l).ne.(0.0,0.0)) then
      cons=big_m(i,l)
      do 7 j=l,2*KL
      big_m(i,j)=big_m(i,j)-cons*big_m(l,j)/big_m(l,l)
 7    continue
      endif
 6    continue
 5    continue

      do i=1,KL
      do j=1,KL
      h(k,i,j)=big_m(i,j)
      if (i.gt.j) then
      h(k,i,j)=big_m(i,j+KL)
      endif
      h(k+1,i,j)=big_m(i+KL,j+KL)
      enddo
      s(k,i)=big_m(i,i+KL)
      enddo
20    continue
```

```
do i=1,2*KL
do j=1,2*KL
big_m(i,j)=(0.0,0.0)
enddo
enddo

do i=1,KL
do j=1,KL
big_m(i,j)=h(n1-1,i,j)
enddo
big_m(i,i+KL)=s(n1-1,i)
enddo
do 15 l=1,KL
do 16 i=l+1,2*KL
if(big_m(i,l).ne.(0.0,0.0)) then
cons=big_m(i,l)
do 17 j=l,2*KL
 big_m(i,j)=big_m(i,j)-cons*big_m(l,j)/big_m(l,l)
 17  continue
endif
16  continue
 15  continue
do i=1,KL
do j=1,KL
h(n1-1,i,j)=big_m(i,j)
if (i.gt.j) then
h(n1-1,i,j)=big_m(i,j+KL)
endif
enddo
s(n1-1,i)=big_m(i,i+KL)
enddo
```

```
!c_____________________________________________________________
!c
!c      BLOCKS ELIMINATION 2
!c      ____________________________________________________________
        do 28 k=n1,2,-1
        do i=1,2*KL
        do j=1,KL
        big_m(i,j)=(0.0,0.0)
        enddo
        enddo
        do i=1,2*KL
        big_c(i)=cn((k-2)*KL+i)
        enddo
        do i=1,KL
        do j=1,KL
                if (i.le.j) then
                        big_m(i+KL,j)=h(k,i,j)
                endif
                if(i.gt.j) then
                        big_m(i,j)=h(k-1,i,j)
                endif
        enddo
        big_m(i,i)=s(k-1,i)
        enddo
    do 8 j=0,KL-1
    do 9 i=j+1,2*KL-1
    big_c(2*KL-i)=big_c(2*KL-i)-big_c(2*KL-j)*big_m(2*KL-i,KL-j)/big_m(2*KL-
j,KL-j)
    big_m(2*KL-i,KL-j)=0.0
 9  continue
 8  continue

    do i=1,KL
```

```
    big_c(KL+i)=big_c(KL+i)/big_m(KL+i,i)
    enddo
        do i=1,2*KL
        cn((k-2)*KL+i)=big_c(i)
        enddo
28      continue
        do i=1,n1
        do j=1,n1
        do k=1,n2
        pot(i,j,k)=cn((i-1)*KL+(j-1)*n2+k)
        enddo
        enddo
        enddo
        do i=1,n1-1
      do j=1,n1-1
        do k=1,n2-1

      Ex(i,j,k)=-(n1-1)*(pot(i+1,j,k)-pot(i,j,k))
      Ey(i,j,k)=-(n1-1)*(pot(i,j+1,k)-pot(i,j,k))
        Ez(i,j,k)=-(n1-1)*(pot(i,j,k+1)-pot(i,j,k))

Epl(i,j,k)=Ex(i,j,k)*CONJG(Ex(i,j,k))+Ey(i,j,k)*CONJG(Ey(i,j,k))+Ez(i,j,k)*CONJG(Ez
(i,j,k))*0.01
      enddo
      enddo
      enddo

      sigm(pp,kk)=0.0
        do k=1,n2-1
        Et(k,kk)=0
        do i=1,n1-1
      do j=1,n1-1
```

```
sigm(pp,kk)=sigm(pp,kk)+sigm1(i,j,k)*(Ex(i,j,k))*CONJG(Ex(i,j,k))+sigm2(i,j,k)*(Ey(i,
j,k))*CONJG(Ey(i,j,k))
     sigm(pp,kk)=sigm(pp,kk)+sigm3(i,j,k)*(Ez(i,j,k))*CONJG(Ez(i,j,k))
        enddo
        enddo
        enddo
      li=0
      do i=1,n1-1
      do j=1,n1-1
      do k=1,n2-1
!      write(7,*) Epl(i,j,k),i,j,k,kk,myid
       li=li+1
       Epls(li)=Epl(i,j,k)
       enddo
      enddo
      enddo
      call
MPI_Gather(Epls,li,MPI_DOUBLE_COMPLEX,Eplsn,li,MPI_DOUBLE_COMPLEX,0,
MPI_COMM_WORLD,ierr)
      if (myid.eq.0) then
      do i=1,li*numprocs
      write(7,*),Eplsn(i)
      enddo
      endif
      pmk=0.0
      sigma(lp)=(0.0,0.0)
      do i=1,nreal
      sigma(lp)=sigma(lp)+sigm(pp,i)/((n2-1)*(n1-1)**2)
      pmk=pm(i)+pmk
      enddo
      print*,krows,lrows,p,kk,sigma(lp)/nreal,myid
 call MPI_Reduce(sigma(lp)/nreal,sigme(lp), 1, MPI_DOUBLE_PRECISION,
MPI_SUM, 0, MPI_COMM_WORLD, ierr)
```

```
      if (myid==0) then
      write(7,*),krows,lrows,p,kk,'sigmeff',sigme(lp)/numprocs
      end if
110     continue
      call MPI_FINALIZE(rc)
     stop
     end
```

BIBILIOGRAPHY

1. R. W. Wood , *On a remarkable case of uneven distribution of light in a diffraction grating spectrum*, Phil. Mag. 4, 396 (1902).

2. J. C. Maxwell Garnett, *Colours in Metal Glasses and in Metallic Films*, Philos. Trans. R. Soc., London 203, 385 (1904).

3. G. Mie, *Beiträge zur Optik trüber Medien*, speziell kolloidaler Metallösungen, *Ann. Phys. (Leipzig)* 25, 377 (1908).

4. "https://blog.britishmuseum.org/2014/04/30/the-lycurgus-cup-transformation-in-glass/"

5. D. Pines, *Collective Energy Losses in Solids*, Rev. Mod. Phys. 28, 184-198 (1956).

6. R. H. Ritchie, *Plasma Losses by Fast Electrons in Thin Films*, Phys. Rev. 106, 874 (1957).

7. J. J. Hopfield, *Theory of the Contribution of Excitons to the Complex Dielectric Constant of Crystals*, Phys. Rev. 112, 1555 (1958).

8. R. H. Ritchie, E. T. Arakawa, J. J. Cowan, and R. N. Hamm, *Surface-plasmon resonance effect in grating diffraction*, Phys. Rev. Lett. 21, 1530–1532 (1968).

9. A. Otto, *Excitation of nonradiative surface plasma waves in silver by the method of frustrated total reflection*, Z. Phys. 216, 398 (1968)

10. E. Kretschmann, and H. Raether, *Radiative decay of non-radiative surface plasmons excited by light*, Z Naturf. 23A, 2135 (1968).

11. Laboratory of Electro-Optical Stimulation, *Surface plasmon excitation*, Kung University,"www.leos.phys.ncku.edu".

12. U. Kreibig, and P. Zacharias, *Surface plasma resonances in small spherical silver and gold particles*, Z. Physik 231, 128 (1970).

13. S. L. Cunningham, A. A. Maradudin, and R. F. Wallis, *Effect of a charge layer on the surface-plasmon-polariton dispersion curve*, Phys. Rev. B 10, 3342 (1974).

14. M. Fleischmann, P. J. Hendra, and A. J. McQuillan, *Raman spectra of pyridine adsorbed at a silver electrode*, Chem. Phys. Lett. 26, 163 (1974).

15. V. G. Veselago, *The ElectroDynamics of substances with simultaniously negative values of ϵ and μ*, Soviet Physics Uspekhi, vol. 10, no. 4, pp. 509-514 (1968).

16. V. M. Shalaev, *Optical negative-index metamaterials*, *Nat Photon*, vol. 1, no. 1, pp. 41-48 (2007).

17. H. Liu, Y. M. Liu, T. Li, S. M. Wang, S. N. Zhu, and X. Zhang, *Coupled magnetic plasmons in metamaterials*, *0907.4208* (2009).

18. J. B. Pendry, *Negative Refraction Makes a Perfect Lens*, Physical Review Letters, vol. 85, no. 18, pp. 3966 (2000).

19. D. Smith, W. Padilla, D. Vier, S. Nemat-Nasser, and S. Schultz, *Composite Medium with Simultaneously Negative Permeability and Permittivity,* Physical Review Letters, vol. 84, no. 18, pp. 4184-4187 (2000).

20. R. A. Shelby, D. R. Smith, and S. Schultz, *Experimental Verification of a Negative Index of Refraction*, Science, vol. 292, no. 5514, pp. 77 -79 (2001).

21. R. A. Shelby, D. R. Smith, S. C. Nemat-Nasser, and S. Schultz, *Microwave transmission through a two-dimensional, isotropic, left-handed metamaterial*, Applied Physics Letters, vol. 78, no. 4, pp. 489 (2001).

22. C. G. Parazzoli, R. B. Greegor, K. Li, B. E. C. Koltenbah, and M. Tanielian, *Experimental verification and simulation of negative index of refraction using Snell's law*, Physical Review Letters, vol. 90, no. 10, pp. 107401 (2003).

23. S. A. Ramakrishna, *Physics of negative refractive index materials*, Reports on Progress in Physics, vol. 68, no. 2, pp. 449-521 (2005).

24. T. J. Yen, W. J. Padilla, N. Fang, D. C. Vier, D. R. Smith, J. B. Pendry, D. N. Basov, and X. Zhang, *Terahertz Magnetic Response from Artificial Materials*, *Science*, vol. 303, no. 5663, pp. 1494 -1496 (2004).

25. S. Linden, C. Enkrich, M. Wegener, J. Zhou, T. Koschny, and C. M. Soukoulis, *Magnetic Response of Metamaterials at 100 Terahertz*, *Science*, vol. 306, no. 5700, pp. 1351 -1353 (2004).

26. V. Podolskiy, A. Sarychev, and V. Shalaev, *Plasmon modes and negative refraction in metal nanowire composites*, *Optics Express*, vol. 11, no. 7, pp. 735-745 (2003).

27. V.M. Shalaeve, W. Cai, U.K.Chettiar, H-K. Yuan, A.K. Sarychev, V.P. Drachev, and A.V.Kildishev, *Negative index of refraction in optical metamaterials*, Optics Letters, vol. 30, no. 24, pp. 3356-3358 (2005).

28. J. Valentine, S. Zhang, T. Zentgraf, E. Ulin-Avila, D. A. Genov, G. Bartal, and X. Zhang, *Three-dimensional optical metamaterial with a negative refractive index*, *Nature*, vol. 455, no. 7211, pp. 376-379 (2008).

29. X. Zhang, *Applied physics: Extreme light-bending power*, *Nature*, vol. 470, no. 7334, pp. 343-344 (2011).

30. W. J. Padilla, *Semiconductors: A new class of metamaterials*, *Nat Mater*, vol. 6, no. 12, pp. 922-923 (2007).

31. A. J. Hoffman, L. Alekseyev, S. S. Howard, K. J. Franz, D. Wasserman, V. A. Podolskiy, E. E. Narimanov, D. L. Sivco, and C. Gmachl, *Negative refraction in semiconductor metamaterials*, *Nat Mater*, vol. 6, no. 12, pp. 946-950 (2007).

32. J.Yao, Z. Liu, Y. Wang, C. Sun, G. Bartal, A. M. Stacy, and X. Zhang, *Optical Negative Refraction in Bulk Metamaterials of Nanowires*, *Science*, vol. 321, no. 5891, pp. 930 (2008).

33. Kneipp K, Wang Y, Kneipp H, Perelman L T, Itzkan I, Dasari R and Feld M S, *Singe molecule detection using surface-enhanced raman scattering (SERS)*, Phys. Rev. Lett., vol. 78, pp. 1667 (1997).

34. J. Zhang, L. Zhang L, and W. Xu, *Surface plasmon polaritons: physics and applications*, J. Phys. D: Appl. Phys. 45 113001 (2012).

35. D. A. G. Bruggeman, *Berechnung verschiedener physikalischer Konstanten von heterogenen Substanzen*, Ann. Phys. (Leipzig) vol. 24, pp. 636-679 (1935).

36. A. P. Vinogradov, A. M. Karimov, and A. K. Sarychev, *Permittivity of composite Percolation Materials: Similarity Law and equation of State*, Sov. Phys. JETP, vol. 67, pp. 212 (1988).

37. G. Depardieu, P. Fiorini, and S. Berthier, *Optical properties of cermets: 3D real space renormalization using the connection machine*, Physica A: Statistical Mechanics and its Applications, vol. 207, pp. 110 (1994).

38. D. J. Frank and C. J. Lobb, *Highly efficient algorithm for percolative transport studies in two dimensions*, Physics Review B, vol. 37, pp. 302 (1988).

39. B. Derrida, D. Stauffer H. J. Herrmann, and J. Vannimenus, *Transfer matrix calculation of the conductivity in three dimensional random resistor networks at percolation threshold*, Journal de Physique Lettres, vol. 44, pp. 701-L706 (1983).

40. L. Zekri, R. Bouamrane, and N. Zekri, *New method for the exact determination of the effective conductivity and the local field in RLC networks*, Journal of Physics A: Mathematical and General, vol. 33, pp. 649-656 (2000).

41. D. A. Genov, A. K. Sarychev, and V. M. Shalaev, *Plasmon localization and local field distribution in metal-dielectric films*, Physical Review E - Condensed Matter and Materials Physics, vol. 67, pp. 56611 (2003).

42. S. R. Animilli, and D. A. Genov, *Geometrical phase transition and local field moments in metal-dielectric composite media*, PRB (2016) (Under Review).

43. S. R. Animilli, Ashish Sharma, D. A. Genov, and S. Zivanovic, *Semi continuous metal dielectric composites in thin-film silicon solar cell*, JAP (2016) (To be Submitted).

44. Ashish Sharma, S. Zivanovic, S.R. Animilli, and D. A. Genov, *Analytical Model of Thin-Film Silicon Solar Cell,* ASME-IMECE2015-50793, pp. V06BT07A042 (2015).

45. V. M. Shalaev, *Nonlinear Optics of Random Media: Fractal Composites and Metal-Dielectric Films* (Springer-Verlag, Berlin, 2000).

46. A. K. Sarychev and V. M. Shalaev, *Electrodynamics of Composite Materials* (World Scientific, Singapore 2003).

47. A. Bunde and S. Havlin, Fractals and Disordered Systems (Springer-Verlag, Heidelberg, 1991).

48. N. Kaiser, *Review of fundamentals of thin-film growth*, Appl. Opt. 41, 3053 (2002).

49. A. A. D. Stauer, *Introduction to Percolation Theory*, 2 ed. Philadelphia: Taylor and Francis , 1991.

50. J. P. Clerc, G. Giraud, J. M. Laugier, and J. M. Luck, *The electrical conductivity of binary disordered systems, percolation clusters, fractals and related models*, Advances in Physics, vol. 39, pp. 191-309 (1990).

51. D. J. Bergman, and D. Stroud, *Physical Properties of Macroscopically Inhomogeneous Media*, Solid-State Physics, vol. 46, pp. 147-269, 1992.

52. A. K. Sarychev, and V. M. Shalaev, *Electromagnetic field fluctuations and optical nonlinearities in metal-dielectric composites*, Physics Report, vol. 335, pp. 275-371, 2000.

53. F. Hache, D. Ricard, C. Flytzanis, and U. Kreibig, *The optical Kerr effect in small metal particles and metal colloids: The case of gold*, Applied Physics A Solids and Surfaces, vol. 47, pp. 347-357, 1988.

54. Y. Yagil, P. Gadenne, C. Julien, and G. Deutscher, *Optical properties of thin semi-continuous gold films over a wavelength range of 2.5 to 500 μm*, Physical Review B, vol. 46, pp. 2503-2511, 1992.

55. D. A. Genov, V. M. Shalaev, and A. K. Sarychev, *Surface plasmon excitation and correlation-induced localization- delocalization transition in semicontinuous metal films*, Physical Review B - Condensed Matter and Materials Physics, vol. 72, pp. 1-4, 2005.

56. F. Brouers, J. M. Jolet, G. Giraud, J. M. Laugier, and Z. A. Randriamanantany, *Cluster plasmon resonances close to the percolation threshold: simulation versus EMA*, Physica A: Statistical Mechanics and its Applications, vol. 207, pp. 100-105 (1994).

57. A. M. Dykhne, *Anomalous plasma resistance in a strong magnetic field*, *Sov. Phys. JETP* vol. 32, p. 348 (1971).

58. T.W. Noh, P.H. Song, Sung-Il Lee, D.C. Harris, J.R. Gaines, and J.C. Garland, *Far-infrared studies of two-dimensional random metal-insulators composites*, Physical Review B: Condensed matter, vol. 46, pp. 4212 (1992).

59. A. P. Vinogradov, A. M. Karimov, and A. K. Sarychev, *Permittivity of composite percolation materials: similarity law and equations of state*, Sov. Phys. JETP 67, 212 (1988).

60. G. Depardieu, P.Fiorini, S. Berthier, *Optical properties of cermets: 3D real space renormalization using the connection machine*, Physica A: Statistical Mechanics and its Applications, vol. 207, pp. 110 (1994).

61. A.K. Sarychev, *Scale invariance and percolation in a random field*, *Sov. Phys. JETP*, vol.45, pp. 524 (1977).

62. F. Brouers, S. Blacher, and A.K. Sarychev, *Fractals in the Natural and Applied Sciences*, (Chapman and Hall, London,1995), Chap. 24.

63. F. Brouers, S. Blacher, A.N. Lagarkov, A.K. Sarychev, P. Gadenne, V.M. Shalaev, *Theory of giant Raman scattering from semicontinuous metal films*, Physical Review B, vol.55 pp. 13234 (1997).

64. B. Derrida, and J. Vannimenus, *A transfer matrix approach to random resistor networks*, J. Phys. A 15, L557 (1982).

65. D. A. Genov, A. K. Sarychev, and V. M. Shalaev, *Metal-dielectric composite filters with controlled spectral windows of transparency*, J. Nonlinear Opt. Phys. Mater.12, 419 (2003).

66. A. K. Sarychev, D. J. Bergman, and Y. Yagil, *Theory of the optical and microwave properties of metal-dielectric films*, Phys. Rev. B 51, 5366 (1995).

67. K. Seal, D. A. Genov, M. A. Nelson, Z. C. Ying, A. K. Sarychev, and V. M. Shalaev, *Growth, morphology, and optical and electrical properties of semicontinuous metallic films*, Phys. Rev. B 67, 35318 (2003).

68. S. I. Bozhevolnyi, V. A. Markel, V. Coello, W. Kim, and V. M. Shalaev, *Direct observation of localized dipolar excitations on rough nanostructured surfaces*, Phys. Rev. B 58, vol. 17, 11441 (1998).

69. S. Gresillon, L. Aigouy, A. C. Boccara, J. C. Rivoal, X. Quelin, C. Desmarest, P. Gadenne, V.A. Shubin, A. K. Sarychev, and V. M. Shalaev, *Experimental Observation of Localized Optical Excitations in Random Metal-Dielectric Films*, Phys. Rev. Lett. 82, 4520 (1999).

70. A. L. Efros and B. I. Shklovskii, *Critical Behaviour of Conductivity and Dielectric Constant near the Metal-Non-Metal Transition Threshold*, Phys. Status Solidi 76, 475 (1976).

71. M. Sahimi, B. D. Hughes, Le. E. Scriven, and H. T. Davis, *Critical exponent of percolation conductivity by finite size scaling*, J. Phys. C 16, L521-L527 (1983).

72. *D.Stauffer* and A. *Aharony*, *Introduction to Percolation Theory*, 2nd ed, (Taylor and Francis, London, 1992).

73. C. D. Lorenz and R. M. Ziff, *Precise determination of the bond percolation thresholds and finite-size scaling corrections for the sc, fcc, and bcc lattices*, Physical Review E, vol. 57, pp. 230-236 (1998).

74. R. M. Ziff and G. Stell, University of Michigan Report No. 88-4 (1988) (unpublished).

75. J. P. Straley, *Critical Phenomena in resistor networks*, *J. Phys. C* 9, 783-795 (1976).

76. F. Brouers, S. Blacher, and A. K. Sarychev, *Giant field fluctuations and anomalous light scattering from semicontinuous metal films*, Physical Review B - Condensed Matter and Materials Physics, vol. 58, pp. 15897-15903 (1998).

77. B. Derrida, D. Stauffer, H. J. Herrmann, and J. Vannimenus, *Transfer matrix calculation of the conductivity in three dimensional random resistor networks at percolation threshold*, Journal de Physique Lettres, vol. 44, pp. 701-L706 (1983).

78. J.M. Normand and H.J. Herrmann, *Precise determination of the conductivity exponents of 3D percolation using Percola*, Intl. J. Mod. Phys. C, vol. 6, pp. 813-817 (1995).

79. D.B. Gingold, C.J. Lobb, *Percolative Conduction in Three Dimensions*, Phys. Rev. B. vol. 42, pp 8220-8224 (1990).

80. J. P. Clerc, V. A. Podolskiy, A. K. Sarychev, *Precise determination of the conductivity exponent of 3D percolation using exact numerical renormalization*, European Physical Journal B: Condensed Matter and Complex Systems, vol. 15, pp. 507-516 (2000).

81. V. M. Shalaev, *Electromagnetic properties of small-particle composites*, Phys. Rep. 272, 61-137 (1996).

82. A. V. Butenko, V. M. Shalaev, and M. I. Stockman, *Giant impurity nonlinearities in optics of fractal* clusters, Sov. Phys. JETP 67, 60 (1988).

83. V. A. Markel, L. S. Muratov, M. I. Stockman, and T. F. George, *Theory and numerical simulation of optical properties of fractal clusters*, Phys. Rev. B43, 8183 (1991).

84. D. P. Tsai, J. Kovacs, Z. Wang, M. Moskovits, V. M. Shalaev, J. Suh, and R. Botet, *Photon scanning tunneling microscopy images of optical excitations of fractal metal colloid clusters*, Phys. Rev. Lett. 72, 4149 (1994).

85. V. M. Shalaev, and M. Moskovits, *Shalaev and Moskovits Reply,* Phys. Rev. Lett. 75, 2451 (1995).

86. P. Zhang, T. L. Haslett, C. Douketis, and M. Moskovits, *Mode localization in self-affine fractal interfaces observed by near-field microscopy*, Phys. Rev. B 57, 15513 (1998).

87. M. I. Stockman, L. N. Pandey, L. S. Muratov, and T. F. George, *Giant fluctuations of local optics fields in fractal clusters*, Phys. Rev. Lett. 72, 2486 (1994).

88. M. I. Stockman, L. N. Pandey, L. S. Muratov and T. F. George, *Optical absorption and localization of eigenmodes in disorder clusters*, Phys. Rev. B 51, 185 (1995).

89. M. I. Stockman, L. N. Pandey and T. F. George, *Inhomogeneous localization of olar eigenmodes in fractals*, Phys. Rev. B 53, 2183 (1996).

90. M.I. Stockman, *Inhomogeneous eigenmode localization, chaos and correlations in large disordered clusters*, Phys. Rev. E 56, 6494 (1997).

91. V. P. Safonov, V. M. Shalaev, V. A. Markel, Yu. E. Danilova, N. N. Lepeshkin, W. Kim, S. G. Rautian, and R. L. Armstrong, *Spectral Dependence of Selective Photomodification in Fractal Aggregates of Colloidal Particles*, Phys. Rev. Lett. 80, 1102 (1998).

92. M. Moskovits, *Surface-enhanced spectroscopy*, Rev. Mod. Phys. 57 , 783 (1985).

93. R. K. Chang and T. E. Furtak , *Surface Enhance Raman Scattering*, eds (Plenum Press, New York, 1982).

94. A. Otto, I. Mrozek, H. Grabhorn and W. Akemann, *Surface-enhanced Raman Scattering,* J. Phys.: Condensed Matter 4, 1143 (1992).

95. V. M. Shalaev, E. Y. Poliakov, and V. A. Markel, *Small-particle composites. II. Nonlinear optical properties*, Phys. Rev. B, 53, 2437 (1996).

96. D. Ricard, Ph. Roussignol and C. Flytzanis, *Surface-mediated enhancement of optical phase conjugation in metal colloids*, Opt. Lett. 10, 511 (1985).

97. F. Hache, D. Ricard, C. Flytzanis and U. Kreibig, *The optical kerr effect in small metal particles and metal colloids: The case of gold*, Applied Physics A 47, 347 (1988).

98. L. D. Landau, E. M. Lifshitz, and L.P. Pitaeveskii, *Electromagnetics of Continuous Media*, 2nd ed. (Pergamon, Oxford, UK, 1984).

99. R. W. Boyd, *Nonlinear Optics*, (Academic Press, New York, 1992).

100. M. I. Stockman, S. V. Faleev, and D. J. Bergman, *Localization versus Delocalization of Surface Plasmons in Nanosystems: Can One State Have Both Characteristics?*, Phys. Rev. Lett. 87, 167401 (2001).

101. D. A. Genov, V. M. Shalaev, and A. K. Sarychev, *Surface plasmon excitation and correlation-induced localization- delocalization transition in semicontinuous metal films*, Physical Review B - Condensed Matter and Materials Physics, vol. 72, pp. 113102 (2005).

102. D. A. Genov, A.K. Sarychev, V.M. Shalaev, and A. Wei, *Resonant Field Enhancement from Metal Nanoparticle Arrays*, Nano Letters, 4, 153-158 (2004).

103. J. Kim, Z. Hong, G. Li, T. Song, J. Chey, Y. S. Lee, J. You, C. C. Chen, D. K. Sadana, and Y. Yang, *10.5% efficient polymer and amorphous silicon hybrid tandem photovoltaic cell*, Nat Commun, 6 (2015).

104. R. A. Sinton, Y. Kwark, J. Y. Gan, and R. M. Swanson, *27.5-Percent Silicon Concentrator Solar Cells*, IEEE Electron Device Letters, EDL-7, pp. 567-569 (1986).

105. B. C. Rowan, L. R. Wilson, and B. S. Richards, *Advanced Material Concepts for Luminescent Solar Concentrators*, IEEE Journal of Selected Topics in Quantum Electronics, vol. 14, pp. 1312-1322 (2008).

106. M. Florescu, H. Lee, I. Puscasu, M. Pralle, L. Florescu, D. Z. Ting and J. P. Dowling, *Improving solar cell efficiency using photonic band-gap materials*, Solar energy materials and solar cells, vol. 91, pp. 1599-1610 (2007).

107. S. Pillai, K. R. Catchpole, T. Trupke, and M. A. Green, *Surface plasmon enhanced silicon solar cells*, Journal of Applied Physics, 101(9), p. 093105 (2007).

108. A. Shah, *Thin-Film Silicon Solar Cell: Micro- and Nanotechnology*, EPFL Press, Switzerland (2010).

109. M. A. Green, K. Emery, Y. Hishikawa, W. Warta, and E. D. Dunlop, *Solar cell efficiency tables* (Version 45), Prog. Photovolt: Res. Appl., 23(1), pp. 1–9 (2015).

110. Ashish Sharma, Sandra Zivanovic, Shravan R. Animilli and Dentcho A. Genov, *Analytical Model of Thin-Film Silicon Solar Cell*, IMECE2015-50793, pp. V06BT07A042 (2015).

111. K. Seal, M. Nelson, Z. Ying, D. Genov, A. Sarychev, and V. Shalaev, *Metal coverage dependence of local optical properties of semicontinuous metallic films*, Journal of Modern Optics, vol. 49, no. 14/15, pp.2423-2435 (2002).

112. K. Seal, M. A. Nelson, Z. C.Ying, D. A. Genov, A. K. Sarychev, and V. M. Shalaev, *Growth, morphology, and optical and electrical properties of semicontinuous metallic films*, Physical Review B, vol. 67, pp. 035318-1-13 (2003).

113. D. A. Genov, K. Seal, Mark. A. Nelson, A. K. Sarychev, Z. C. Ying, and V. M. Shalaev, *Local Filed Distribution in Random Metal-Dielectric films; Theory and Experiment*, Physica B: Physics of Condensed Matter, vol. 338, Issue 1-4, pp. 228 (2003).

114. Yu. A. Akimov, W. S. Koh, K. Ostrikov, *Enhancement of optical absorption in thin-film solar cells through the excitation of higher-order nano-particle plasmon modes*, Optical Society of America, vol. 17, pp. 10195-10205 (2009).

115. S.Pillai, K.R. Catchpole, T. Trupke, and M.A. Green, *Surface plasmon enhanced silicon solar cells*, Journal of Applied Physics, vol. 101, pp. 093105 (2007).

116. R. A. Pala, J. White, E. Barnard, J. Liu, and M. L. Brongersma, *Design of Plasmonic Thin-Film Solar Cells with Broadband Absorption Enhancements*, *Advanced Materials*, vol. 21, no. 34, pp. 3504-3509 (2009).

117. A. Tamang, A. Hongsingthong, P. Sichanugrist, V. Jovanov, M. Konagai, and D. Knipp, *Light-Trapping and Interface Morphologies of Amorphous Silicon Solar Cells on Multiscale Surface Textured Substrates*, IEEE Journal of Photovoltaics, pp.16-21, vol.4 (2014).

118. Y. P. Singh, A. Jain, and A. Kapoor, *Localized Surface Plasmons Enhanced Light Transmission into c-Silicon Solar Cells*, Journal of Solar Energy (2013).

119. Z. Yu, A. Raman, and S. Fan, *Fundamental limit of nanophotonic light trapping in solar cells*, Proc. Natl. Acad. Sci. U S A, 107(41), pp. 17491–17496 (2010).

120. Z. Yu, S. Sandhu, and S. Fan, *Efficiency above the shockley-queisser limit by using nanophotonic effects to create multiple effective bandgaps with a single semiconductor*, Nano Letters, 14(1), pp. 66–70 (2014).

121. F. Priolo, T. Gregorkiewicz, M. Galli, and T. F. Krauss, *Silicon nanostructures for photonics and photovoltaics*, Nat Nano, 9(1), pp. 19–32 (2014).

122. R. Santbergen and R.J.C. van Zolingen, *The absorption factor of crystalline silicon PV cells: A numerical and experimental study*, Solar Energy Materials and Solar Cells, vol. 92, no. 4, pp. 432-444 (2008).

123. J. O. Schumacher and W. Wettling, *Device Physics of Silicon Solar Cells*, vol. 3. (London: Imperial College Press, 2000).